Experimental studies on Soot and Particulate reduction in Heavy Fuel Oil Combustion

A THESIS
SUBMITTED FOR THE DEGREE OF
DOCTOR OF PHILOSOPHY
By

Saurabh Markandeya

Department of Mechanical Engineering
Indian Institute of Science
Bangalore, India
July, 2018

DEDICATED TO

my wife Kajal

Acknowledgements

I would like to express my deepest gratitude and respect to my research advisor Prof. R. V. Ravikrishna. I greatly appreciate his simple and yet magnificent persona which I have experienced during my research. His openness to new ideas, his in-depth knowledge and expertise in the field helped me to successfully overcome challenges during my research. This entire work has been a great pleasure because of his supportive and amicable nature.

I express my sincere thanks to Prof. J. H. Arakeri, Dr. R. N. Goverdhan and Prof. M. S. Bobji who helped me during my research work with timely advice and allowed to use instruments from their labs. I thank my departmental chairmen, office staff, and workshop staff for their support.

I express my sincere thanks to ICER chairmen, office staff and department staff for their support. I also express my sincere thanks to AFMM facility staff and Center for Nanoscience and Engineering staff for allowing me to use their departmental facilities.

I gratefully acknowledge Devendra and Madan for imparting meticulous training on the laser diagnostic equipments.

I deeply cherish the discussions with Prasad and Suryaprakash which helped me in developing my experimental setups.

I thank my other labmates Amrit, Krishna, Shantanu, Atanu, Pabitro, Nishant and Pallav who made my time spent in lab pleasant.

I would like to thank my parents and in-laws for all their love and support that kept me going. Finally, a special ‘Thank you’ to my wife, Kajal whose patient love and constant support enabled me to complete this work.

Abstract

Heavy fuel oil (HFO) is extensively used in industrial burners and marine engines. HFO droplet combustion gives rise to carbon particulates generated by pyrolysis, which are called cenospheres. There is a current hypothesis that ‘one HFO droplet generates one cenosphere’, though there is no strong experimental evidence in support of this hypothesis. The present research deals with experimental study of HFO droplet combustion and investigates effect of HFO spray characteristics on carbon particulate emission in a spray combustion environment. A new research burner is designed to study combustion characteristics of a sparse HFO spray in a controlled high temperature environment (800 K – 1300 K). A nebulizer system generates a sparse spray of HFO droplets which enables fundamental studies on droplet combustion. Initially, spray evaporation studies are performed with standard liquids such as n-decane and n-dodecane. The droplet evaporation rate constant K_{evap} data derived from experiments are found to be in good agreement with those from literature. The research burner is then utilized to study HFO spray combustion and particulate formation. A novel Laser-induced fluorescence (LIF) based optical technique is developed to optically image HFO droplets in the high temperature spray flame environment. Based on this data, fuel injection parameters are optimized to achieve spray characteristics with Sauter Mean Diameters (SMD) ranging from 24-µm to 53-µm.

Soot measurements are carried out in the HFO spray flames using the Laser Induced Incandescence (LII) technique to identify soot formation and oxidation zones. Soot is observed to be produced at lower flame heights and subsequently oxidized along the spray flame height. It is observed that a reduction in SMD from 53-µm to 24-µm leads to a 58% reduction in soot formation. To investigate the impact of HFO spray characteristics and environment temperature on droplet pyrolysis, the cenosphere sizes are measured using an aerodynamic particle sizer. With change in SMD from 53-µm to 24-µm, a drastic reduction (~90%) in cenosphere emission density (particles/cm^3) is observed. It is also observed that higher temperatures ranging from 1073 K to 1223 K are favorable for cenosphere reduction. The morphological study of cenospheres indicates that these are nascent coke particles generated at the end of the droplet combustion phase. The results seem to indicate that the 'one droplet generates one cenosphere' theory is not applicable for smaller droplets. The data is further analyzed to establish the existence of a critical diameter of HFO, which undergoes complete combustion in the droplet combustion phase without generating a solid coke particle. In other words, if a HFO spray consists of droplets whose diameter is below this critical value, the particulate emissions can be nearly zero. From the experimental data, the critical droplet diameter is found to be in range of 18-µm to 23-µm for the medium grade of HFO used.

Keywords: Heavy fuel oil (HFO), Spray, Droplets, Combustion, Particulate emission, Soot, Cenospheres, Laser Induced Incandescence, Laser Induced Fluorescence

Table of contents

List of figures

List of tables

1 Introduction

Since the industrial revolution, crude oil has become a conventional source of energy. However, at present, the depleting reserves of crude oil and the pollution caused due to its burning has become a subject of global concern. The lighter components of crude oil such as gasoline and diesel are widely used in automotive applications. The heavier components such as bunker oil and heavy fuel oil (HFO) are widely used for marine and stationary power generation. Being a by-product of crude oil distillation, these heavy fuels are cheap and hence widely used as a fuel. Recently, with the increased demand for automotive fuels and stricter pollution norms, the automotive fuels are becoming lighter and hence the content of residual fuels is becoming heavier with more residual carbon. This has reduced the quality of bunker and heavy fuel oils. With increased awareness of ill effects of pollution from marine engines and stationary power plants, it has become imperative to study the burning characteristics of these residual fuels and reduce emissions during their combustion.

In India, HFO is used for power generation, marine applications and small and medium process heat boilers. During the year 2009-2010, in India, HFO consumption stood at 0.7 million tons for power generation and 3.2 million tons for industrial applications. Almost 90% of the small (20 – 100 kW) and medium (100 – 1000 kW) process heat boilers employ HFO as fuel due to its low cost. A typical elemental composition of HFO is shown in Table 1.1.

Elements	%
Carbon	~ 83 -87
Hydrogen	~ 10 – 12
Nitrogen	~ 0.3 – 0.6
Sulphur	~ 2 – 3
Metal residues (V, Ni, Na)	~ 50 – 500 ppm
Ash	~ 0.02 – 0.1%

Table 1.1 Typical composition of a Heavy Fuel Oil (HFO).

Surrogate composition	%
Light diesel	~ 75 - 85
Vacuum residual	~ 15 – 25

Table 1.2 Surrogate equivalent of HFO.

Physical properties	Typical HFO	Used Medium grade HFO
Viscosity at 50 °C (cSt)	390 - 450	76
Viscosity at 100 °C (cSt)	14 - 25	14
Specific gravity	0.98	0.9566
Calorific value (MJ/kg)	~ 35 - 40	36
Surface tension at 20 °C (N/m)	0.0275 – 0.030	-

Table 1.3 Typical physical properties of a Heavy Fuel Oil (HFO).

There is no fixed chemical composition of HFO and it largely depends upon the source of the crude oil and the distillation process. Chemically, HFO mainly consists of large aliphatic chains, aromatic compounds, asphaltene and free carbon with traces of metals. Hence most of the research community uses a surrogate equivalent of HFO, which is a mixture of light diesel oil and vacuum residual of crude oil (Refer Table 1.2). Due to the presence of heavy hydrocarbons, HFO is a thick liquid and exhibits high viscosity and density. The physical properties of a typical HFO are listed in Table 1.3.

A distillation curve of a typical HFO is shown in Figure 1.1 and a distillation curve for a medium grade HFO used in present research is shown in Figure 1.2. It clearly shows that it is very difficult to achieve complete evaporation of HFO droplets in a spray prior to combustion. This makes it very difficult to achieve complete combustion and reduce emissions of unburnt HC, CO, and particulates. It is a widely accepted fact that the presence of heavy components in the HFO results in carbon particulate emissions. Many researchers have proposed different ways to quantify the heaviness of HFO. Some of the principles/procedures used to define heaviness in regards to the ability to form carbon particulates and their typical range for an HFO are listed in Table 1.4. Among the various issues with HFO combustion, carbon particulate emissions are of a major concern. A wide range of carbon particulates (sizes ranging from 10 nm up to 100 µm) are generated during HFO combustion. These particulates are classified based on size range as ‘soot’ for size ranging from 10-nm to 1-µm, and ‘cenospheres’ for size ranging from 1-µm to 100-µm.

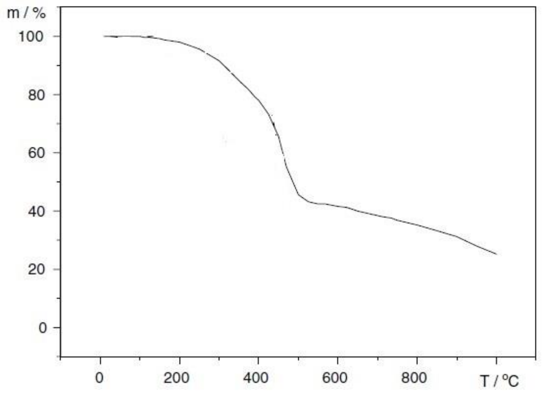

Figure 1.1 Typical distillation curve of a HFO [1].

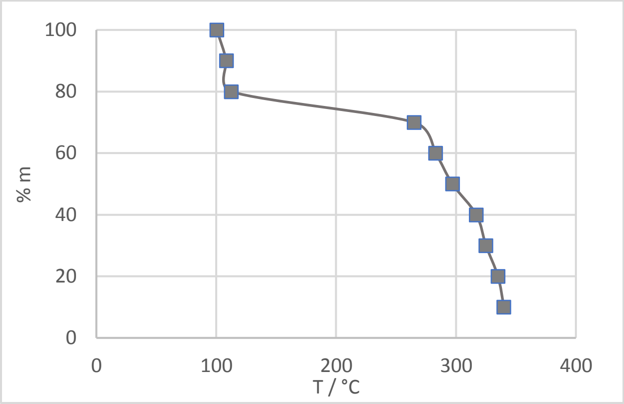

Figure 1.2 Distillation curve of medium grade HFO used in our research.

Heavy component characterization	
Ramsbottom	~ 3 - 18 %
Conradson Number	~ 6 - 22
n-Heptane insoluble (Asphaltenes)	~ 5 - 20 %
n-Pentane insoluble	~ 11 %
Coke formation index	0.4 - 0.1

Table 1.4 Typical heavy component characterization indexes of HFO.

The mechanisms of formation for these two classes of carbon particulates are quite different. Soot is a result of condensation of polyaromatic hydrocarbons (PAH) on to carbon-rich nuclei formed during gas-phase combustion, while cenospheres are generated due to pyrolysis of HFO droplets during combustion. There is a widely accepted hypothesis that ‘One HFO droplet generates one cenosphere', though there is no strong experimental evidence for the same.

The present research deals with an experimental study of fine HFO droplet combustion and investigates the effect of HFO spray characteristics on carbon particulate emission in a spray combustion environment. The present research work is organized in the following major sections:

1. Introduction
2. Literature survey
3. Experimental techniques
4. Experimental setups
5. HFO spray characterization
6. Soot formation in HFO spray flames
7. Cenosphere formation in HFO spray flames and
8. Conclusions

Chapter 2 introduces the HFO combustion phenomenon related to the particulate formation and describes the present state of understanding of scientific literature in this regard. The chapter is concluded by the definition of the ‘problem statement’ of the present research.

Chapter 3 describes various experimental techniques used during this research to investigate flow fields, spray characteristics, HFO spray combustion and particulate formation. A detailed review of ‘Laser Induced Incandescence (LII)’ technique is presented which is used for in-situ soot measurements in flames. Techniques such as PDIA for spray characterization, PIV to investigate flow fields in spray flames and aerodynamic particle size spectroscopy to measure particulate emissions are also briefly discussed.

Chapter 4 describes an experimental research burner used to study HFO spray combustion and technical requirements of different sub-systems of the setup. A fundamental study of single component liquid droplet evaporation in convective environment is carried out on this research burner. This chapter also discusses the calibration burner used to establish LII operating parameters and measured soot profiles.

Chapter 5 introduces the challenges faced in imaging HFO droplets in a combustion environment. A novel LIF-based technique is then described to overcome these challenges. This technique is used to characterize HFO spray in a combustion environment, and various operating conditions for the HFO spray system are identified.

Chapter 6 deals with experimental studies on soot formation and emission from HFO spray flames using the LII technique for different spray conditions identified in chapter 5. This chapter presents the results and discussions on soot formation followed by TEM imaging studies of soot.

Chapter 7 discusses the results of the particle size spectroscopy technique used to study cenosphere emissions from HFO spray combustion. A statistical method is described to estimate the critical droplet diameter of HFO spray below which the cenosphere emissions are drastically reduced.

Chapter 8 concludes the present research work by summarizing the favorable conditions for smoke reduction. These serve as guidelines for HFO burner design.

2 Literature survey

A literature survey is conducted to document the current understanding of HFO combustion and the carbon particulate formation mechanisms. This chapter identifies the gaps in the literature regarding particulate formation in HFO spray flames thereby consolidating the problem definition for the present research work.

2.1 Soot Morphology:

Typically, all combustion generated particulate emission are referred as soot. However, these particulates are categorized based on their sizes and chemical composition as shown in Table 2.1 Classification of particulates emitted from HFO combustion

The carbon particulates formed during the gas phase combustion are technically referred as soot. Under an electron microscope, these appear as agglomerates of spherical particles termed primary soot particles. Chemically, primary soot particles are carbon-rich hydrocarbon compounds with about 90% carbon and 10% hydrogen. They are typically spherical in shape and exhibit a size range of 10-nm to 50-nm as shown in Figure 2.1 Images of different types of particulates

As described in Chapter 1, HFO contains traces of residual metal fractions. These metals form metal rich particulates during combustion called plerospheres [2]. Typically, they exhibit a size range of 0.05 to 1 micron and typically contain metals like vanadium, iron, copper, nickel etc. Carbon-rich, graphitic particulates larger than 1-µm size are called cenospheres [3]. These are mainly formed due to high-temperature pyrolysis of larger fuel droplets occurring in spray flames.

Particulates	**Size**	**Composition**
Soot (Gas phase)	20 nm to 500 nm	Carbon ~ 90% Hydrogen ~ 10%
Plerospheres	0.07 to 1 µm	Metal particulates containing V, Fe, Cu, Ni, Mn, Zn
Cenospheres	1 to 100 µm	Mainly Carbon, traces of Ash

Table 2.1 Classification of particulates emitted from HFO combustion.

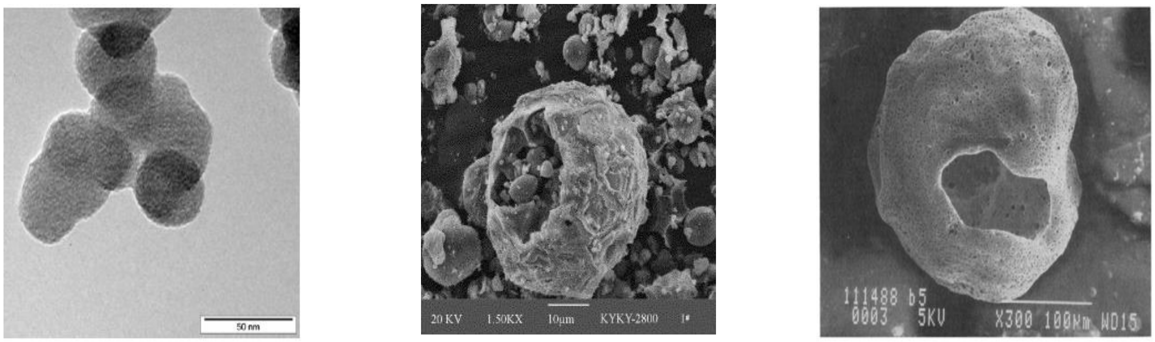

(a) Soot (b) Plerospheres (c) Cenosphere

Figure 2.1 Images of different types of particulates.

Most of the literature on HFO combustion is related to process heat burners, furnaces and boilers. A typical liquid-fueled combustion system consists of a fuel atomizer, which disintegrates a fuel jet into fine droplets facilitating rapid evaporation, a swirler to supply combustion air supply to mix the fuel vapour with the combustion air. A typical industrial burner consists of the following components:

1. Fuel atomizer with fuel supply system
2. Swirler with an air blower system
3. Flame ignitor
4. Flame tube

The combustion behavior of a fuel in a burner depends upon the physico-chemical properties of the fuel as well as the physical processes such as fuel atomization, evaporation, air entrainment and, flame stabilisation. The following sections focus on the understanding of these parameters to investigate particulate formation during combustion of HFO in industrial burners.

2.2 Combustion characteristics of Heavy Fuel Oil (HFO) in industrial burners

Heavy Fuel Oil is generally burnt in spray flames with preheated co-flowing combustion air using flame stabilizing mechanisms. The various flame stabilization techniques used in burners involve use of single swirler, multiple swirlers and stabilization plates. Generally, industrial burners are swirl stabilized burners and use pressure jet atomizers. The atomizer is centrally located and injects fuel in the form of a spray. Hot combustion air is supplied through the swirler. This hot air entrains in the fuel spray to achieve air-fuel mixture. This premixed air-fuel mixture is then burnt in the flame front region resembling a diffusion flame. The swirling air produces an internal re-circulating zone which entrains burnt gases with the incoming fresh fuel spray. This increases the temperature in the fuel-air mixing region, thereby enhancing the evaporation rate of fuel droplets. Generally, the design of burner and flow parameters are selected such that complete evaporation of fuel droplets is achieved before the flame front. Figure 2.2 shows a fluid dynamic phenomenon in a typical swirl stabilized spray flame and the trajectories of fuel particles in the presence of swirl.

Recently, there is a renewed interest in HFO combustion and particulate formation in marine engine applications and process heat boilers due to emission regulations. Efforts are being made computationally and experimentally to understand the effect of the combustion chamber, burner design and fuel properties on combustion characteristics and pollutant formation. The fuel properties and fuel atomization techniques have a substantial effect on drop size distribution and their subsequent evaporation. Since HFO is highly viscous with higher molecular weight, it is quite challenging to achieve a fine spray as compared to that obtained with conventional fuels such as diesel. Rosa et al. [4] experimentally studied spray and combustion characteristics of laboratory spray flames of diesel and HFO under similar operating conditions using a twin-fluid atomizer. They observed that HFO spray produces droplets that are around twice the size as compared to those droplets from a diesel spray particularly at the outer edges of the spray. Larger droplets were also recorded along the axis for HFO spray, while very fine droplets were produced along the axis for diesel spray. The diesel flames burn with characteristics of a gas diffusion flame (Refer Figure 2.3).

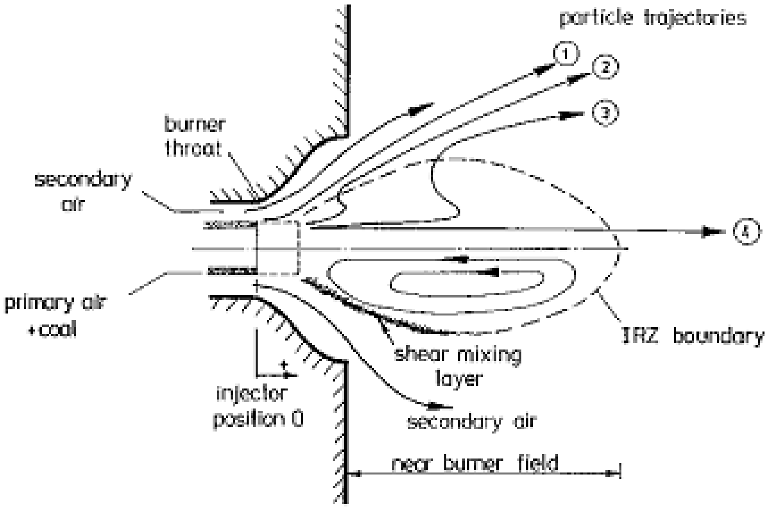

Figure 2.2 Fluid dynamic phenomenon in a typical swirl stabilized HFO burner [5].

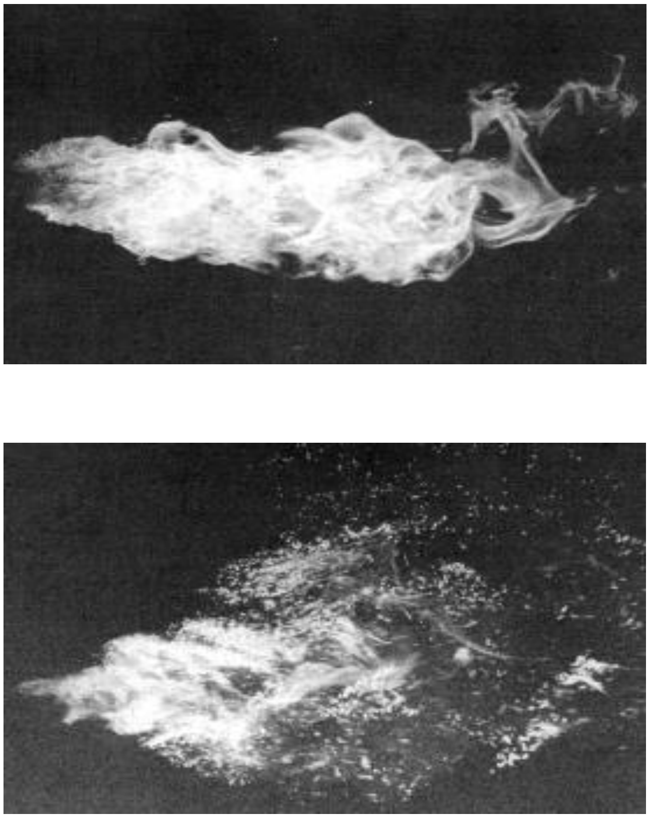

Figure 2.3 Swirl stabilized light diesel flame.

Figure 2.4 Swirl stabilized HFO flame .

While in the case of HFO, larger droplets penetrate through the flame region without getting completely evaporated thus producing a large amount of carbon particulates due to incomplete droplet combustion or droplet pyrolysis. Most of the HFO droplets burn in droplet combustion phase or in clusters (refer Figure 2.4) and results in the loss of combustion efficiency. Hence, it is necessary to design a combustion system which will provide sufficient residence time for droplets to undergo complete evaporation, combustion and thereby reduce particulate emissions.

High distillation temperature of HFO is a primary reason for the fuel droplet pyrolysis leading to formation of carbon-rich particulates called cenospheres. Miller et al. [6] experimentally analysed the particulate emissions generated in an industrial fire tube boiler using fuels with different sulfur content and viscosities. They observed a bimodal size distribution of the particulates formed with an insignificant effect of sulfur content on carbon particulate emissions. The fine particles in the size range of 0.07 to 1 micron mainly consist of residual metals and are called plerospheres. The broadly distributed coarse particles (from 5 to 100 microns) are mainly carbon-rich particles. These carbon particulates are generated even though the combustion efficiencies recorded are around 99.7%.

The coke/carbon rich particles generated by fuel droplets pyrolysis are the direct result of asphaltene content in the fuel. Asphaltene is the content in the fuel which is n-heptane insoluble. Park et al. [7] studied the particulate emission characteristics of the HFO and found that the coke formation index (CFI) of an HFO increases linearly with the asphaltene content of the fuel. The CFI represents the mass fraction of fuel droplet that gets converted into coke.

Due to the high viscosity of HFO and vacuum residues, it is difficult to finely atomize such fuels by conventional atomization techniques. Hence, water emulsions of HFO and vacuum residues are investigated by Tarlet et al. [4] and Chavez et al. [8]. When fuel is sprayed in a combustion chamber, the finely suspended water droplets in the oil rapidly evaporate, expand and causes the fuel droplet to explode, thus achieving secondary atomization and smaller SMDs as compared to pressure jet atomizers. They reported particulate emission reduction of the order of 20% to 30%. The potential of fuel atomization in the reduction of cenosphere emission is evident from this study.

Apart from effective atomization strategies, the air entrainment and flame stabilization by swirling air also play an important role in the combustion of HFO droplets. Many computational and experimental studies to understand the effect of operating parameters such as swirl number, excess air-fuel ratio, spray SMD on particulate, NOx and CO emissions have been conducted. Byrnes et al. [9] observed that decrease in spray SMD reduces the size of cenospheres generated initially which are eventually oxidized before chamber exit, thus reducing particulate emissions. However, the NOx emissions were found to be increased. With 15% excess air-fuel ratio, enhanced heterogeneous combustion of coke particles results in reduced particulate emission. However, this increase in excess air-fuel ratio also resulted in increased NOx emissions. The increase in swirl number (SN) from 1.05 to 1.2, resulted in a slight decrease in NOx and particulate emissions, but SN cannot be increased further due to flame stability constraints. It was concluded that the particulate and NOx emissions are mutually exclusive and by adjusting these operating parameters, only a compromise can be achieved. Similar results are reported by Yaun et al. [10]. Increase in SN intensifies recirculation in inner recirculation zone (IRZ) resulting in increased residence times for droplets in the flame region and consequently fewer particulate emissions. Excess air ratio lesser than 8% results in depletion of oxygen availability in the post-flame region for heterogeneous combustion thereby resulting in increased particulate emissions. They concluded that particulate emissions can be reduced by careful adjustment of operating parameters so as to increase the residence time of cenospheres in high-temperature regions of the furnace. Barreiros et al. [11] also suggested that the design of burner and operating conditions should be selected such that aerodynamics of near burner flow field provides rapid vaporization of fuel droplets in fuel-rich atmosphere formed by an intense IRZ followed by long residence times of primary fuel stream in IRZ to ensure maximum burnout.

The above studies indicate that some additional measures are required to reduce particulate emissions further without increasing NOx emissions. One way to keep NOx emissions low and avoid fuel bound nitrogen (FBN) conversion to NOx is air staging. In air staging, the combustion air is supplied in multiple stages. In the first stage, a fuel rich reducing atmosphere is maintained so that NOx formation is curbed due to lack of oxygen. The excess combustion air is suddenly mixed with this partially burned combustion products to oxidize unburnt hydrocarbons and quench the flame by lowering the temperature below 1200 °C so that no thermal NOx is generated. Such a configuration is experimentally investigated by Villasenor et al. [12] in a 500-kW HFO-fueled furnace. The primary zone was operated at 0.5% excess air and two secondary air jets are used to quench the burnt gases in the primary zone. A reduction in NOx emissions of around 71% as compared to that in a conventional configuration was observed, however, due to reduced temperatures in the secondary zone, the particulate emissions are high. This shows the temperature sensitivity of heterogeneous cenosphere combustion. One way to improve cenosphere combustion in the secondary zone is to add gaseous fuel with the secondary combustion air. Rebola et al. [13] investigated the effect of the mixing propane to primary atomizing air as well as secondary combustion air. Their experimental investigation on a 150-kW laboratory furnace revealed that combustion air staging is effective only in reducing NOx emissions while HFO atomization using propane-air mixture is effective in reducing both particulates as well as NOx emissions. Shihadeh et al. [14] demonstrated an aerodynamically-staged HFO combustor where the primary, secondary and tertiary air swirlers produced a radially stratified core flame. However, this concept is not as effective as external air staging in reducing NOx formation.

In most of the above experimental investigations, the particulate characterization is carried out by introducing a probe at appropriate locations. Recently, a laser-based non-intrusive optical diagnostic technique is developed, which can produce 2D field images by in-situ laser-based diagnostics called Laser Induced Incandescence (LII). Allouis et al. [15] applied time-resolved LII on HFO laboratory flames to measure particle size at different locations along the burner axis. They also reported qualitative soot volume fraction at different HAB locations. Based on LII signal decay characteristics, they inferred that the particle size distribution is bimodal with peaks centered at about 60-nm and 1-µm.

The literature discussed up to now is focused on formation and reduction of pyrolysis generated porous carbon particulates called cenospheres. Allouis et al. [2] characterized the Particle Size Distribution (PSD) of emitted particulates on a scaled-down industrial burner. The SEM (Scanning electron microscopy) and EDX (energy dispersive X-ray) revealed the presence of solid particulates accumulated in the range of 1-µm to 4-µm formed due to metallic residuals from HFO, which are called plerospheres. It was also noted that the metallic concentration in these plerospheres is independent of asphaltene content in the HFO. Linak et al. [16] presented PSD characterization of PM emitted by a 732-kW HFO-fired commercial boiler. The PSD is weakly bimodal with one sub-micron peak between 0.01-µm to 0.1-µm and super-micron peak between 10-µm to 100-µm. They concluded that the ultra-fine particulates are the outcome of the accumulation of condensing metal sulphates while, the large particulates are formed due to incomplete burnout of droplets.

Hence, we can conclude that for all practical HFO burners, the particulate emissions are weakly bimodal. There are two peaks, one of the plerospheres about 0.01 to 0.1 microns and another of cenospheres at about 1 to 100 microns. The nascent gas phase soot formed during combustion is very reactive and is completely oxidized due to higher temperature and residence times. The total particulate emissions can be reduced by using a different design and operating strategies as discussed above. However, it is difficult and expensive to develop and optimize practical combustion systems for low emissions. There are two ways to address this problem,

1. Developing a scaled down combustion system for a furnace and optimizing operating parameters to achieve maximum combustion efficiencies and lower emissions
2. Another is to use computational modeling and simulations; a powerful tool used nowadays to investigate different design configurations and also predict physico-chemical phenomena that are difficult to study with experiments.

2.3 Scaling of HFO fired Burners

For scaling of HFO fueled burners, it is necessary to consider the fluid flow, heat transfer, chemical reactions, multi-component & multi-phase mixing in the close vicinity of burner while defining the scaling laws. Many non-dimensional numbers such as Reynolds, Froude and Damkohler numbers are considered, but they are found to lead to conflicting scaling requirements [5]. Hence, from a practical standpoint, partial scaling rules are chosen keeping in mind the objective of scaling, i.e., thermal input, fuel penetration in mixing zone, NOx formation etc. The most frequently used criteria are constant velocity and constant residence time (convective time scale). From practical considerations of small-scale burners, the constant velocity criterion is the most favored, as the constant residence time criterion leads to very low combustion chamber pressures for small-scale burners and very high pressures for full-scale burners. Furthermore, pollutant formation is a major function of micro and macro scale mixing. The constant residence time criterion keeps the macro-scale mixing unaltered and in case of isotropic turbulence, the micro-scale effects can also be kept unaltered. The authors proposed that for scaling pollutant formation in different flames, the degree of mixing and reaction should be identical for different values of (x/D) (x= axial distance from burner face, D burner throat diameter).

In case of liquid fuel flames, another important parameter to consider is momentum ratio between fuel and air streams. The design of a fuel atomizer determines the droplet distribution and the spray momentum, and hence it is difficult to adjust the spray momentum for scaling. A scaling for swirl-stabilized liquid fuel flame can be achieved by scaling the internal circulation zones such that the fuel droplet penetration in the IRZ remains unaltered [17]. For such a criterion, the constant velocity or constant residence time scaling for the dimensions and the flow rates are found to give similar results. To maintain similar extent of fuel droplet penetration for scaled-down burners below 50-kW requires scaling the droplets to very fine sizes. It is also found that with a standard drop size distribution, small flames cannot be practically stabilized without a supporting fuel such as hydrogen. The above considerations are incorporated in the research burner designed for present research work.

2.4 Droplet combustion

Mathematical modeling has emerged as a powerful tool in designing of combustion chambers for furnaces. For successful predictions, it is imperative to understand the physical & chemical processes by which fuel droplet combustion produces cenospheres and subsequent oxidation of cenospheres occuring in the combustion chamber. This will enable us to generate mathematical models which can be implemented in CFD simulations for design and development of practical systems.

Such models are developed by studying the combustion processes involving isolated droplet combustion. Several studies are reported in the literature investigating the droplet evaporation behavior and rate, combustion rate, ignition delay, cenosphere formation and burning characteristics of coke particles. The coke particles or cenospheres are formed by pyrolysis of HFO droplets under high temperature. As the flame envelopes the burning droplet, it is a fair assumption that the droplet pyrolysis happens in an inert atmosphere. Bomo et al. [14] investigated pyrolysis of mono-dispersed heavy oil droplets with different asphaltene content at 1200°C in an inert nitrogen atmosphere. The droplet size was varied between 400 to 800 micron and the residence time was varied between 0.07 to 0.16 seconds. It is observed that cenosphere is formed inside the droplet and not on the surface of the droplet by carbonization; thus, each drop forms a cenosphere. The temperature at which it is formed is considerably lower than those required for soot formation during combustion. They proposed that the cenospheres formation is not related to total asphaltene content in HFO and mainly depends on the aromatic chemical structure of asphaltene compounds.

Similar observations regarding the formation of cenospheres are reported by Urban et al. [18] [19]. The droplet combustion in a drop tower revealed that the initial liquid phase combustion is disruptive. They proposed that micro-explosions during droplet combustion result in large blowholes on the solidifying coke shell thus explaining the porosity in cenospheres. Every droplet is assumed to generate a cenosphere particle, and the particle diameter depends upon the initial diameter of the droplet and mass fraction of heavy components. The total particulate mass generated is related to the fraction of heavy hydrocarbon content in the oil. The authors proposed CFI (Coke formation index) for distinguishing different fuel grades which is an estimate of the mass fraction of droplet converted into coke. It is also observed that the CFI index and concentration of n-heptane insoluble asphaltenes correlate very well with each other.

In general, the droplet burning characteristics such as ignition delay, ignition temperature, and combustion duration mainly depend upon the chemical composition of the fuel. It is a well-accepted theory that combustion of HFO droplets in a furnace takes place in two distinct phases; droplets phase combustion followed by solid coke combustion separated by a flame extinction event. The heavy components such as asphaltenes and large aromatics are responsible for coke formation. Villasenor et al. [20] studied the effect of asphaltenes with isolated HFO droplets in a highly radiative heating environment with heating rates up to 1000 °C/s. Based on the size and the temperature history of the burning droplets, they proposed four different regimes of droplet combustion and identified their characteristic times. The different regimes and their characteristic times for a 730-µm droplet are listed below,

1. Droplet evaporation and ignition delay (~ 300 ms)
2. Ignition, droplet combustion, and swelling (~ 250 ms)
3. Droplet contraction and coke formation (~ 50 ms)
4. Solid phase Coke combustion (~ 1540 ms)

The coke and total burnout time increased with the asphaltene content and the initial droplet diameter. They observed that HFO droplets with less aromatic content produce cenospheres with a thinner and fragile shell, which can be oxidized easily.

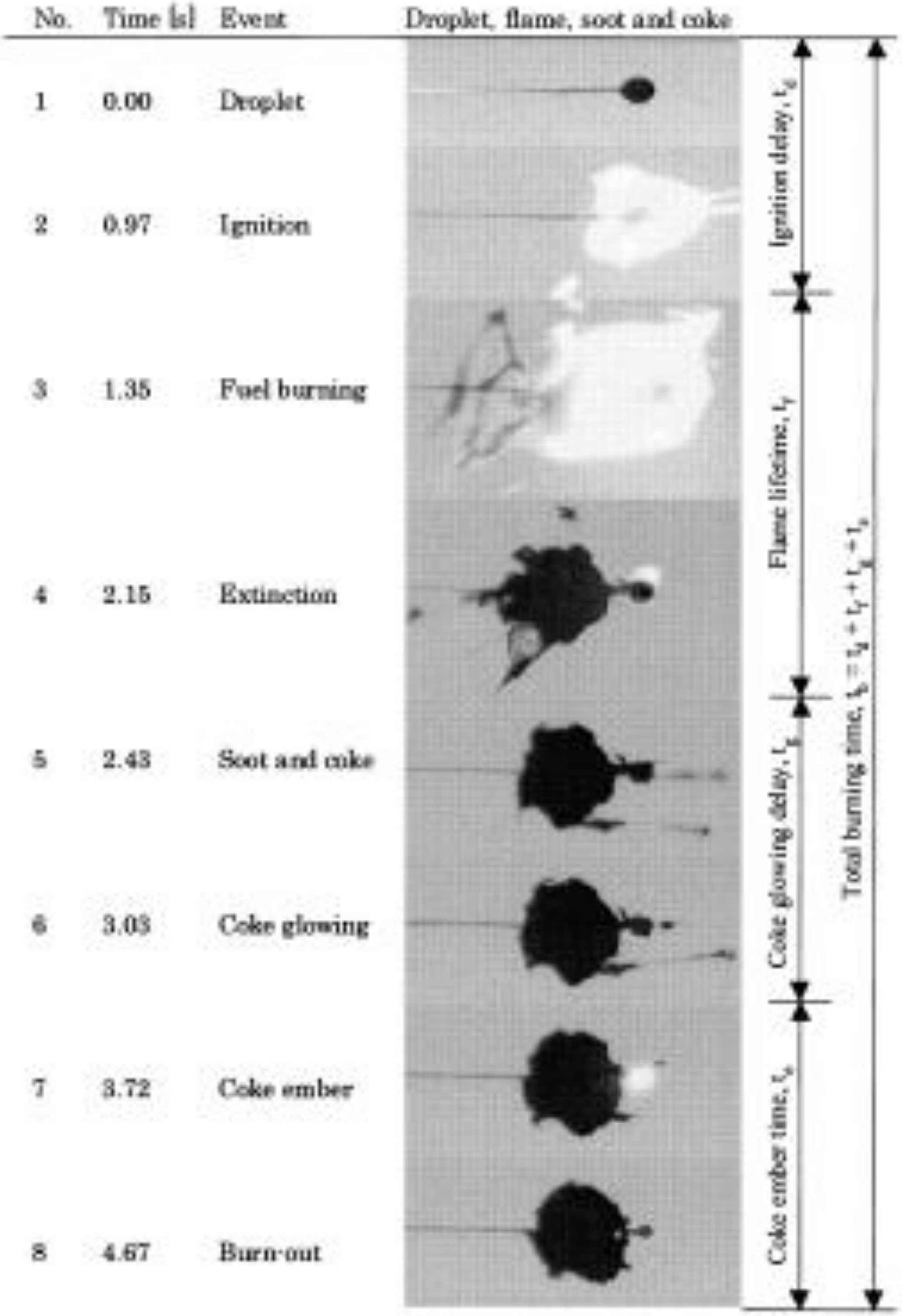

Figure 2.5 Different stages of droplet phase combustion for HFO droplets.

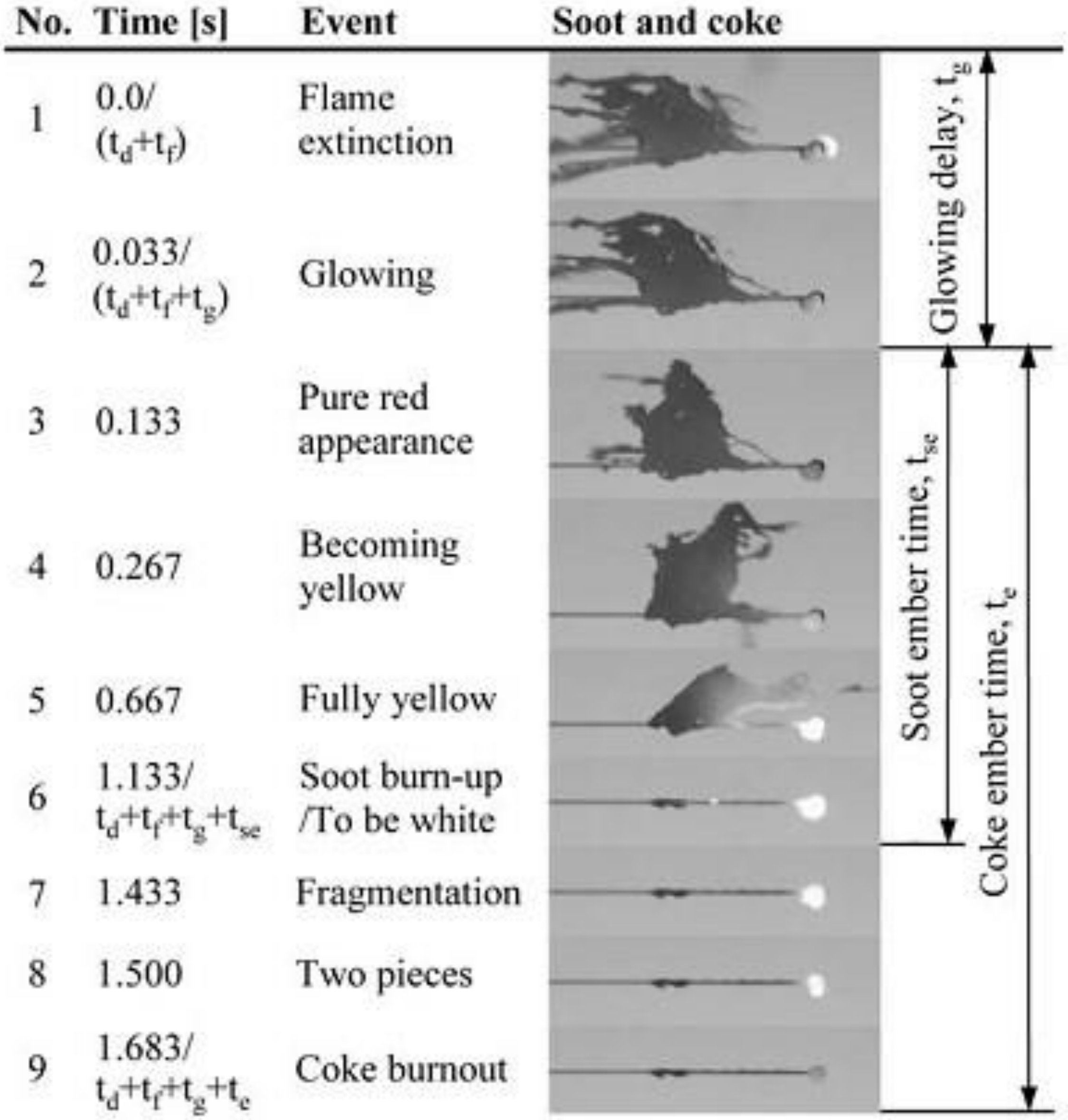

No.	Time [s]	Event	Soot and coke
1	0.0/ (t_d+t_f)	Flame extinction	
2	0.033/ $(t_d+t_f+t_g)$	Glowing	
3	0.133	Pure red appearance	
4	0.267	Becoming yellow	
5	0.667	Fully yellow	
6	1.133/ $t_d+t_f+t_g+t_{se}$	Soot burn-up /To be white	
7	1.433	Fragmentation	
8	1.500	Two pieces	
9	1.683/ $t_d+t_f+t_g+t_e$	Coke burnout	

Figure 2.6 Different stages of solid phase combustion regime of HFO droplets.

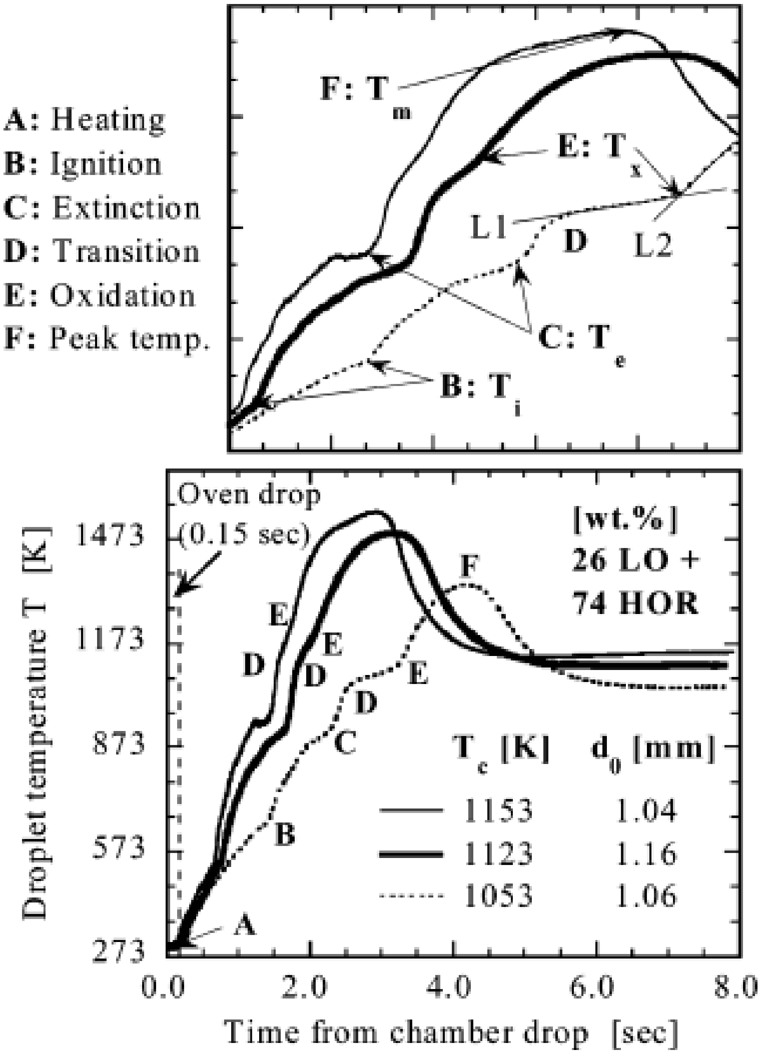

Figure 2.7 HFO droplet temperature variation during droplet combustion (refer Figure 2.5 & Figure 2.6).

Extending the above study for a more generalized HFO composition, Xu et al. [21][22] extensively studied HFO combustion characteristics and identified the onset of stages in combustion for isolated HFO droplets. Different HFO compositions were represented in a generalized form, i.e., blends of heavy oil residual (HOR) and light oil (LO). Based on the experimental data of size and temperature history, the various steps in the HFO droplet burning are summarized as follows and the series of events are shown in Figs. 2.5, 2.6 and 2.7.

The HFO droplet undergoes combustion in two phases, liquid phase combustion (1 to 4) followed by combustion of solid phase coke (5 to 8). The combustion phenomena of the HFO droplet can be briefly described as shown below,

1. Droplet phase combustion:
    1. As the droplet is exposed to sufficiently high temperatures, the volatile fractions start evaporating and get mixed with the surrounding air.
    2. If the surrounding temperature is greater than self-ignition temperature (~ 600 K), the air-fuel mixture surrounding droplet undergoes spontaneous ignition after a time delay of t_d and a visible flame is formed.
    3. The radiative and convective heat transfer between the flame front and droplet surface causes further heating of droplet and volatiles generated by evaporation and thermal cracking keep the flame burning. At later times in this phase, disruptive behavior of burning droplets including satellite droplet formation has also been observed. The duration for which flame is visible surrounding the droplet is called volatile flaming duration.

    4. Large amounts of lumps of soot (from gas phase combustion) are generated during combustion of volatiles. This is visible as a black smoke cloud.
    5. Consequently, the flame extinguishes (~ 1100 K) and coke residue appears on the tip of the thermocouple.

2. Solid phase combustion:
    1. The coke residue sticks to the wire. The temperature of this particle keeps on increasing due to radiant heating.
    2. As the particle temperature reaches around 1150 K, the coke starts oxidizing and particle glows with yellow in color. The time period from extinction of visible flame till coke glowing is termed as coke glowing delay. The coke glowing delay is found to be independent of HFO composition and coke particle size.
    3. The coke continues to burn slowly, while soot being more reactive, burns faster. The combustion of coke happens within the solid particle and not on the surface. The coke particle interior temperature rises to 1450 K. Though the soot burns off completely, the carbon-rich coke particle remains after coke burnout. This porous carbon-rich particle is termed as cenosphere.

The noteworthy observations made in the above study are as follows:

    1. The time durations for different stages (discussed above) have a huge impact on the burner and combustion chamber design. The duration of the ignition delay, the flaming duration, the coke glowing delay and the coke burnout duration are estimated from the temperature history of a burning HFO droplet. Out of these durations, the coke burnout duration (~ 40 – 60%) overwhelms the total droplet burning duration at

practical combustion chamber temperature of 1200 K. This indicates that the ignition delay should be considered for as design criterion for burner design while the coke burnout duration should be considered for combustion chamber length rather than the volatile burning time.

2. With lower chamber temperature (1058 K), the soot lumps do not glow until the coke burnout. However, with higher chamber temperature (1153 K), the coke and soot started glowing simultaneously. This shows that the ignition of soot requires a higher temperature than coke. However, the burnout duration of soot is substantially lesser than that of cenospheres. Hence, the solid burning stage is dominated by coke burnout time. In actual burners, soot burning occurs simultaneously with the fuel burning in the recirculation region. For developing a computational model of solid phase combustion, only cenosphere oxidation can be modeled without considering soot oxidation.

3. With the decrease in LO fraction (volatile fraction), both ignition delay and coke glowing delay decrease considerably. The flaming duration decreases slightly. The coke burnout time was also found to be constant irrespective of LO fractions for LO > 30%.

4. With higher chamber temperature of 1200 K as compared to 1000 K, the ignition delay and the coke glowing delay are considerably reduced, however, total combustion duration remained the same. The coke particles formed at higher chamber temperatures were found to have higher density, smaller in size and less porosity than those formed at lower chamber temperatures.

5. The total burning duration is found to vary linearly with droplet diameter than the second power of diameter (D^2 law). Interestingly, the volatile flaming duration correlated well with the second power of diameter.

Useful information on HFO droplet combustion phases and timescales have come out of these experiments. It is well-established that the solid phase burning occurs via heterogeneous surface oxidation, which takes more time than the droplet combustion phase. However, the liquid phase burning is more complicated to describe in terms of physical and chemical mechanisms involved. It is postulated that liquid phase combustion can be divided into four sub-stages namely, pre-ignition heating, evaporation of volatiles, thermal cracking of heavier components and polymerization to form coke. Recently, Ikegami et al. [23] conducted micro-gravity HFO droplet combustion experiments to identify liquid combustion stages. The absence of gravity eliminated the effect of convection driven mass and heat transport, thereby having little effect on the droplets temperature history and size. Thus, the various phenomena occurring during the droplet phase combustion can be derived from the temperature-time curve. The sample temperature and size history for an HFO droplet are shown in the Figure 2.8. The distinct stages and the related phenomena identified are described as shown below:

1. Pre-ignition and heating stage: Due to heating by higher surrounding temperature, the droplet temperature rises till the event ‘A', which is identified as an ignition point. There is a slight increase in diameter due to thermal expansion of oil. During this heating period, the volatiles continue to evaporate and form a cloud surrounding the droplet.
2. After ignition, a rapid rise in temperatures is observed with increased swelling of droplets. There is a continuous rise in temperature and no disturbances are observed in

size history as well as the surface of the droplet. The droplet evaporation is similar to multi-component distillation. This stage is denoted by ‘A' to ‘D'.

3. Inner evaporation stage: The temperature and size histories indicate the presence of a distinct stage of inner evaporation and are situated between A and D events. This is identified by the point of inflection in the temperature history. The stage from A to B corresponds to the surface evaporation with multi-component distillation. The stage from B to C corresponds to volumetric evaporation of volatiles as the droplet temperature is well above saturation temperatures of the lighter components. The rate of temperature rise is slower even in presence of a surrounding flame front. This indicates high evaporation rates due to higher enthalpy absorption. The vapor bubbles are formed inside the droplet. The splashing and slight disturbances on the burning drop surface indicate that vapour bubbles near the surface are able to escape due to lower viscosity. While the sharp rise in droplet size from B to C indicates that, the bubbles formed near the center are not able to reach the surface, they coalesce and expand the droplet. The sudden drop in droplet size from stage C to D is a result of a micro-explosion. After stage C, the temperature starts to rise at a faster rate due to depletion of volatiles till the next inflection point D. It is clear that inner evaporation is dominated by the volatile content in oil.

4. Thermal decomposition: The end of vaporization stage is marked by D. The reduction in temperature rise rate marks the onset of a new stage of thermal decomposition. The presence of inflection in droplet temperature curve rise shows large endothermic reactions taking place in presence of the flame front. This temperature is higher than the distillation temperature of lighter components, i.e., 700 K. This can be explained by

thermal decomposition of the heavier components. Decomposition of heavier components gives rise to vapors of lighter components which sustains the flame. The rate of increase of droplet temperature keeps on increasing indicating that the cracked components become heavier as this decomposition process continues. The fuel decomposition produces a high viscosity shell on the surface of the droplet resulting in entrapment of gases generated by decomposition. This results in frequent micro-explosions, fuel satellites, and violent droplet activity. This stage also witnesses a peak in droplet size due to volatile gas generation, which then decreases till F with the progress of decomposition.

5. Polymerisation: After thermal decomposition, the droplet temperature and the droplet heating rate start increasing drastically. From the image data, the droplet starts expanding for the last time before extinction. The droplet surface begins to appear as that of a coke particle. The droplet thermal decomposition takes place simultaneously along with the polymerization. The evolution of gases again increases the size of the droplet which is followed by sudden contraction due to condensation of the solid particle. The temperature monotonously rises to a peak droplet temperature due to the absence of evaporation. The peak temperature also coincides with the temperature at the flame extinction event. The polymerization temperature identified from the inflection point in the temperature-time curve is around 840 K and is independent of the fuel composition.

Some more important observations made in the above study are as follows:

1. With the decrease in initial droplet diameter (1.52-mm to 0.9-mm), the distinction between the different liquid combustion stages is observed to reduce. As expected, the

characteristic temperatures are found insensitive to initial droplet sizes and are mainly a function of the chemical composition of the fuel. The ignition delay, which depends upon the amount of fuel evaporated, increases with increase in initial diameter.

2. The thermal decomposition and polymerization temperatures were almost independent of fuel composition while the evaporation temperature decreased with increase in lighter fractions.
3. The HFO droplet evaporation is dominated by an evaporation process similar to the multi-component distillation due to rapid mass transport within droplets caused by disruptive burning.
4. The single droplet combustion studies revealed the physical mechanisms and possible chemical reactions by which HFO droplet burns and turns into a coke particle. The rate of combustion, the total burn-out duration and their dependence on initial droplet diameter is a very important parameter for designing practical burners. It is found that the total combustion duration varies almost linearly with initial droplet diameter as opposed to linear dependence on the square of the droplet diameter as shown in Figure 2.9.

With the above understanding, it is possible to adopt mathematical models describing each stage. A Heavy Fuel Oil (HFO) can be considered as an equivalent mixture of diesel (light oil) and asphaltenes (heavy oil residual). The combustion mechanisms for diesel are well understood. However, to successfully predict combustion behavior of HFO spray flames and carbon particulate emissions, more information regarding the chemical composition, decomposition and polymerization mechanisms of asphaltene is required. A detailed discussion on chemical composition and physio-chemical properties can be found in a study by Garaniya [24]. The experimental work on fast pyrolysis of heavy fuel oil droplets by

Moszkowicz et al. [25] explains the kinetics of HFO droplet combustion. They postulated that during droplet combustion. there is a competition between the kinetics of vaporization and solid coke formation to consume the fuel. Furthermore, it is noted that the rate of pyrolysis increases with the furnace temperature.

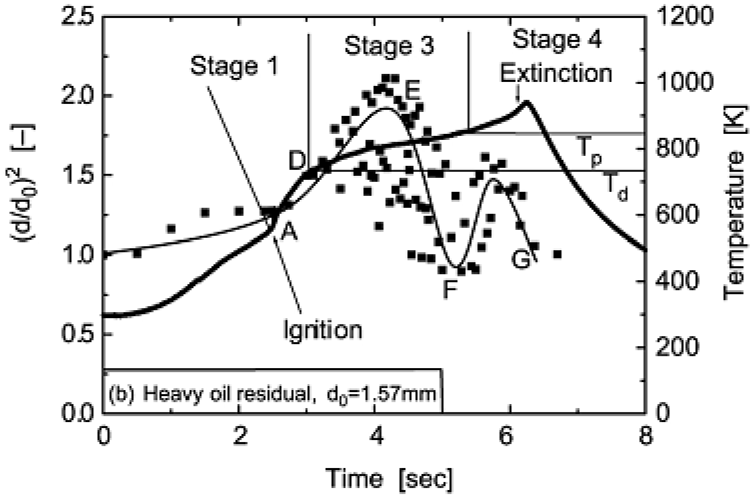

Figure 2.8 HOR droplet temperature and diameter history during combustion under microgravity conditions.

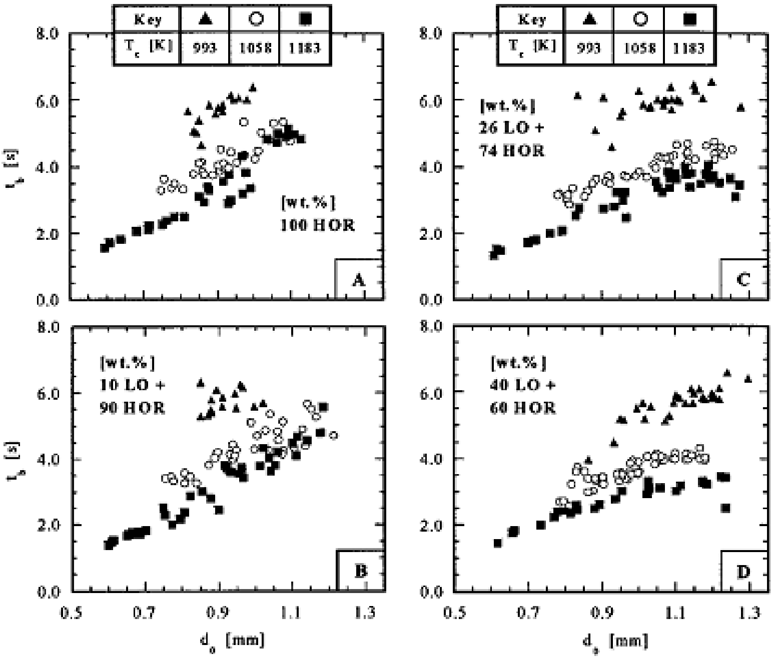

Figure 2.9 Variation of the total burn-out time period with initial droplet diameter for different mixtures of Light oil (LO) and Heavy oil residue (HOR).

Bartle et al. [3] based on their single droplet combustion studies and the chemical composition analysis of burning drop at different stages proposed that asphaltene compounds are also generated during droplet combustion and the amount of increase depends upon the initial asphaltene content. A recent work on thermal cracking and combustion kinetics of asphaltenes by Murugan et al. [26] has reported the following observations:

1. Coke formation depends upon the pyrolysis temperature and the heating rate. As the pyrolysis temperature and the rate of heating increases, the mass of residual coke formed reduces.
2. The amount of coke formation in inert gas pyrolysis experiments is more than that produced in experiments with air.

3. In case of non-isothermal pyrolysis, the rate of asphaltene decomposition and oxidation increases with the rate of heating.

In a practical flame, the gas temperature in a furnace is about 1200 K and the HFO droplet size ranges from 20-μm to 200-μm. Hence, the heating rates experienced by HFO droplets when injected into a flame are of order 10000 °C/s [26]. A typical HFO spray droplet distribution and the combustion-generated particulate size distribution are shown in Figure 2.10 [26]. The authors have stated that the particulate size distribution seems to confirm the theory that one droplet produces one cenosphere. However, it is not clearly evident from the droplet and particle size distributions.

2.5 Summary and scope of present work

Based on the above literature survey, it is widely accepted that a HFO droplet burns in two phases, droplet phase combustion followed by solid phase combustion. This seems to give credence to the theory that 'one HFO droplet produces one cenosphere'. The heavier components such as asphaltenes and aromatics are primarily responsible for coke or cenosphere formation. However, when smaller drops (~ 25 micron) are injected in hot combustion environment (~ 1000 - 1400 K), the droplet may undergo simultaneous evaporation, thermal cracking, and coke formation. Hence, a possible scenario of competition might exist between evaporation, thermal cracking, and the solid coke formation mechanisms. And thus, there exists a probability that a droplet burns out completely in the droplet combustion phase without coke particle or cenosphere formation. Hence it is necessary to investigate the effect of droplet diameter on combustion and subsequent cenosphere formation.

The subsequent chapters describe the research burner designed to investigate HFO droplet combustion in a spray environment and the experimental methodology adopted to study the dependence of initial droplet diameter on cenosphere formation.

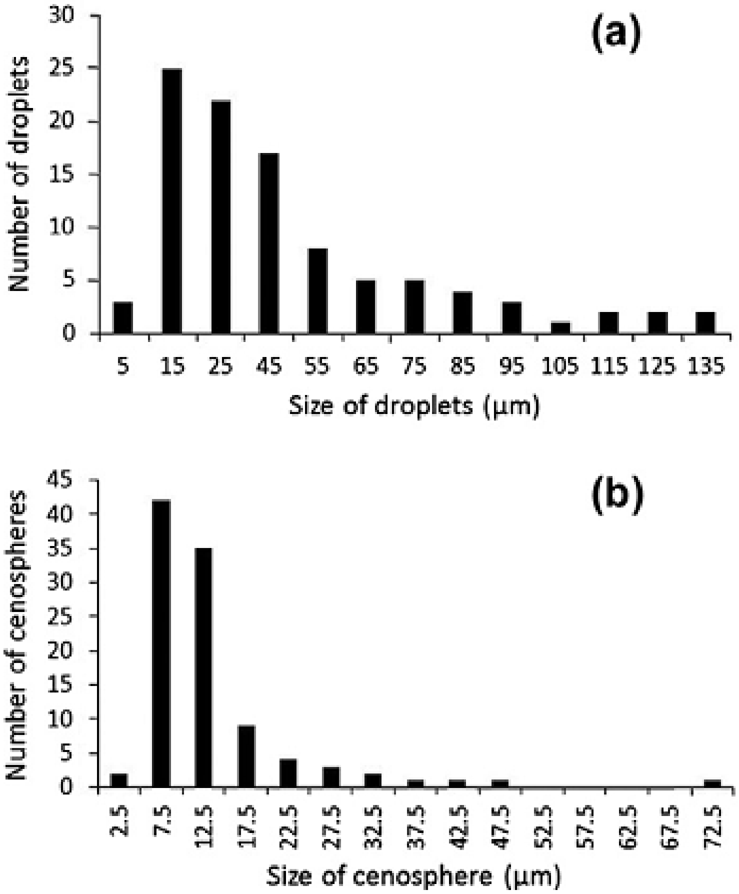

Figure 2.10 Distribution of droplet size and cenosphere size formed from combustion HFO with 9 wt % asphaltene in laboratory scale furnace [3].

3 Experimental techniques

In a combusting spray environment, a droplet experiences a complex interplay of the boundary layer, transient heating, convective evaporation, and combustion. To investigate such complex physics, various non-invasive laser diagnostic techniques such as LII, PDIA, PIV are used. One of the objectives of this research is to investigate carbon particulate emissions from HFO spray flames. A particle sizing technique called 'Aerodynamic particle size spectroscopy' is used to characterize particulate emissions. This chapter briefly introduces these experimental techniques, the corresponding equipment and operating parameters used.

3.1 Laser Induced Incandescence (LII) technique

LII is an in-situ planar laser diagnostic technique, which is used to measure soot concentration in a flame. The following sections describe a detailed overview of this technique and identifies important experimental parameters.

3.1.1 Introduction to LII technique:

The understanding of the processes of soot formation, and hence the strategies for its reduction, highly depends upon the capabilities to measure in-situ soot distribution inside the flames. For this purpose, an experimental method should be capable of providing information regarding the amount of soot (soot volume fraction), its spatial variation during the combustion processes and its temporal evolution. A two-dimensional temporally-resolved LII imaging technique largely matches such requirements.

Following the pioneering works of Eckbreth [27], Melton [28] and many recent papers [37, 38, 39, 40, 41] the potential of the Laser-Induced Incandescence (LII) technique as a planar soot visualization technique has been well-established. Although the basic principles of this technique are well understood, several uncertainties are still to be addressed for a complete theoretical description of this method. In spite of these uncertainties, quantitative measurements have been performed in a variety of experimental conditions and practical applications.

3.1.1.1 Theoretical consideration of LII technique:

A planar LII technique produces single-shot planar soot distribution images of a flame. As a primary interaction, a high energy laser pulse is introduced into flame causing the soot particles to absorb these laser photons and get heated to very high temperatures (~ 4000 K). This heat absorbed is lost due to different heat loss mechanisms such as evaporation, conduction to surrounding gas, annealing and radiation. The thermal black body radiation from these soot particles at such high incandescence temperatures is used as a signature of soot presence (Refer Figure 3.1).

A detailed theoretical description of this process was first reported by Melton [28] and recently a detailed theoretical model has been presented by Bladh et al. [29]. Some of the simplifying assumptions used in the interpretation and processing of the signals are listed below:

1. Soot is an aggregate of spherical primary soot particles; thus, any soot particle can be described as N_pD_p.
2. Evaporation is the dominant heat loss mechanism for all soot particles at characteristic incandescence temperatures.

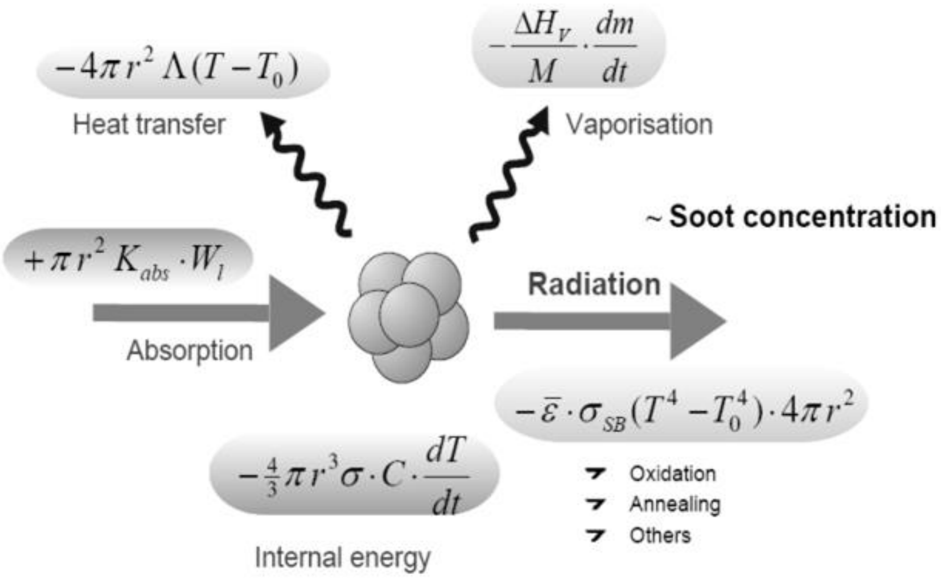

Figure 3.1 Laser interaction with soot particle and different heat loss mechanisms.

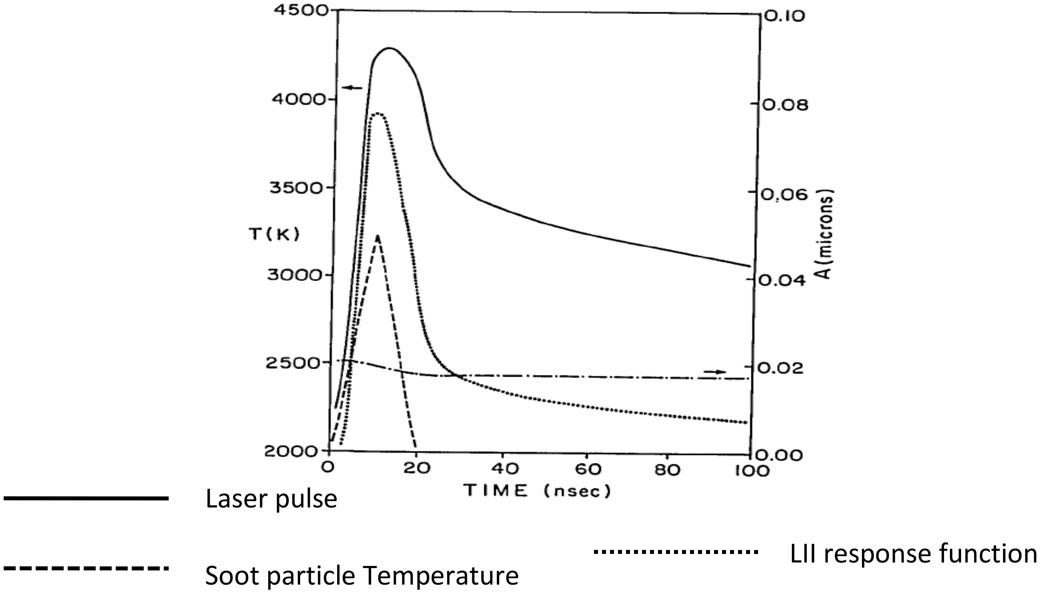

Figure 3.2 Predicted LII signal response function.

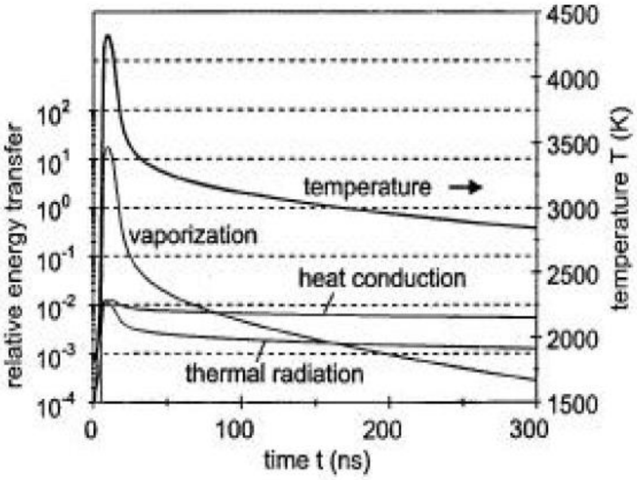

Figure 3.3 Comparison of rate of heat loss by different mechanisms after the laser pulse.

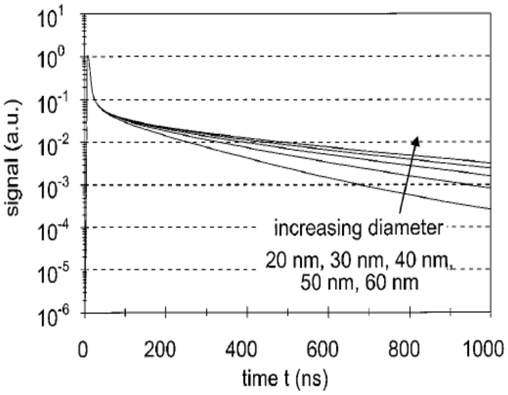

Figure 3.4 Normalised temporal LII signal for different primary particle sizes.

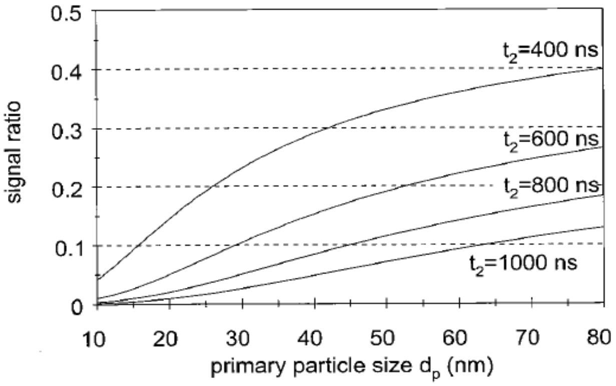

Figure 3.5 Ratio of LII signal at different t_2 times and its dependence on primary particle size.

By mathematical modeling of the photon absorption process and the subsequent heat loss mechanisms, the temporal temperature and the radiation signature is calculated [28] [30]. Figure 3.2 shows the laser pulse duration, soot particle temperature, and the predicted LII signal, while Figure 3.3 shows the order of magnitude comparison of different heat loss mechanisms. As assumed, the evaporation heat loss is dominant during the laser pulse, however, it sharply drops and the conduction heat transfer becomes a major heat loss mechanism subsequently. It is observed that during the dominant evaporation heat loss regime, a strong LII signal is emitted while during dominant conduction heat loss regime, emitted LII signal shows a slow temporal decay.

For the prompt LII signal detection (i.e. LII signal detection during laser pulse), theoretical model predicts that,

$$Prompt\ LII\ \propto (N_p D_p)^x \tag{3.1}$$

where, x= $3 + (154 / \lambda_{det})$ and λ_{det} is the detection wavelength (in nm) of broadband LII signal.

Thus, with proper choice of detection wavelength, the D^3 dependence of LII signal is obtained. The prompt detection of LII signal enables us to estimate soot volume fraction distribution in the laser plane. The temporal radiation signature is dominated by heat conduction to surrounding gas and is a surface phenomenon. Hence, the LII temporal signal is biased towards the larger particles, as the smaller particles have more surface to volume ratio and hence they cool faster than the larger particles as shown in Figure 3.4 [31].

Will et al. [31] proposed that this particle bias can be utilized to determine primary particle size evolution along the flame length. The ratio of LII signal at two different times (t_1 and t_2) is used to determine the primary particle size. As shown in Figure 3.5, after the delay of

100-ns from the initial peak, during which the evaporation dominates, the LII signal is still independent of particle size. This time is termed as t_1. On the other hand, t_2 is any time later than t_1 from the initial peak, when LII signal is captured again. The signal ratio for different t_2 durations from the laser shot with respect to different primary particle diameter is shown in Figure 3.5. This shows that with t_2 = 1000 ns, the signal ratio is linearly proportional to D_p. However, the due to the large delay of 1000 ns, the absolute signal intensity is very low.

Recently, Bladh et al. [29] presented an advanced mathematical model for LII signal prediction using more detailed heat transfer models with an objective to understand the inherent particle size dependence of the LII signal. They observed that the LII signal is better represented by Equation (3.2).

$$S_{LII} \propto \pi D^2 N_P \int_0^\infty R(\lambda') \frac{4\pi D E(m)}{\lambda'} \frac{2\pi h c^2}{\lambda'^2} \left(\frac{1}{e^{\frac{hc}{\lambda' k_B T}} - 1} - \frac{1}{e^{\frac{hc}{\lambda' k_B T_g}} - 1} \right) d\lambda' \qquad (3.2)$$

where,

D = primary soot particle diameter,

N_p = number of primary particles per soot aggregate,

λ = the laser wavelength,

E(m) = the absorption function,

h = the Plank constant,

c = the speed of light,

k_B = the Boltzmann constant,

T = soot particle temperature,

T_g = ambient gas temperature.

The explicit D^3 dependence of LII signal is evident from Eq. 3.2. The λ_{det} scaling found in Milton's model appears here as a scaling factor for soot temperature. The original D^3 dependence is a result of the temperature dependence of the surface heat transfer processes such as radiation and conduction. Hence, care should be taken while using simplifying assumptions in the estimation of soot volume fraction and primary particle determination, as a significant error is introduced by the oversimplifying mathematical model. A detailed model for temporal LII signal calculation is available elsewhere [30].

3.1.1.2 Experimental setup and operating parameters:

A typical LII experimental setup is shown in **Error! Reference source not found.**.

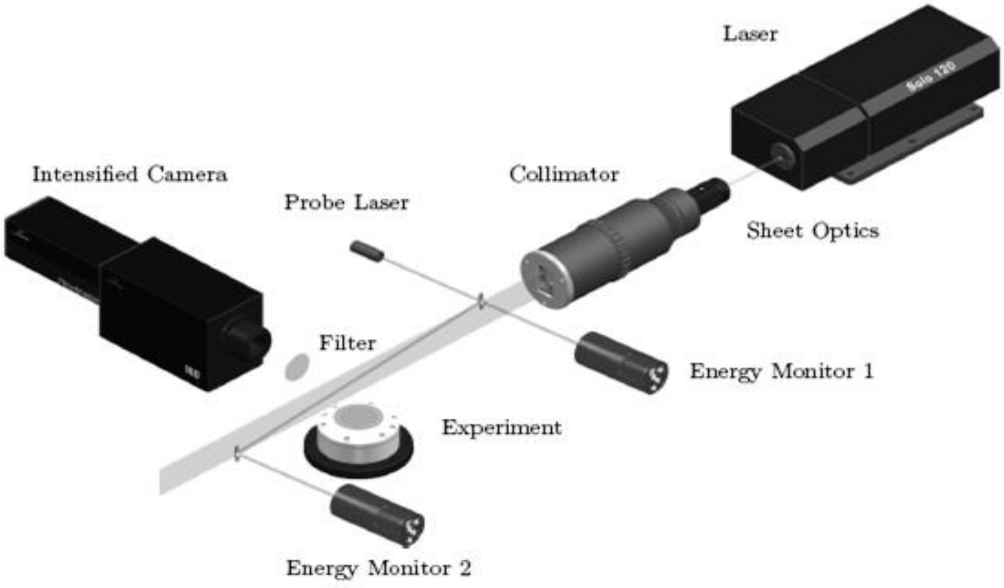

Figure 3.6 Typical LII experimental set-up [32].

In the LII technique, high-powered pulsed lasers are employed. Using the sheet making optics, a laser sheet of uniform energy density is produced which is passed through the flame under investigation. An intensified CCD camera along with an appropriate detection wavelength narrow band pass filter centered at 400-nm, FWHM 50-nm is used to capture the planar prompt LII images. As the LII image produced represents a relative picture of soot volume fraction (Eq. 3.1), a calibration is required to obtain quantitative soot volume fraction (SVF) information. A laser extinction technique, which is a line of sight method, is typically used as a calibration technique for LII images. It gives a single point absolute soot volume fraction value which is then used to scale the LII intensity images. Based on the literature, the following are the important operating parameters of the LII technique:

- Laser excitation parameters:
    i. Laser intensity or fluence
    ii. Excitation frequency
- LII Signal Detection parameters:
    i. Detection frequency
    ii. Detection duration and strategy

Laser excitation intensity:

As discussed earlier, all the soot particles in the investigation volume should reach incandescence temperatures such that evaporation is the dominant mechanism of heat loss. Hence, sufficiently high laser intensities are necessary. Many studies have reported that the LII signal increases with increase in laser intensity and then saturates forming a plateau region and then falls as shown in **Error! Reference source not found.** [33][34]. Due to the necessity of high laser power for LII, pulsed Nd:YAG lasers are generally employed.

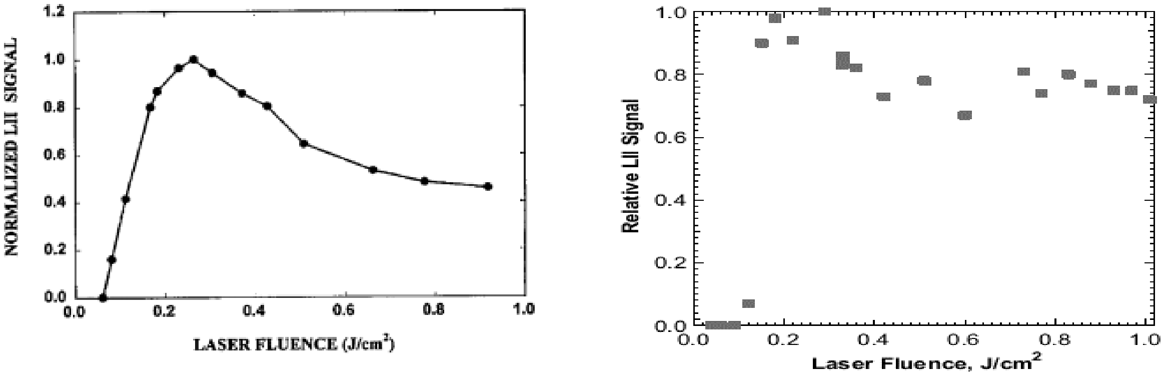

Figure 3.7 Effect of laser fluence on LII signal [33] [34].

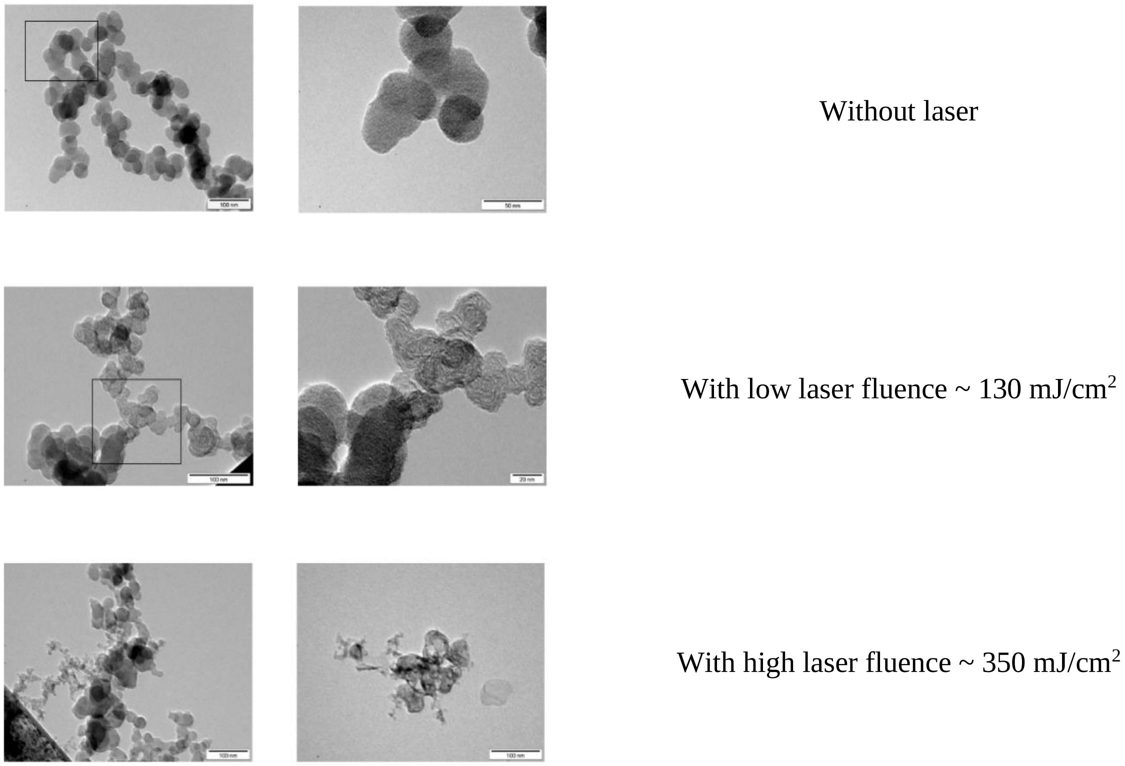

Figure 3.8 Morphological changes in Soot due to laser pulse heating [35].

Hence, we have excitation laser wavelength options in multiples of the harmonics of the 1064-nm Nd:YAG fundamental frequency. However, it is also observed that these high-power laser pulses result in annealing of soot particles and thus changing their optical properties as well as surface areas as shown in **Error! Reference source not found.** [35]. Hence, a laser fluence of 0.1 J/cm^2 for the 1064-nm laser excitation wavelength and 0.12 J/cm^2 for the 532-nm laser excitation wavelength are used to minimize the morphological changes to the soot [30][36].

Laser excitation wavelength:

An appropriate laser excitation wavelength is chosen such that it minimizes fluorescence interferences. Soot by nature is a broadband absorber. However, it is observed experimentally that UV lasers cause photo-dissociation of soot even at low energies. As discussed in the previous section, Nd:YAG lasers are commonly used due to high laser intensity requirements. Hence, we need to make a choice between the fundamental frequency of 1064-nm and the frequency-doubled harmonic of 532-nm. Polyaromatic hydrocarbons (PAH) are broadband absorbers and they are found in all sooty flames. They typically fluoresce due to excitation by the 532-nm laser pulse, giving out a broadband emission. This contaminates a very large band of detection wavelengths. De Luliis et al. [37] found that with 532-nm excitation and detection at 450-nm, around 80% of the LII signal is contaminated by fluorescence from PAH as shown in **Error! Reference source not found.**.

Wainner et al. [38] and Michelsen et al. [39] observed that at high laser excitation fluences of the 532-nm beam, the evaporated species such as C_2 and C_3 produce excitation bands as shown in **Error! Reference source not found.**. No such predominant fluorescence and excitation band interferences are observed with 1064-nm excitation over a large range of laser fluences. However, with lower laser fluences (< 0.3 mJ/cm^2) for 532-nm and 1064-nm, the fluorescence and excitation band signal contributions are minimal. Also, from a practical standpoint, using a visible beam (532-nm) is far more convenient than using an infrared beam (1064-nm). Hence, most researchers have used a 532-nm laser at lower fluences for the LII technique.

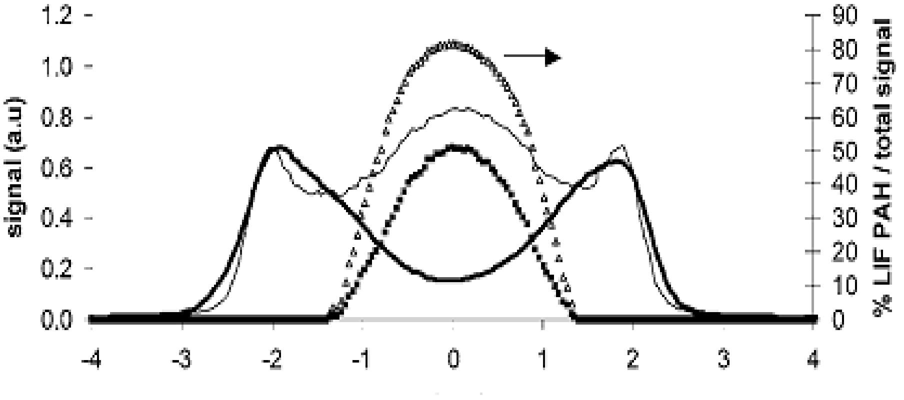

Figure 3.9 Fraction of LII signal contributed by PAH fluorescence with 532 nm excitation wavelength [37] where, Thin line: λex=532nm λdet=650 nm, Thick line: λex=1064 nm λdet=410 nm, Squares: PAH LIF from 2-color LII, Triangles: % contribution of LIF to LII.

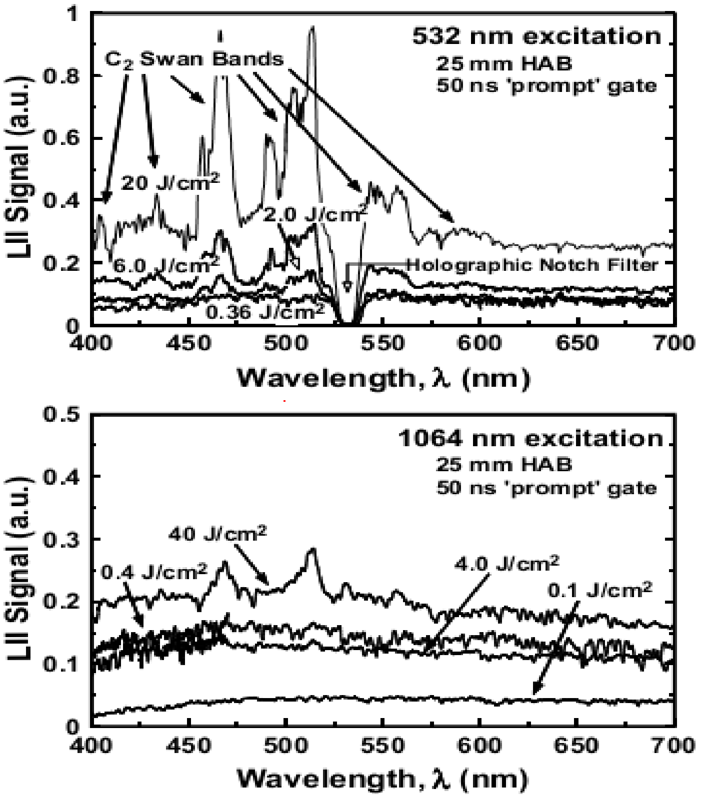

Figure 3.10 Spectral LII signal with 532nm and 1064 nm excitation wavelengths.

Detection wavelength:

Soot is also a broadband emitter, just as a black body. Hence, a wide wavelength detection window is available to detect the LII signal. However, as pointed out in the previous sections, the detection window should be selected such that predominant interferences are avoided. The LII spectral signal obtained by 532-nm laser pulse excitation is shown in **Error! Reference source not found.** [40]. For lower laser fluence using the 532-nm beam, a detection window centered at 400-nm is desirable. With a 400-nm detection window, one can also avoid flame luminosity of the sooty flames. Hence, lower detection wavelengths from 380-nm to 450-nm are widely used for the LII signal detection. However, for detection below 400-nm, UV optics are required. Furthermore, simultaneous two wavelength-based (two-color) measurements utilising 397-nm and 783-nm are being used for accurate soot particle temperature and volume fraction estimation.

Detection strategies:

A detection strategy constitutes selection of signal integration time (or camera exposure period) and temporal position with respect to the laser pulse. Based on the objective of the measurement, i.e., soot volume fraction or primary particle diameter, different strategies are employed. Randall et al. [41] carried out a detailed study of various detection strategies as shown in **Error! Reference source not found.**.

From theoretical considerations, it is known that prompt detection, i.e., signal integration coinciding with a laser pulse, results in LII signal proportional to soot volume fraction. The temporal LII signal evolution contains information on the primary soot particle size. To deduce the particle size information, an LII signal is captured twice with an integration time of about 10-ns. These two detections are temporally delayed by 100-ns and 800-ns than the laser pulse. The duration of signal integration is determined by considering excitation frequency, excitation intensity scattering, detection wavelength and expected interferences. For excitation with 532-nm, to reduce PAH fluorescence and C2 & C3 interferences, a low fluence of 0.12 J/cm^2 is employed while the signal integration time for prompt detection is 40-ns.

LII Signal evaluation:

LII technique is primarily developed to extract soot volume fraction (SVF) from the prompt signal and soot primary size distribution from the temporal signal. To derive quantitative information of soot volume fraction from planar LII image, signal intensity calibration to quantify SVF is necessary. A calibration constant is generally determined by a line-of-sight extinction measurement and is mathematically described as follows [42]:

$$f_v = \left(\frac{\lambda}{6}\,\pi\, L\, E(m)\right) \ln\left(\frac{I_0}{I}\right) \tag{3.3}$$

where,

$$E(m) = -Im\left[\frac{(m^2-1}{m^2+2}\right] = \frac{36\pi nk}{(n^2-k^2+2)^2+4n^2k^2} \tag{3.4}$$

where,

λ = light beam source wavelength,

L = length over which light extinction happens,

$E(m)$ = emissivity soot particle,

I_0 = Initial light beam intensity,

I = Final light beam intensity after extinction,

m = Complex refractive index of soot particle and

$m=n+ik = 1.57\text{-}0.52i$ [42].

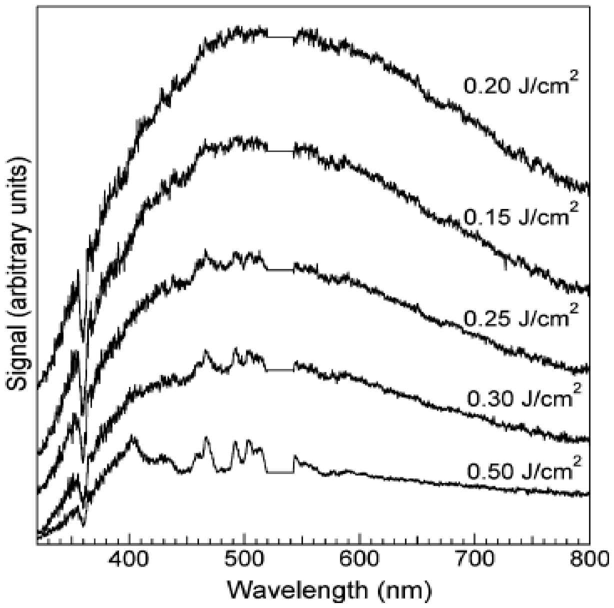

Figure 3.11 Comparison of spectral LII signals with 532 nm excitation at different laser fluences [40].

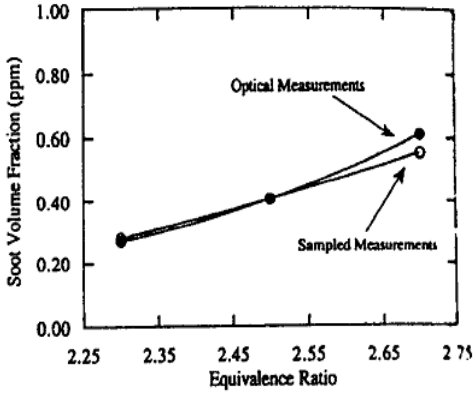

Figure 3.12 Comparison of Soot volume fraction measured by extinction technique and gravimetric measurement [43].

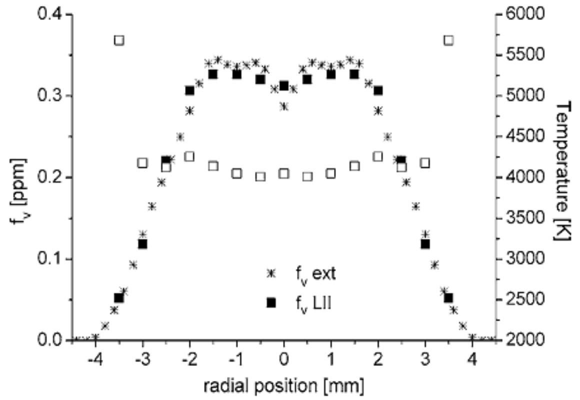

Figure 3.13 Soot volume fraction measured by LII and calibrated by extinction technique [44].

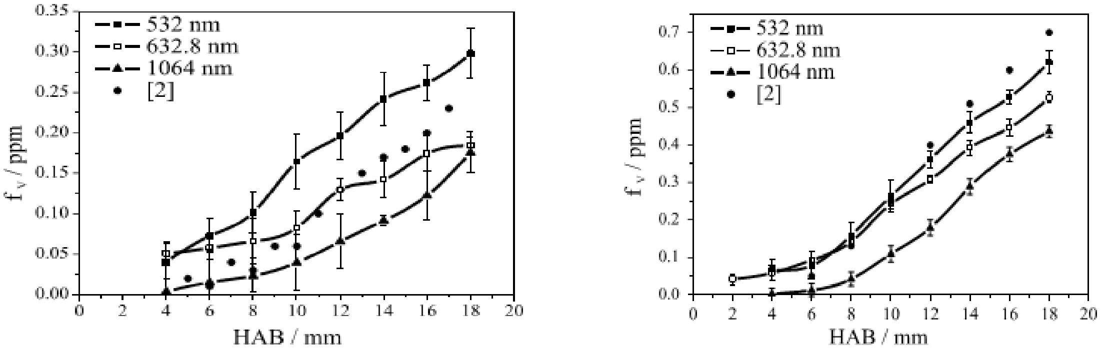

Figure 3.14 Comparison of soot volume fraction measurement by Extinction technique and Gravimetric technique [45] (Solid dots represent Gravimetric technique results).

Thus, the accuracy of planar soot volume fraction estimation depends upon the accuracy of calibration. Fig. 3.12 shows that the comparison of SVF estimated by extinction measurement with the gravimetric measurements. Recently, Cignoli et al. [44] reported a good agreement between f_v estimated by LII and calibrated by extinction technique for a standard ethylene flame as shown Fig. 3.13. They also found uniform primary soot particle temperatures in the measurement volume. However, one should be careful while applying calibration deduced from extinction measurements. Zerbs et al. [45] found that, for higher soot volume fractions, significant errors are introduced as shown in Fig. 3.14.

3.2 LII calibration burner

To utilize the LII technique for in-situ measurement of soot volume fractions in HFO spray flames, it is necessary to establish the LII experimental procedure, selection of operating parameters and extinction calibration methodology. For this purpose, a reference burner known as the Gulder burner is used [46]. A Gulder burner utilizes a laminar ethylene diffusion flame stabilized by a co-flow of air as shown in Fig. 3.15. Figures 3.16 & 3.17 show a schematic and images on the Gulder burner. The operating parameters of Gulder burner are listed in Table 3.1.

To characterize flow field of this burner and ensure that the co-flow is laminar, the PIV technique is used. Figure 3.18 shows the radial velocity profile of co-flow and the corresponding flow stream lines are shown in Fig. 3.19. These results indicate that the co-flow flow field is indeed laminar in nature.

This burner is then used to generate an ethylene-air laminar diffusion flame. A spatial distribution of soot volume fraction of Gulder burner flame is estimated using the LII planar technique and calibrated by extinction technique. An LII setup used for this investigation is shown in Fig. 3.6. The second harmonic of the Nd:YAG laser at 532-nm wavelength is used. Using sheet optics and a collimator, a collimated sheet of 50-mm height and 0.5-mm thickness is generated. The energy density of the laser sheet is maintained at 120 mJ/mm^2. A Lavision make 2-megapixel camera with an optical intensifier and a 400-nm bandpass filter is used to capture prompt LII images. A 100-ns exposure period is used for the Intensified CCD camera (ICCD) and 300 images are captured for each of the case mentioned in Table 3.1. The line-of-sight extinction technique is used for calibration of captured LII images.

Figure 3.15 Standard calibration burner for sooty flames.

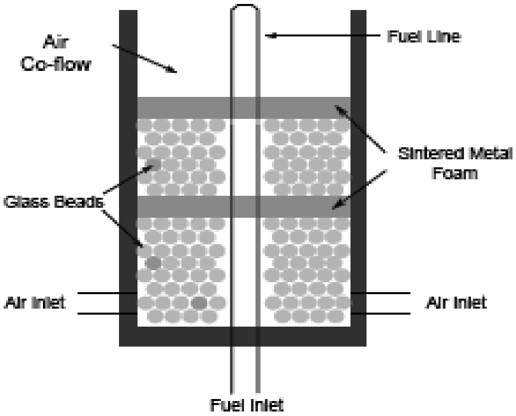

Figure 3.16 Schematic of Gulder burner construction.

Gas	Flow rate	Units
Ethylene	0.1938	std lit/min
Air	284	std lit/min

Table 3.1 Operating conditions for Gulder burner.

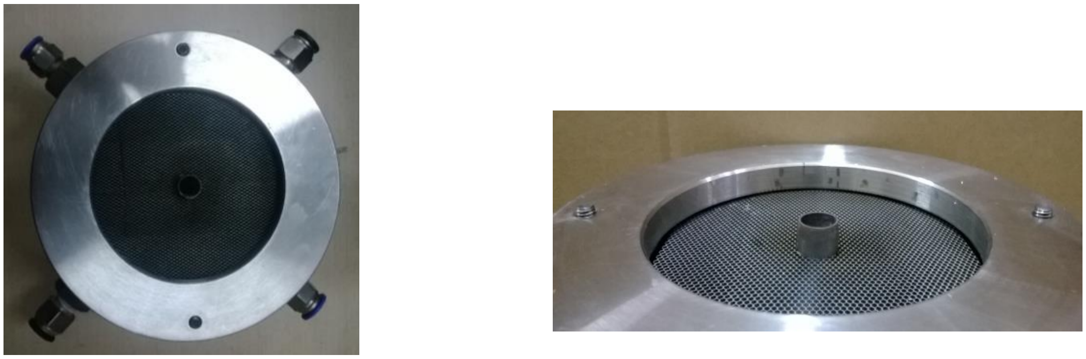

Figure 3.17 Images of the Gulder burner fabricated for the purpose of providing a calibration flame.

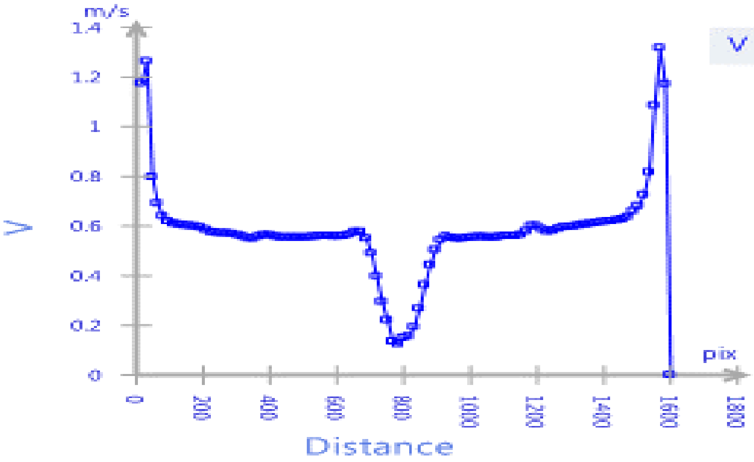

Figure 3.18 Radial velocity profile of co-flow for fabricated Gulder burner.

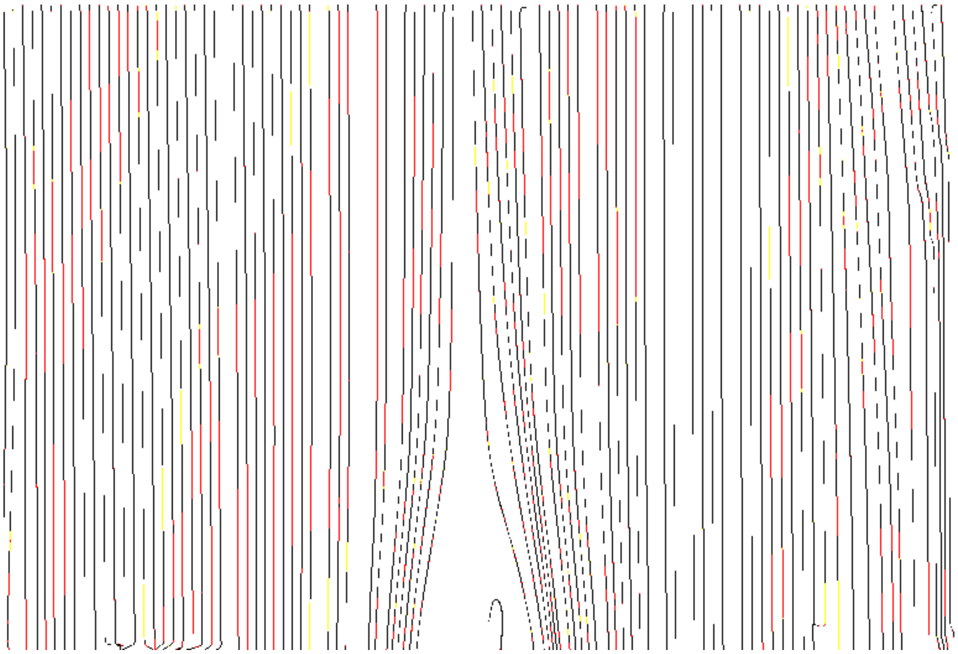

Figure 3.19 Streamlines of co-flow for fabricated Gulder burner.

A 532-nm continuous solid-state laser with a beam diameter of 3 mm is used for line-of-sight extinction measurements. The extinction measurements are recorded separately at the end of the LII imaging for every case. A Lavision Soot-master software is used for post-processing of LII images. Using equation (3.3), the calibration constant is estimated

A comparison between radial distributions of soot volume fraction at different heights (HAB) and the SVF data reported in [46] is shown in Fig. 3.21. The comparison of measured radial profiles with the reference data reported in literature shows that the measurements are within the experimental accuracy. Thus, the LII technique, extinction calibration procedure, and the selected operating parameters are validated. This technique is further used for soot emission investigation of HFO spray flames. It should be noted that for HFO flames, the primary soot particle size is expected to be very different as compared to that in the ethylene air flame from the Gulder burner. However, the extinction technique used for calibration is independent of primary particle size and is solely dependent on the line-of-sight extinction of the laser beam intensity.

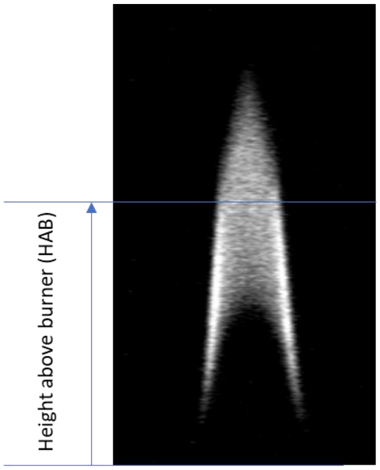

Figure 3.20 Single shot LII image of Gulder burner ethylene diffusion flame. The image intensity is calibrated at 42 mm HAB

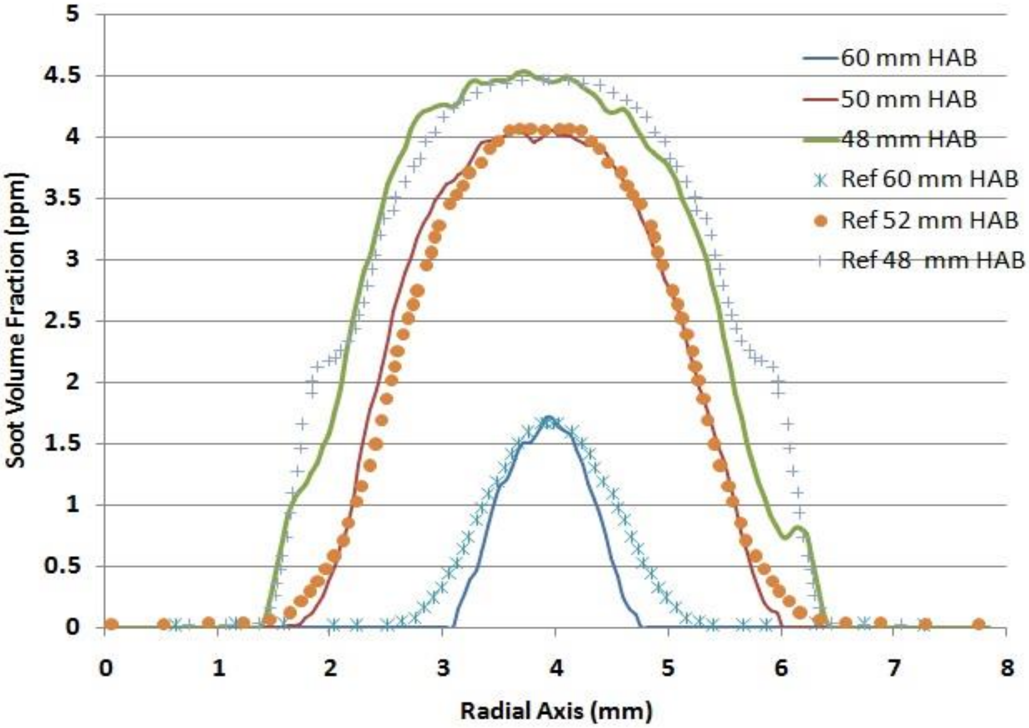

.

Figure 3.201 Comparison of SVF radial profiles at different heights and the corresponding [46].

3.3 Shadography (PDIA) technique

Particle/Droplet Imaging Analysis (PDIA), an image-based, non-intrusive droplet size measurement technique is used for droplet size measurements. In this method, backlit spray images are obtained in a magnified region of the spray and are analysed using computer-based post processing software. This technique has been extensively used for particle/droplet size measurements in recent times due to developments in computational algorithms and technological improvements in digital imaging equipment. PDIA uses short-duration lasers with a pulse width of the order of 10-ns and a diffuser for a uniform background. Due to the short duration of the illumination, the droplet images are practically frozen in time. Madan Mohan et al. [47] explain that PDIA measurements compare well with light-scattering based techniques such as Phase Doppler Anemometry (PDA). However, PDIA technique also provides additional information such as droplet shape and droplet velocities. PDIA is a planar imaging technique and hence measures droplets with various depth of focus (DOF). For larger droplets, DOF is higher while for smaller droplets DOF is smaller. This generates a bias towards larger droplets as larger droplets have higher probability to get captured during imaging than smaller droplets. Hence, a statistical DOF correction is applied to account for smaller droplets during imaging. A detailed method for DOF correction is explained by Kashdan et al. [47]

A typical PDIA setup is shown in Figure 3.23. It employs a 2-MP digital camera to capture images. A long-distance microscope (make: Questar model: QM100) is used to zoom in to a small area of 2-mm x 2-mm and image droplets present in the region. A pulsed Nd:YAG laser generating 532-nm harmonic is used as the light source. To create a high intensity luminous background, a fluorescent diffuser is used. A programmable timing unit (make: Lavision) is used to synchronize the light source and the camera and to enable imaging of the droplets with 10-ns exposure and at the rate of 15 Hz.

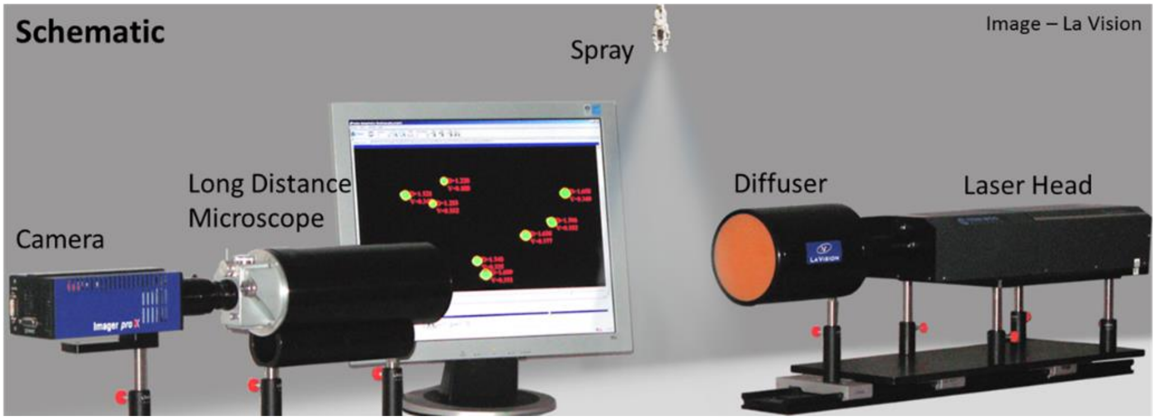

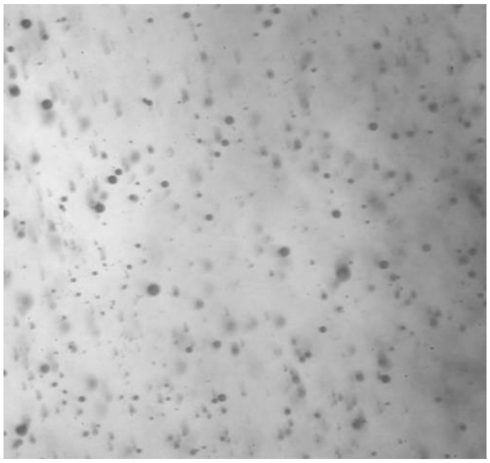

Figure 3.21 Raw image of droplets in spray.

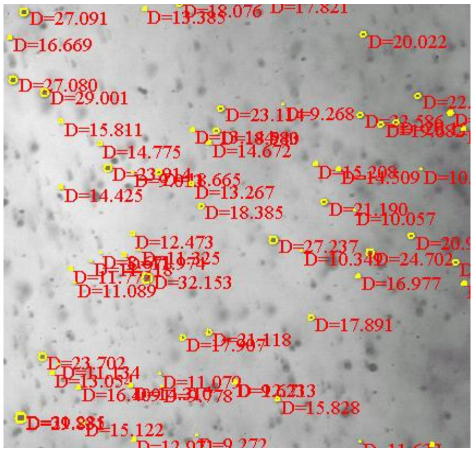

Figure 3.22 Post processed image of droplets and identified droplet diameters.

Figure 3.23 Typical experimental arrangement of PDIA technique.

A typical image of droplets in a spray environment is shown in Fig. 3.22. A droplet sizing software (Lavision ParticleMaster) is used to identify and estimate the size of the droplets in the depth of focus. A typical post processed image is shown in Fig. 3.23. By capturing multiple images of a spray, droplet size distribution and SMD characteristics can be determined.

3.4 Particle imaging velocimetry technique

Particle Image Velocimetry (PIV) is a non-intrusive technique which is used to estimate instantaneous velocity vectors in a fluid flow. In this technique, the fluid is seeded with fine particles which are assumed to follow the fluid flow dynamics. The motion of these seeding particles captured by a digital camera to estimate velocity field in the fluid. This is done by taking two images shortly after one another and calculating the distance traveled by the individual particles within this time. The displacement field is determined from the location of the seeding particles in the two images. The velocity field is obtained by dividing the displacement field by the known time separation.

A typical PIV setup consists of a CCD camera, high power laser, an optical arrangement to convert the laser output light to a light sheet, particle seeding equipment and controllers to synchronize flow imaging. A typical PIV setup is shown in Fig 3.25. Pulsed lasers such as Nd:YAG are used to generate near frozen images of the seeded particles in flow. The laser beam is converted in to a light sheet using cylindrical and spherical lenses to obtain planar, two-dimensional information. The tracer particles form the basis of the velocity measurement in PIV. The particles should be as small as possible so that they are able to closely follow the flow. However, on the other hand, they may not be too small, because then they will not scatter light sufficiently causing weak signals. In the present research, olive oil mist with an average particle size of 2-μm is used to seed the flow.

A double-pulse Nd:YAG laser (make: Lavision) generating 532-nm laser is used as light source. The two independent laser beams are carefully aligned to ensure that same plane is imaged during two consecutive laser pulses. A collimator (make: Lavision, Model: 1108405) is used to generate a laser sheet of height 40-mm and thickness 0.5-mm. A 2-megapixel CCD camera (make: Lavision) is used for imaging. Using a programable timing unit (make Lavision) dual pulse laser and camera shutter are synchronized. The Davis software (make: Lavision) is used to analyse and estimate flow velocity field.

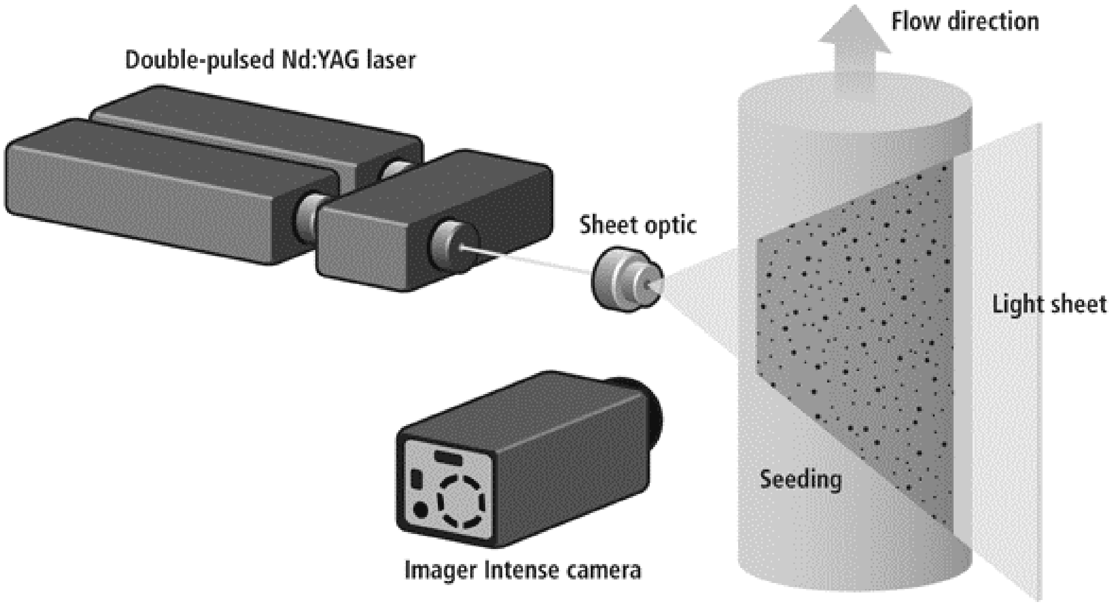

Figure 3.24 Typical setup used for PIV measurements.

3.5 Particle size spectroscopy

An aerodynamic particle sizer (make: TSI, model: 3321) shown in Fig 3.25 is used to quantitatively measure cenosphere emission density and particle size distribution. The aerodynamic particle sizer (APS) is based on time-of-flight spectrometry that measures the velocity of particles in an accelerating airflow through a nozzle. In the instrument, particles are confined to the centerline of an accelerating flow and then passed through two broadly focused laser beams. Side-scattered light from the particle in the flow is collected by an elliptical mirror that focuses the collected light onto a solid-state photodetector, which converts the light pulses to electrical pulses. By controlling the timing between the peaks of the pulses, the velocity can be calculated for each individual particle. The spectrometer then converts each time-of-flight measurement to an aerodynamic particle diameter. For convenience, this particle size is binned into 52 channels (on a logarithmic scale). The particle range spanned by the TSI APS spectrometer is from 0.5 to 20-µm. The schematic of the working of the APS is shown in Figure 3.26.

This equipment has an in-built suction pump to suck the flue gas sample into the instrument. It can measure particle density of up to 10000 particle/cm^3 with an accuracy of 10%. To avoid particulate separation in the probe, it is necessary that the suction probe is properly sized and has minimum bends. An L-shaped tube with 18-mm inner diameter and 100-mm radius of curvature is used as a probe for a sampling of flue gases. It should be noted that this instrument can handle particle-laden flows only at room temperature. Hence, it is imperative to cool the exhaust gas before it enters the aerodynamic particle sizer.

Figure 3.25 Aerodynamic particle sizer, TSI Model 3321.

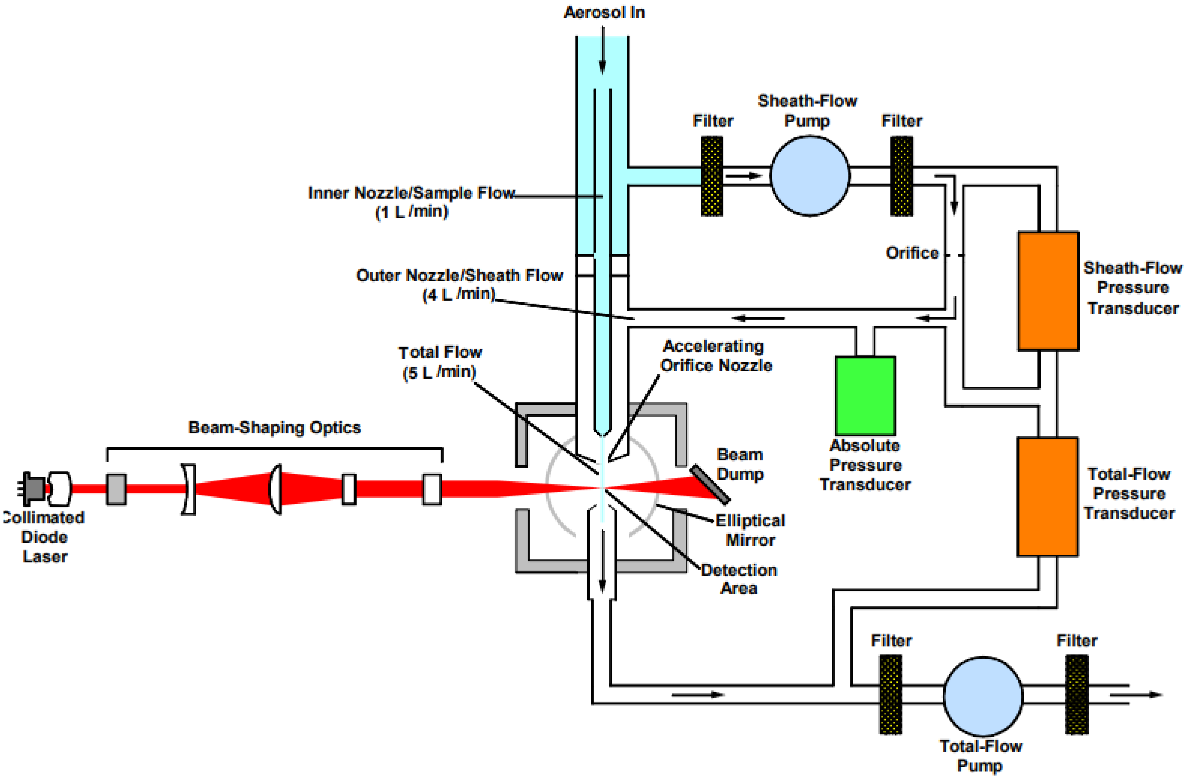

Figure 3.26 Schematic of TSI APS.

4 Experimental setup

To study HFO droplet combustion in a practical environment, there is a need to develop research burner that can accurately reproduce droplet combustion dynamics in a combusting spray environment. In such an environment, the droplet experiences a complex interplay of the boundary layer, transient heating, convective evaporation, and combustion. Most liquid spray combustion burners involve dense sprays where it is possible to investigate the effect of spray characteristics on global performance parameters such as flame height and soot emissions. However, the liquid fuel spray flame burner proposed by Lemaire et al. [48] is found suitable to investigate the effect of spray characteristics such as drop size distribution on the particulate formation as it typically involves very sparse sprays. Some minor modifications are carried out to this design in the present thesis make it suitable to study HFO spray flames. The description and characterization of this burner are presented in the next few sections.

4.1 HFO spray research burner

The research burner setup constitutes a modified McKenna flat flame burner with a central tube and is operated at atmospheric conditions. A twin-fluid nebulizer (make: Meinhard model: DIHEN-170-A0.1) is placed in the central tube and is flush with the flat burner surface, as shown in Figure 4.1 and the schematic of the research burner is shown in Figure 4.2.

4.1.1 Flat flame burner

The Mckenna burner is standard calibration burner used in combustion studies on flat flames. The burner has a water-cooled sintered top through which premixed air-fuel mixture is supplied. A modified Mckenna burner has a 6-mm central tube as shown in Figure 4.1. The Mckenna burner generates a flat flame which is used to generate a hot co-flow into which the HFO spray from the nebulizers is injected at the center. The hot co-flow is generated using an H_2-O_2-N_2 as a fuel-oxidizer mixture and is burnt in the form of a laminar flat flame. Hydrogen is used as a fuel to generate the hot gas as it does not contribute to any of the carbon emissions. This aspect is useful in the study of soot formation from HFO spray flames. By varying the hydrogen flow, the co-flow temperatures can be varied. By varying the oxygen flow rate, a hot inert or oxidizing co-flow atmosphere can be generated. In the present experiments, the hot co-flow temperature is varied from 823 K to 1373 K and the oxygen mole fraction is maintained at 20% to mimic the realistic combustion of HFO in industrial burners.

4.1.2 Nebuliser system

In order to generate a statistical methodology for droplet combustion studies, it is desirable to use an atomizer which can generate very dilute sprays with a variable mean droplet diameter. Hence, a quartz nebulizer (make: Meinherd, model:Q-DIHEN-170-A0.1) is used which can generate a finely atomized and sparse fuel spray [49] [50]. It is a twin-fluid nebulizer, which uses nitrogen as the atomizing gas. The HFO is introduced into the nebulizer capillary using a stainless-steel syringe and a syringe pump. As discussed, the HFO exhibits high viscosity at room temperature and hence it is preheated to 80°C using a tape heater wound on stainless steel syringe. As the nebulizer contains very fine capillary (diameter: 100-µm), to maintain HFO preheat till the tip of the nebulizer, atomizing gas is also preheated to 90 °C using a pipe heater. The nebulizer thus produces a sparse HFO spray along the central line of the flat flame burner. By varying the gas-to-liquid ratio (GLR), different droplet size distributions are achieved.

4.2 Spray evaporation studies

In order to validate the newly-devised research burner and to gain insights on the convective evaporation of droplets, single-component liquid spray evaporation studies are first carried out in a non-oxidizing hot environment. The single component liquids such as n-decane and n-dodecane are studied and their evaporating constants K_{evap} are estimated in the convective spray environment. As mentioned earlier, premixed hydrogen-nitrogen-oxygen flame is used to generate a controlled hot co-flow environment surrounding the central spray. The conditions are chosen such that the temperature of the inert co-flow is maintained at 600°C. Table 4.1 lists the operating conditions used for these evaporation studies. As discussed earlier, the atomizing gas jet dissipates its momentum along the central axis. Thus, the droplets experience varying drag conditions due to change in the surrounding flow field. Thus, in order to experimentally deduce the evaporation rates of liquid droplets, it is required to measure droplet distributions at different heights along the central axis, the droplet velocities and the decaying central atomizing jet velocity field along the axis.

4.2.1 Atomizing jet velocity field measurement:

A non-intrusive planar Particle Imaging Velocimetry (PIV) technique is used to estimate the velocity decay velocity profile of the central atomizing jet. A PIV setup uses a dual-pulse Nd:YAG laser operating at 532-nm wavelength and 15-Hz repetition rate as an illuminating light source in the form of a 1-mm thick laser sheet. A 2-Megapixel CCD camera along with 532-nm bandpass filter is used to capture Mie scattering from the droplets. A Lavision PIV software is used to post-process the images to estimate the centerline atomizing jet velocity field.

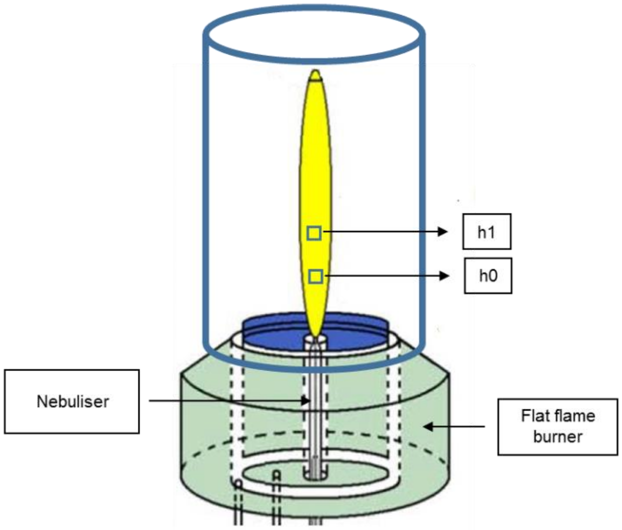

Figure 4.1 Schematic of a flat flame research burner with centrally placed nebuliser.

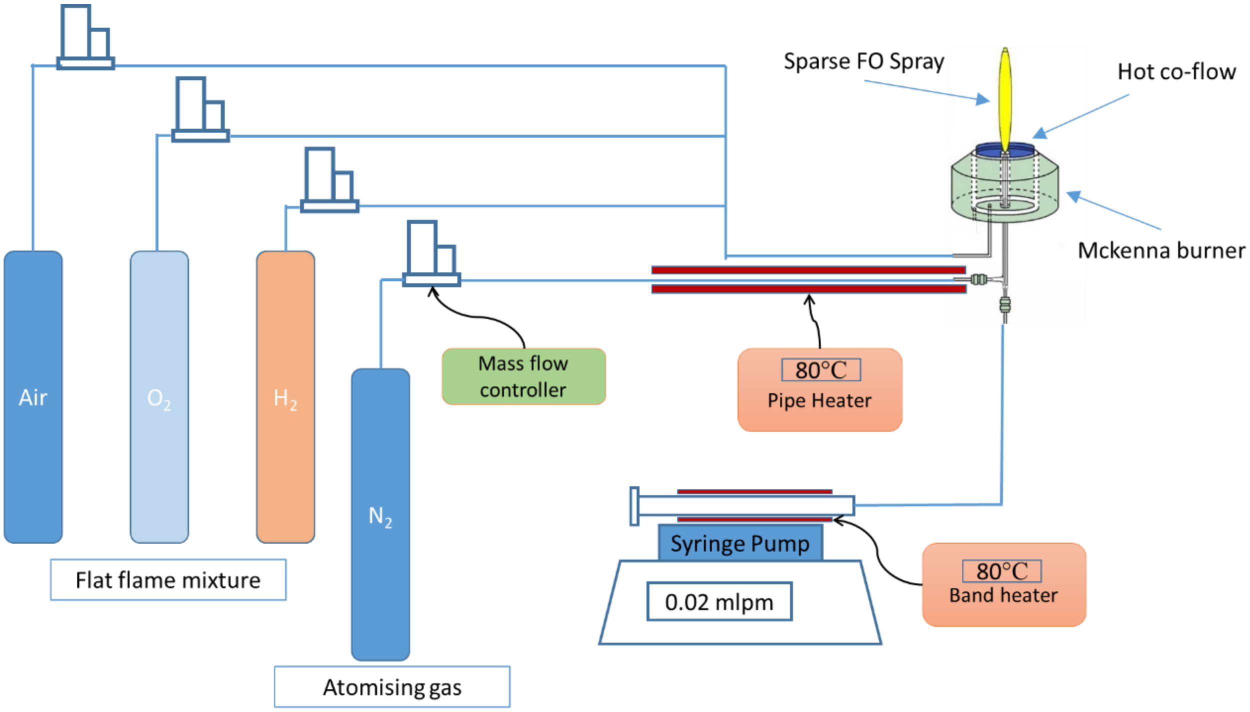

Figure 4.2 Schematic of the experimental setup used for study of HFO droplet combustion.

Parameter	n-decane	n-dodecane
Liquid flow (mlpm)	0.05	0.05
Atomizing N_2 gas flow (SLPM)	0.1	0.15
H_2-N_2-O_2 flow rate (SLPM)	1.7 - 1.7 - 12	1.7 – 1.7 - 12
Co-flow temperature (°C)	600	600

Table 4.1 Operating parameters of research burner for evaporation studies.

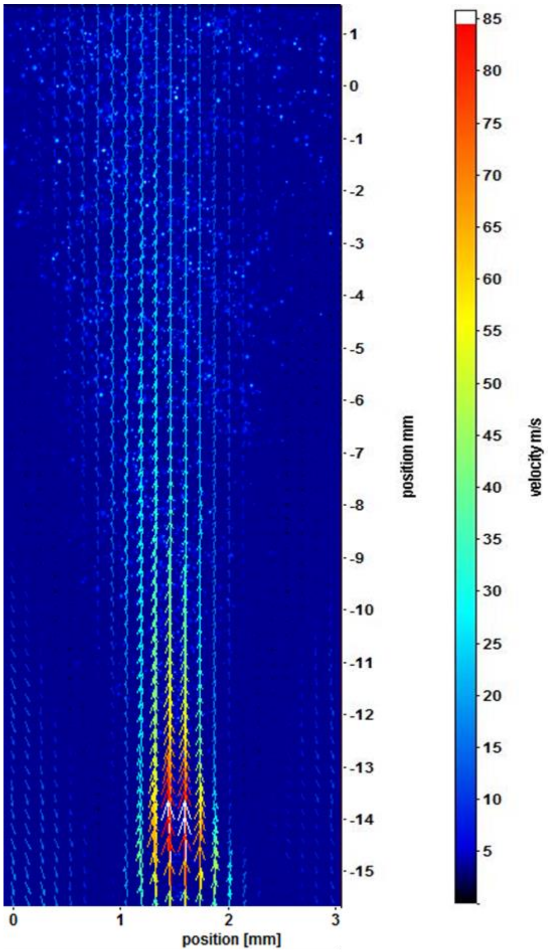

Figure 4.3 Velocity field of the central atomizing gas jet.

Figure 4.3 shows the atomizing jet mean velocity vector field superposed on the liquid spray Mie scattering image. It can be observed that droplets in liquid spray experience the convective velocity field due to atomizing jet. The centerline jet velocity is extracted from this velocity vector field as shown in Figure 4.5. Phenomenologically, an atomizing jet decay is similar to a turbulent gas jet dissipating in a quiescent environment as shown in Figure 4.4. Typically, the mean velocity of turbulent jet dissipates as:

$$V(x) = 5\ V(0) \left(\frac{x_0}{x}\right) \tag{4.1}$$

where x_0 is jet entrance height, x is height along the axis, and V(0) is centerline jet velocity at x_0.

The comparison of the measured mean of axial velocity decay as compared to a theoretical decay profile is shown in Figure 4.5. There is a good match between the empirical and the experimental mean velocity decay profile. The error bar indicates the extent of mean velocity fluctuations. It should be noted that the atomizing jet is laden with liquid droplets. However, as the spray is dilute in nature, the effect of presence of droplets on the decay profile is not pronounced.

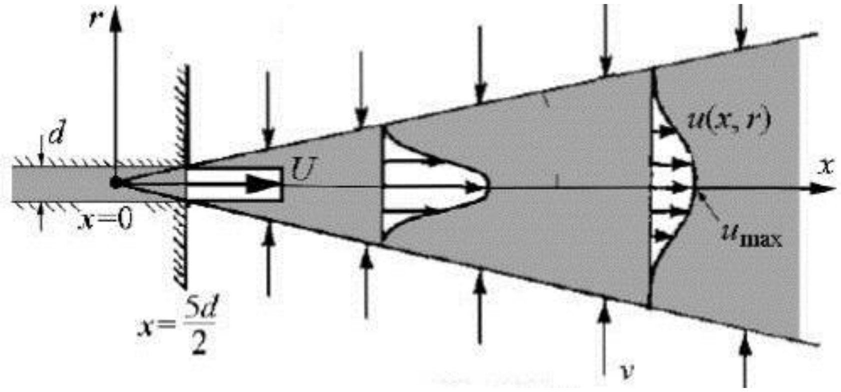

Figure 4.4 Velocity field of the turbulent gas jet dissipating in a quiescent environment [51].

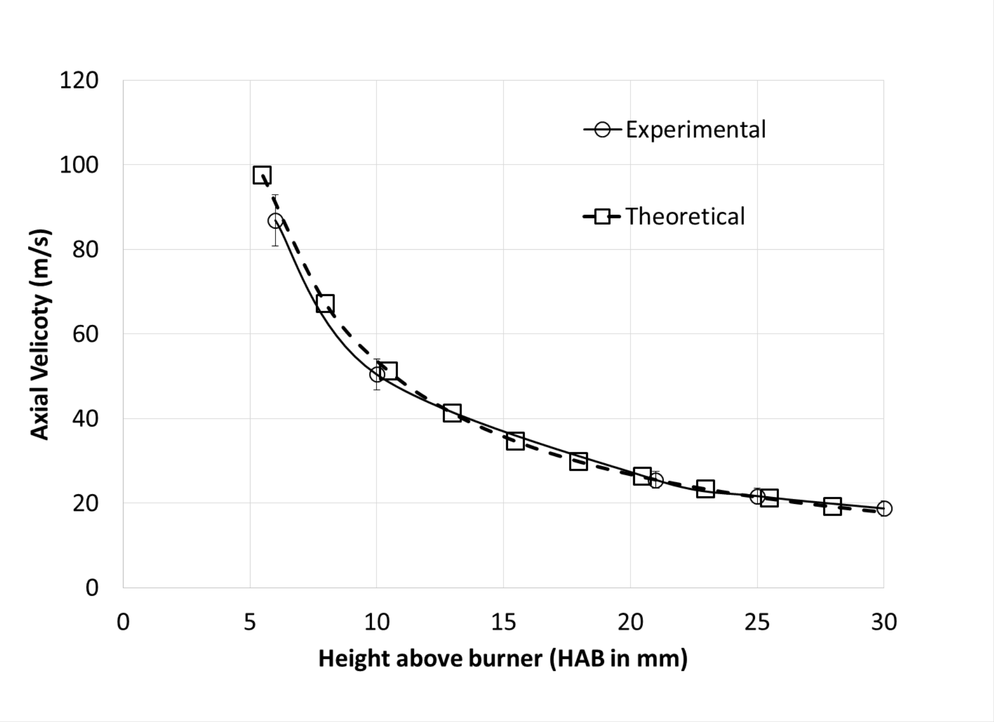

Figure 4.5 Decay in the centerline mean velocity of the atomizing jet.

4.2.2 Droplet size and droplet velocity measurement:

The spray drop-sizing and the velocity measurements are conducted at different heights (HAB) in an evaporating spray to statistically estimate droplet evaporation rate for liquids such as n-decane and n-dodecane. Based on lumped transient heating analysis of a droplet, it is found that a 40-μm droplet reaches boiling point at a height of 4-mm and 8-mm above the burner for n-decane and n-dodecane, respectively. Hence, for the current study, the droplet diameters and velocities are recorded at heights excess (height above burner) of 5-mm and 10-mm for n-decane and n-dodecane, respectively.

The droplet sizes and their velocities are measured using the Shadowgraphy technique. The technique is a based on high resolution imaging with a pulsed backlight illumination. A uniform backlight background is produced by laser-induced fluorescence. The droplet images are recorded using a 2-megapixel CCD camera fitted with a Long-Distance Microscope (LDM). The LDM gives a field of view of 1.5-mm by 2-mm. Hence, very small droplets of diameter ~ 5-μm can be directly imaged. Using an image processing software (Make: Lavision ParticleMaster), the particle sizes and their velocities are estimated. The droplet imaging is carried out at two different heights along the burner axis. For the evaporation rate analysis, only droplets which have a predominantly axial velocity (with 99% or more axial velocity component) are filtered for further analysis. This filtration strategy is used to ensure that the droplets considered for evaporation rate analysis are travelling along the burner axis.

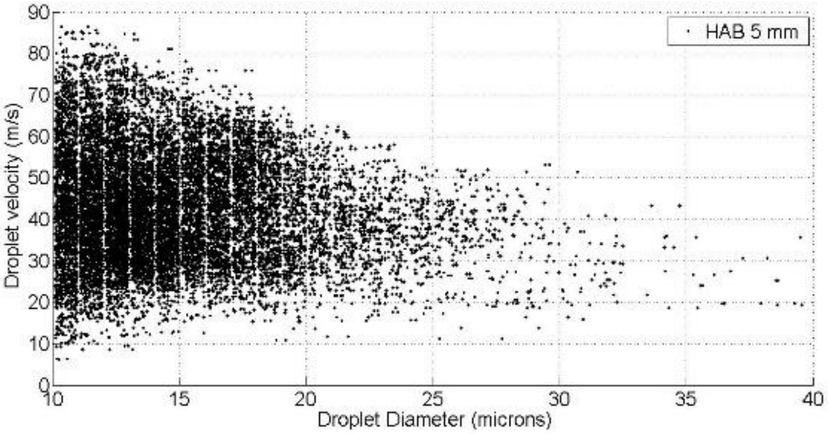

Figure 4.6 Droplet diameter-velocity correlation for n-decane at HAB=5-mm.

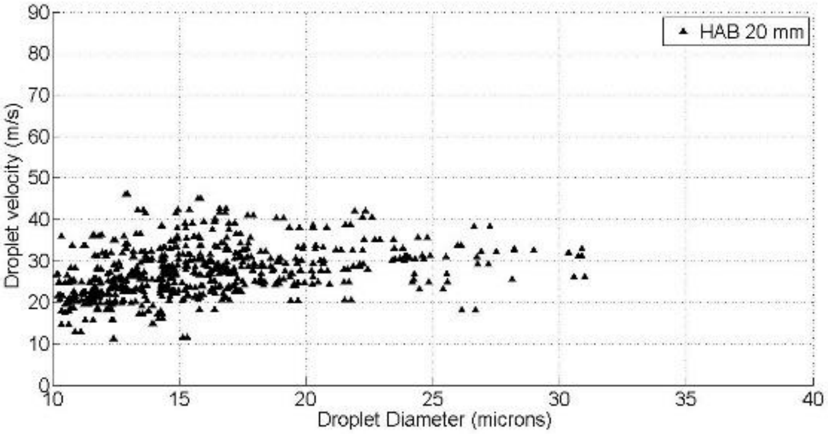

Figure 4.7 Droplet diameter-velocity correlation for n-decane at HAB=20-mm.

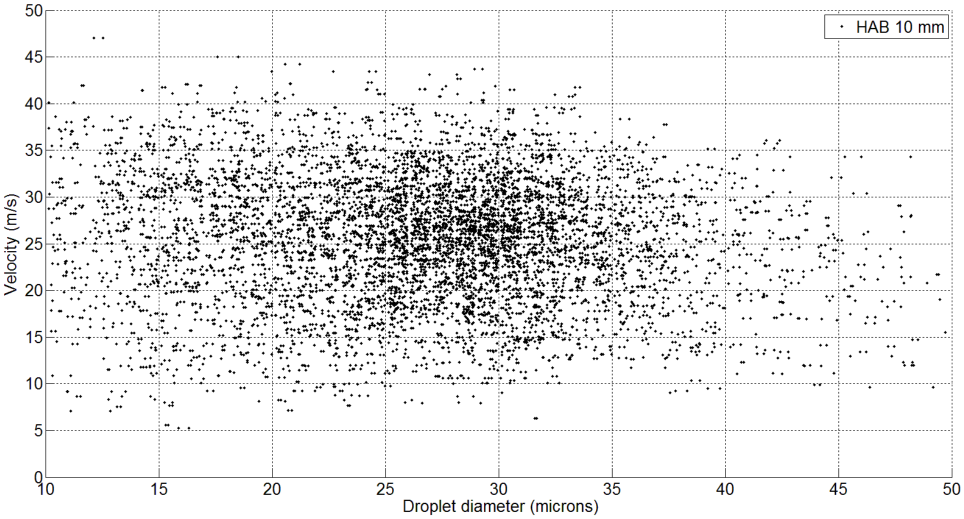

Figure 4.8 Droplet diameter-velocity correlation for n-dodecane at HAB=10-mm.

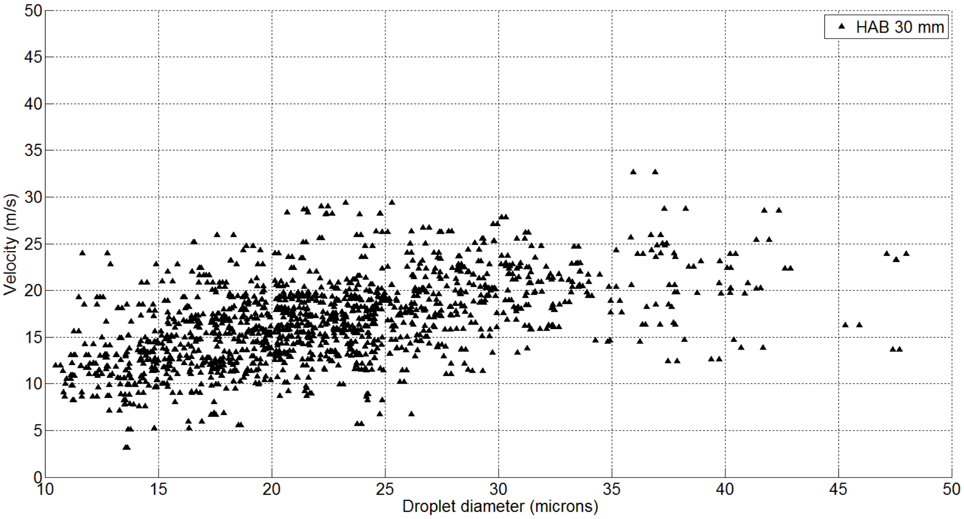

Figure 4.9 Droplet diameter-velocity correlation for n-dodecane at HAB=30-mm.

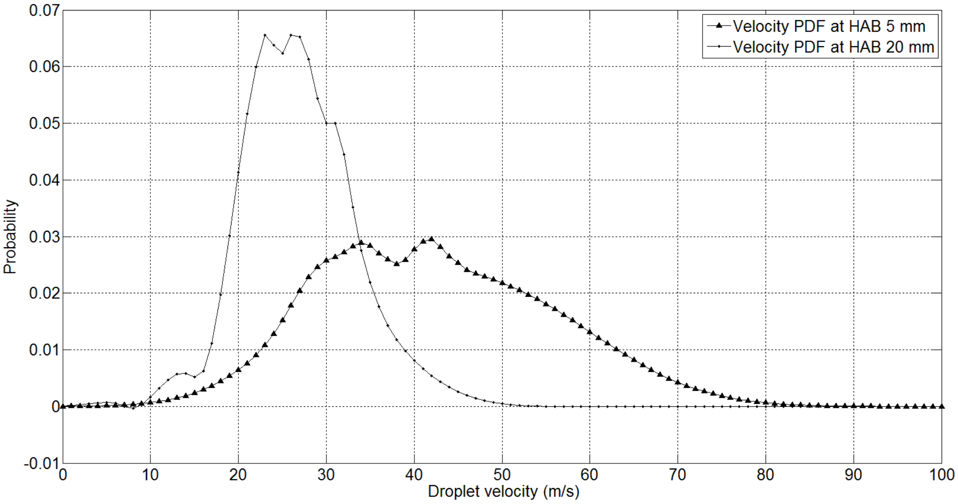

Figure 4.10 Droplet Velocity PDF for n-decane.

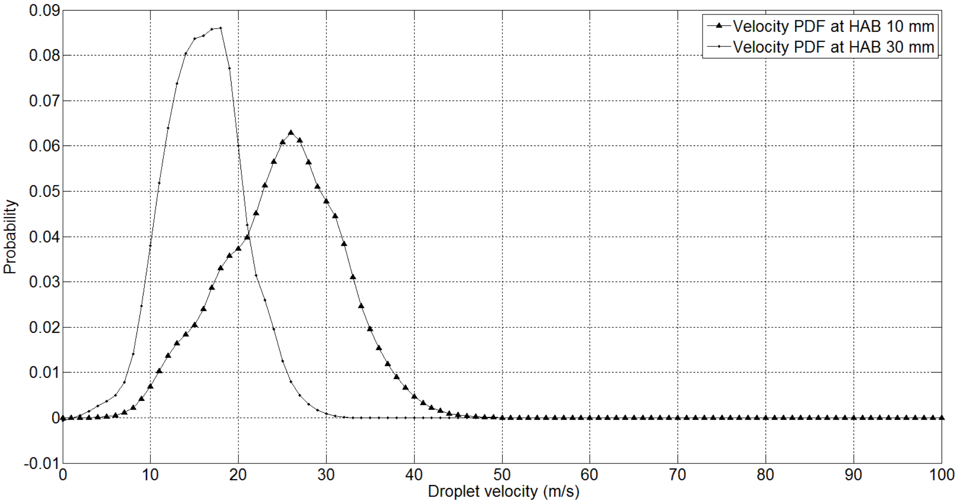

Figure 4.11 Droplet Velocity PDF for n-dodecane.

Figure 4.6 and Figure 4.7 show the droplet diameter–velocity correlations for n-decane at HAB of 5-mm and 20-mm, respectively. Figure 4.8 and Figure 4.9 show the droplet diameter-velocity correlations for n-dodecane at HAB of 20-mm and 30-mm, respectively. It is observed that the droplet velocity variance as well as the mean velocity decreases with height above burner. This can be attributed to the decaying co-flow velocity field and the droplet evaporation, as discussed previously. The comparison of PDF of mean axial velocities for droplets as shown in Figure 4.10 andFigure 4.11 also corroborates this fact. Furthermore, at higher heights, it is observed that larger diameter droplets (~ 30-µm) have higher velocities than smaller diameter droplets (~ 10-µm). The larger droplets due to higher initial momentum retain their momentum for a longer time, while the smaller droplets lose their momentum rapidly. This explains the trends observed in Figure 4.7 and Figure 4.9. As the droplets have a range of initial diameters and velocities, they experience different convective conditions and hence, different evaporation rates. This may be due to jet breakup dynamics and turbulence in the jet carrying the droplets. This experimental data is further utilized to evaluate droplet evaporation timescales and estimate the evaporation rate constant. For droplet evaporation rate estimation, classical models are used for momentum transfer (Cd), convective heat transfer (Nu) and mass transfer (Sh) [52]. The simplified droplet evaporation model assumes that liquid has infinite conductivity and droplets are at boiling temperature. The correlations from these models used are listed below.

$$\frac{dm}{dt} = Sh\pi D\rho_c D_v\,(\omega_s - \omega_\infty) \tag{4.2}$$

$$\frac{dU}{dt} = \frac{3\,C_d}{2\,r}\left(\frac{\rho_\infty}{\rho_l}\right)\,|U_\infty - U|\,(U_\infty - U) \tag{4.3}$$

$$Nu_0 = 1 + (1 + RePr)^{1/3}\ Re^{0.077}$$

(4.4)

$$Nu = \frac{\log(1 + B_t) * Nu_0}{B_t}$$

(4.5)

$$Sh_0 = 1 + (1 + RePr)^{1/3}\ Re^{0.077}$$

(4.6)

$$Sh = \frac{\log(1 + B_t) * Sh_0}{B_t}$$

(4.7)

$$C_d = \frac{12.69}{Re^{2/3}\ (1 + B_t)}$$

(4.8)

where,

m = droplet mass,

U = droplet velocity,

Nu_0 = Nusselt number without convection,

B_t = Spalding heat transfer number,

Pr = Prandlt number,

Sh = Sherwood number.

C_d = coefficient of drag

Where, the droplet diameters and their velocities at the lower heights (HAB) are used as initial conditions for the numerical modeling using the above-mentioned correlations. Using the numerical model, the droplet diameters and velocities are predicted at higher heights, i.e., at HAB of 20-mm for n-decane and HAB of 30-mm for n-dodecane. These are then compared with experimental data. Figure 4.12 and Figure 4.13 show the comparison of predictions with experimental data. It is clearly observed that the standard correlations predict droplet evaporation i.e., convective mass transfer and momentum transfer with considerable accuracy.

It is also observed that the predicted values show a clear correlation as opposed to considerable scatter observed in the experimental data. The scatter in the experimental data can be attributed to the initial breakup dynamics of the air-assisted atomization in the nebulizer, and also to the turbulence in the atomizing jet. As the model uses mean velocity, it fails to capture the velocity fluctuations. The above findings indicate that classical formulation can be utilized to reasonably estimate evaporation rates for pure component droplets under evaporative convective conditions. The effect of turbulence enhanced heat, mass and momentum transfer mechanisms are not modeled in this formulation.

4.2.3 Evaporation rate estimation for multi-component fuels:

In the case of real fuels such as Jet-A1 which are multicomponent liquids, it is difficult to know the exact composition of the fuel and consequently their thermo-physical and chemical properties. Hence the classical approach explained above cannot be used for estimating K_{evap} value. As shown in Figure 4.14, for HAB > 30 mm, the centerline co-flow velocity is ~ 5 m/s. The velocity decay is slow between HAB=30 mm to HAB=60 mm, which can be considered practically constant. From Figs 5.10 and 5.11, we observe that at higher heights (HAB > 30 mm), the droplets nearly attain local velocities (Stokes regime) and evaporate in a quiescent environment.

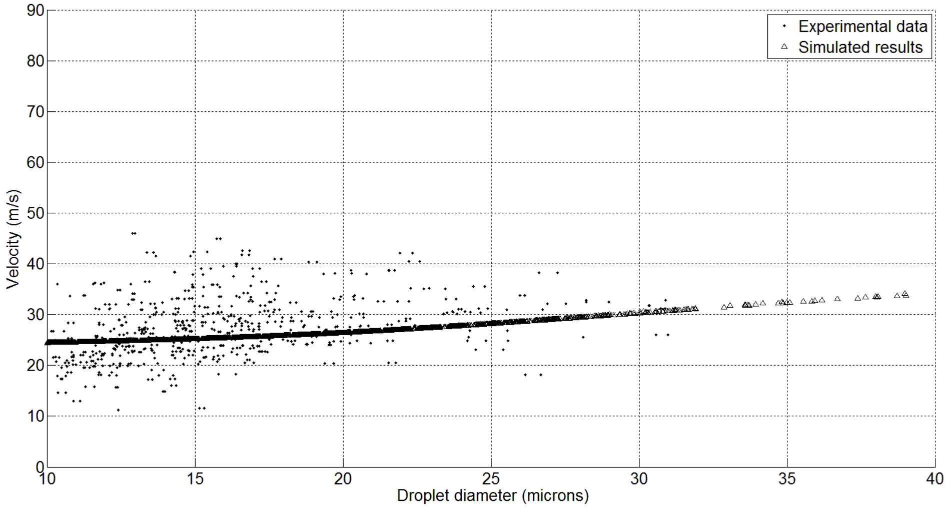

Figure 4.12 Comparison of experimental and predicted correlation for n-decane at HAB=20 mm.

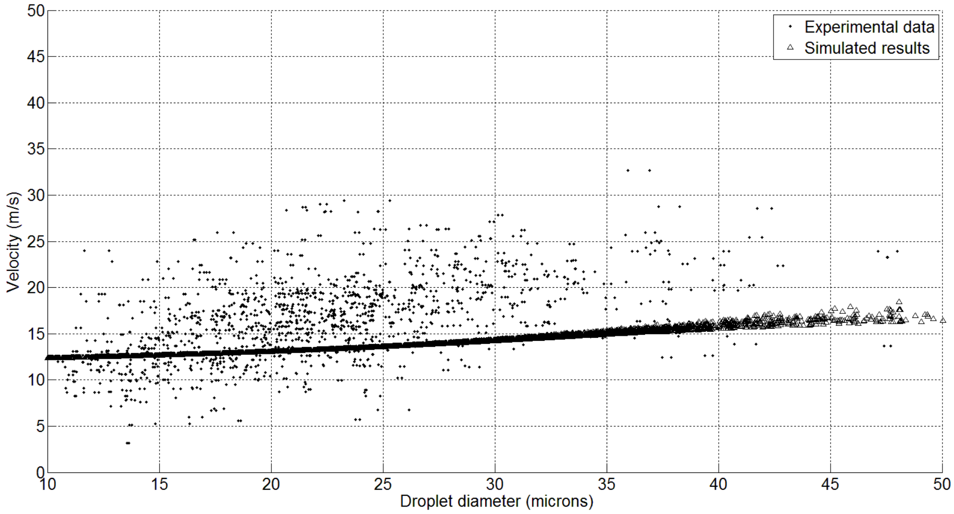

Figure 4.13 Comparison of experimental and predicted correlation for n-dodecane at HAB=30 mm.

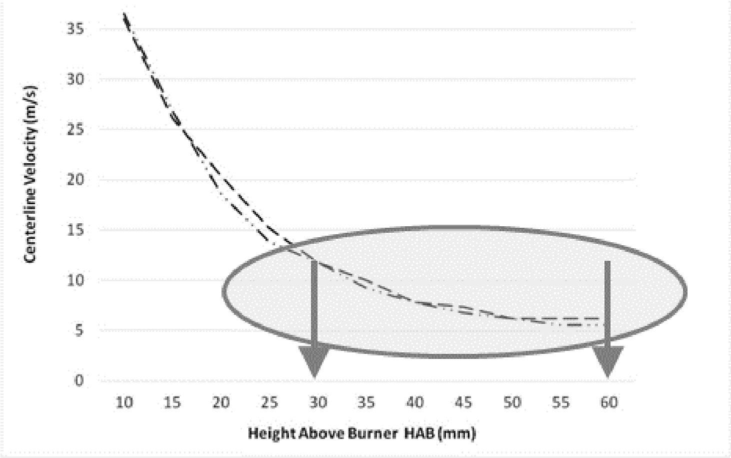

Figure 4.14 Decay in the centerline mean velocity of the atomizing jet.

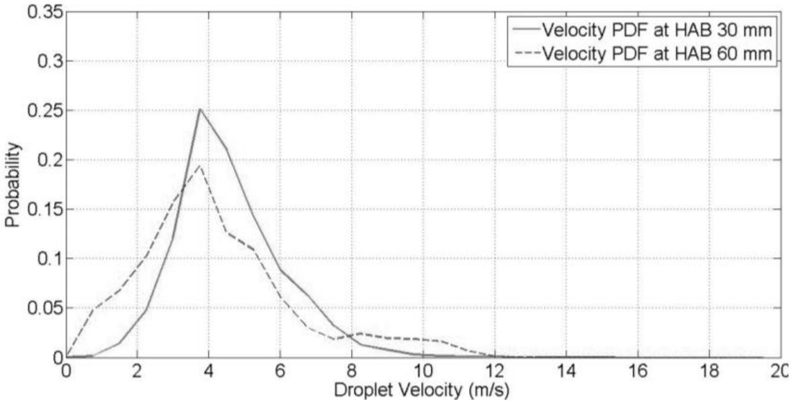

Figure 4.15 Droplet Velocity PDF for Jet-A1 fuel at HAB= 30mm and HAB= 60mm.

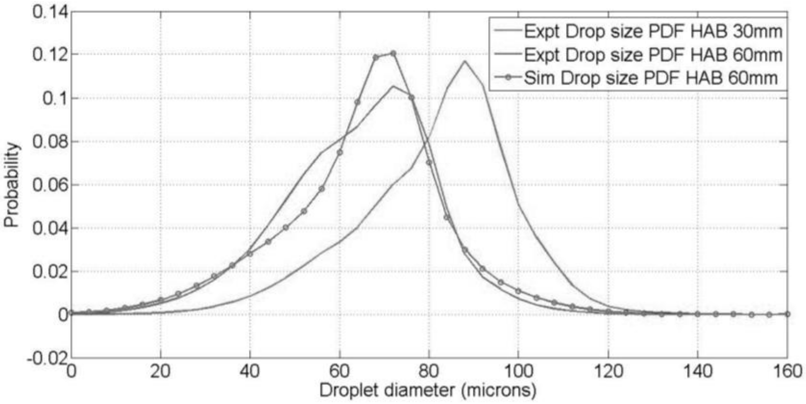

Figure 4.16 Comparison of Drop size distribution for Jet-A1 spray at HAB= 30mm and HAB= 60mm.

The droplets at these heights undergo evaporation under quasi-steady velocity conditions with nearly zero relative velocity (quiescent environment). Figure 4.15 shows the measured velocity PDF for Jet-A1 fuel droplets at 30-mm and 6-mm HAB and validates this argument. Hence, droplets size and velocities for all are measured at HAB = 30 mm and HAB = 60 mm. The classical D^2-*law* is used to predict the drop size PDF at HAB=60 mm. For Jet-A1 spray, with K_{evap} = 0.35 mm^2/s, the comparison of experimentally measured droplet size distribution with the predicted droplet size distribution is shown in Figure 4.16.

$$D^2 = D_0^2 - K_{evap} t \tag{4.9}$$

where, D_0 = initial droplet diameter and D = droplet diameter after time t.

The evaporation constant estimated for Jet-A1 fuel matches well with the experimental values reported by Horender et al. [54] and Strotos et al. [55].

4.2.4 Parametric study of convective droplet evaporation

The classical numerical model is further utilized to gather further insights on droplet evaporation under convective conditions, where the surrounding environment is maintained at temperatures well above the boiling point of the liquid. Using the validated classical numerical model, the following parametric studies are conducted.

4.2.4.1 Effect of droplet initial conditions on droplet downstream velocity

The experimental investigation of droplet evaporation indicates that convective heat and mass transfer play a predominant role in droplet evaporation in a spray environment. Hence, it is imperative to study the effect of droplet initial diameter and initial velocity of injection on the relative convective velocity of the droplet in the evaporative environment. In this parametric study, initial droplet diameters of 20-μm and 80-μm are studied with initial velocities of 20 m/s and 80 m/s in each case. Figure 4.17 shows the results of this parametric study. The green line indicates dissipating central atomizing jet of the nebulizer. With smaller initial droplet diameter of 20-µm, the droplet velocity accelerates initially and then decreases rapidly to follow central jet velocity. For both cases of 20 m/s and 80 m/s initial velocities for the 20-µm droplet, the relative convective velocities are reduced to zero at about 40-mm HAB. Above this height, the droplet experiences the quiescent evaporating environment, i.e., zero relative velocity. In case of the larger initial droplet diameter of 80-µm, the droplet velocities expectedly decay at a slower rate. With a higher initial velocity of 80-m/s, the droplet velocity is considerably higher than centerline velocity even at 150-mm HAB. For the lower initial velocity of 20-m/s, the droplet velocity approaches the decaying centerline velocity at about 120-mm HAB. The relative convective velocity is considerably lower along centerline as compared to the 80-m/s velocity case. Thus, it can be observed that larger droplets lose their momentum at a lower rate as compared to smaller droplets and hence experience convective evaporation for a longer period.

4.2.4.2 Effect of initial droplet diameter on rate of evaporation

To study the effect of droplet relative velocity and size on instantaneous evaporation rate, the non-dimensional droplet diameter is shown against a normalized time scale for droplet evaporation. Figure 4.18 shows the temporal evolution of droplet diameter for two different initial diameters of 20-µm and 80-µm. The slope of the curve represents the droplet evaporation rate constant K_{evap}. The non-dimensional droplet diameter evolution shows that under convective evaporative condition, the droplet evaporation rate is higher initially due to higher relative velocities. The evaporation rate reduces quickly and then asymptotically reaches the droplet evaporation rate in a quiescent environment. In line with the parametric study of droplet velocity evolution, the larger droplet evaporates at higher evaporation rate K_{evap} =0.82 mm^2/s as compared to the smaller droplet (K_{evap} =0.4 mm^2/s). This is mainly due to higher relative convection velocities experienced by the larger droplet than the smaller droplet for the same initial velocity. At higher heights (HAB), for the smaller droplet, the relative convective velocity is nearly zero, i.e., the droplet evaporates in a quiescent hot environment and hence, the curve is a straight line with a constant slope of 0.11 mm^2/s. However, for the larger initial diameter, the droplet experiences relative convective velocity till a height of 150-mm and hence, the droplet experiences higher evaporation rates at higher heights. This shows that larger droplet evaporates faster than the smaller droplet in convective spray environment.

Thus, spray evaporation studies are successfully carried out on the newly designed research burner. An experimental technique and numerical scheme have been established to estimate droplet evaporation rates in convective spray environments as well as quiescent environments.

The evaporation studies presented in this chapter validate the following key features of the research burner:

- The nebuliser system generates a finely-atomised dilute spray which enables a controlled study of droplet dynamics.
- The decaying velocity field experienced by the droplets is also characterized and the co-flow facilitates control of the thermal environment experienced by the droplets.

This research burner is next used to study effect of droplet size on HFO combustion. The results of the HFO spray combustion and particulate emissions are described in the next few chapters.

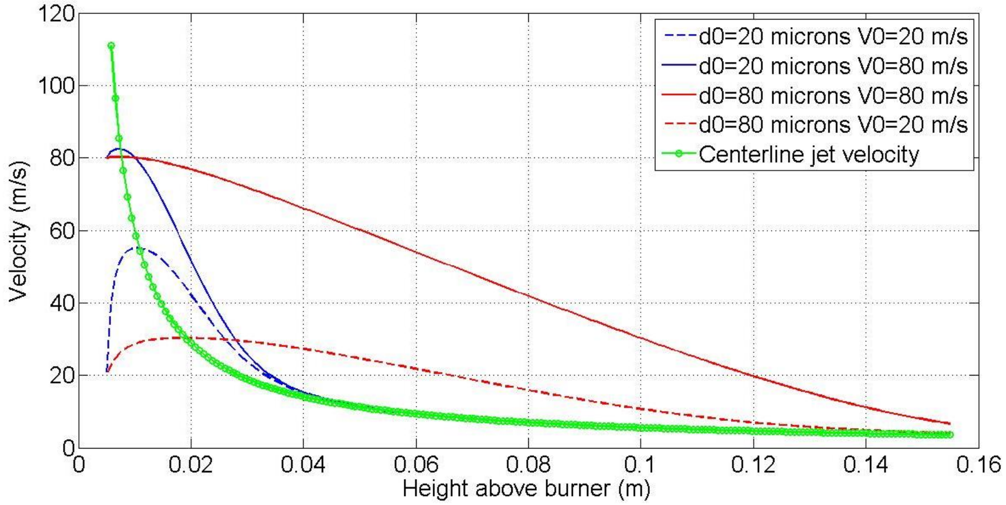

Figure 4.17 Effect of droplet initial droplet size and velocity of downstream velocity evolution.

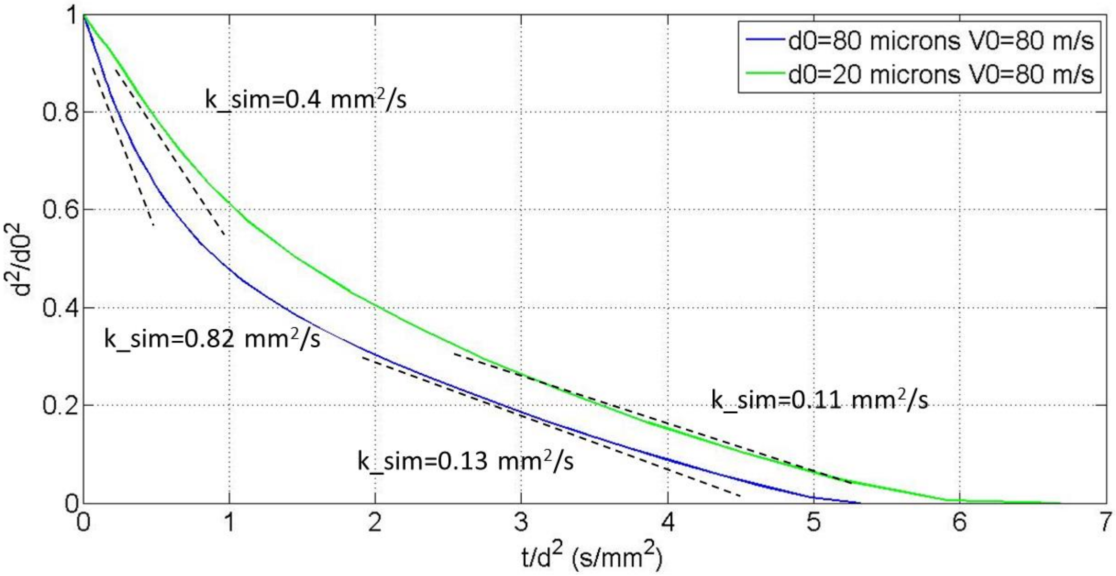

Figure 4.18 Effect of droplet initial conditions on temporal evaporation rate.

5 Heavy Fuel Oil (HFO) spray characterization

To investigate the effect of drop size on HFO combustion and particulate formation, it is necessary to quantify the spray drop size distribution generated by the nebulizer system. Typically, drop size distributions are measured in cold spray environment and it is assumed that the distribution does not get affected by the hot co-flow. As discussed in section 3.2, PDIA, a spray characterisation technique is used to image HFO droplets in spray environment and determine their sizes for different conditions. Using this technique, the drop size distributions and Sauter mean diameters (SMD) are determined for the complete range of operating gas to liquid ratios (GLR) for nebulizer system. **Error! Reference source not found.** shows the operating GLRs of the nebulizer and the measured drop size distributions for HFO sprays in cold atmosphere. However, during initial HFO spray combustion experiments, it was found that the spray characteristics of HFO are quite different in non-combusting and combusting environments. A considerable change in droplet dispersion is observed from Mie scattering images of HFO spray in cold co-flow and combusting spray environments (refer **Error! Reference source not found.**). This indicates a substantial change in spray characteristics in the combustion environment as compared to that in the cold environment. Hence, it is imperative to image droplets in the spray combustion environment.

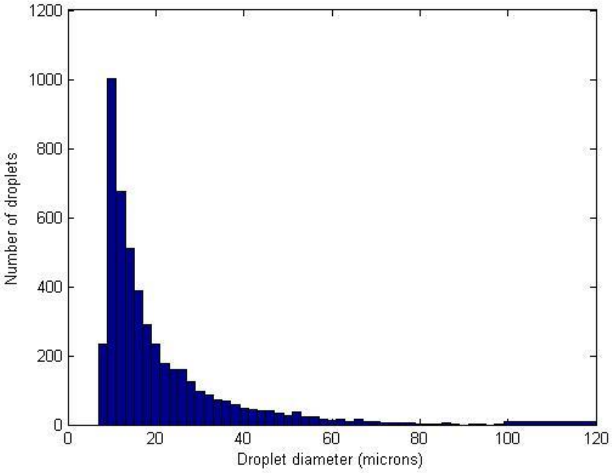

Figure 5.1a Drop size distribution of HFO spray with operating GLR=45, SMD=44µm.

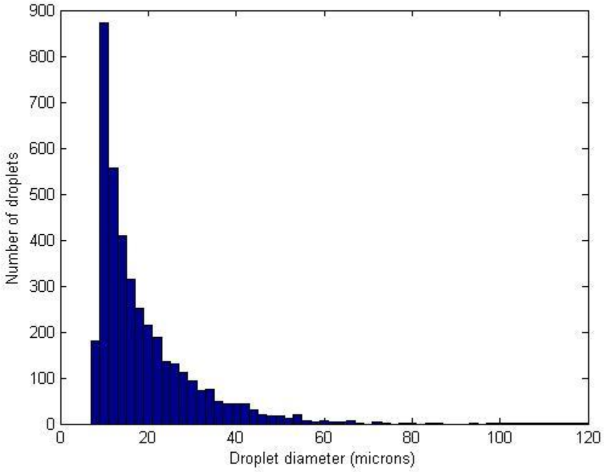

Figure 5.2b Drop size distribution of HFO spray with operating GLR=90, SMD=37µm.

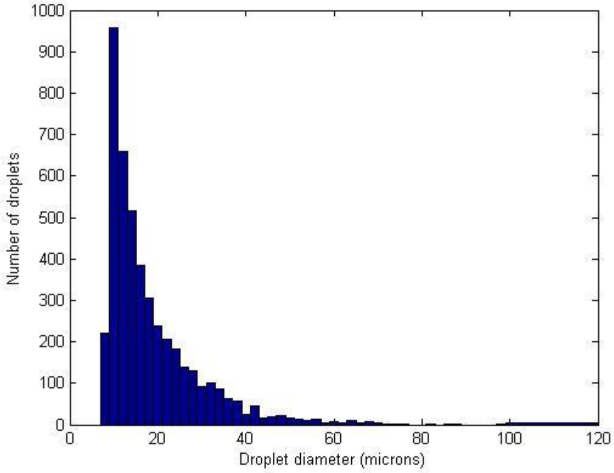

Figure 5.3b Drop size distribution of HFO spray with operating GLR=135, SMD=35µm.

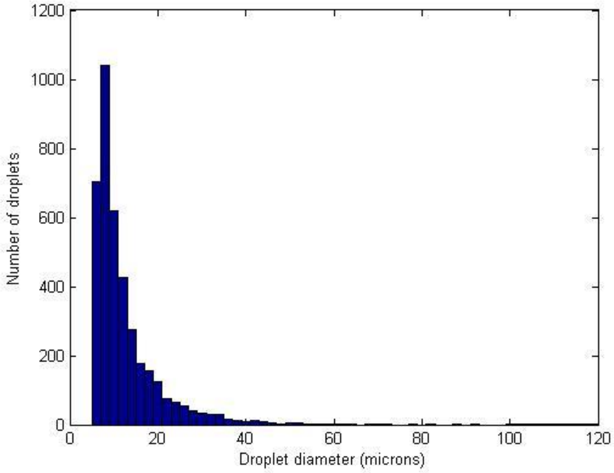

Figure 5.4b Drop size distribution of HFO spray with operating GLR=180, SMD=32µm.

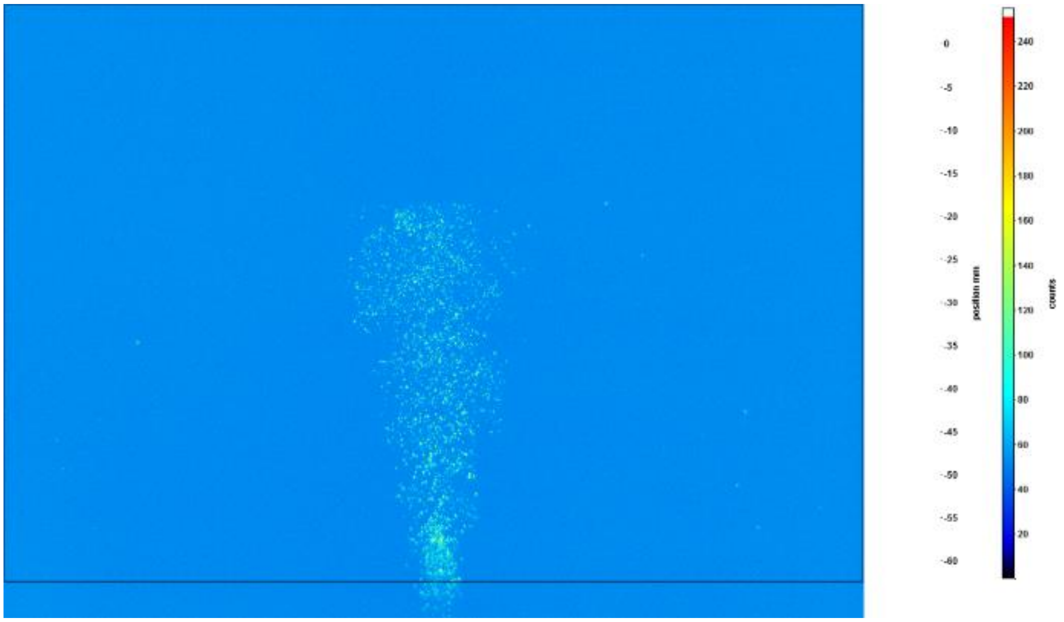

Figure 5.5a HFO spray dispersion in cold environment (Instantaneous Laser scattering image).

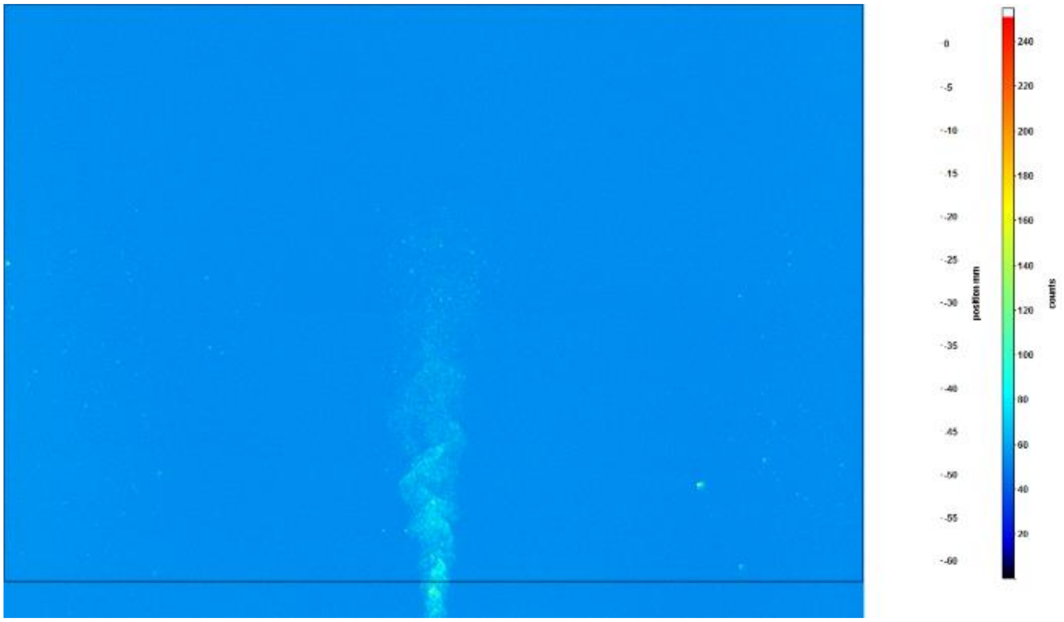

Figure 5.6b HFO spray dispersion in hot environment (Instantaneous Laser scattering image).

As previously discussed, the Particle or Drop Imaging analysis (PDIA) technique is then employed to directly image the HFO combusting spray. However, the images captured using this back-light shadowgraphy technique resulted in a blurring of droplet edges in images as shown in Figure 5.7. This made it difficult to estimate droplet diameters accurately. This blurring effect can be attributed to high-temperature gradients and the associated lensing effects due to the presence of the flame around the droplet.

The Interferometric Mie Imaging (IMI) technique is also employed for droplet imaging (refer Figure 5.8). However, similar blurring effects are observed. Hence, there is a need for a technique which will avoid this issue of high thermal gradients and image droplets with sharp boundaries.

A new strategy to image burning HFO droplets is proposed based on following points:

- To eliminate dependence on the backlight for imaging of droplets, it is desirable if droplets act as a light source.
- With lensing effect of thermal gradients, the burning droplets will show a shift in location. However, the droplet edge blurring in the image can be reduced to a large extent.
- The aromatics are one of the major constituents of HFO. They have strong tendency to fluoresce under UV excitation. These aromatics emit broadband fluorescence and a longer wavelength of 600 nm can be used to visualize droplet in spray environment.
- A Laser Induced Fluorescence technique using strong pulsed UV laser is employed to fluoresce HFO droplets in the combusting environment
- As observed earlier, fine droplets are produced in the combusting environment. Hence, a long-distance microscope (LDM) with 600-nm bandpass filter is used along with the

CCD camera for droplet visualization. A 532-nm notch filter is also used to eliminate any traces of the second harmonic in the 355-nm beam generated by Nd:YAG laser. Using LDM, the camera is focused onto a small window of 1.5-mm by 2-mm resulting in 2-μm spatial resolution.

- A fluorescence signal is typically weak and hence it is necessary to use Intensifier along with 2-MP camera.
- Instead of using a laser sheet, a focused laser beam is utilized to increase the laser intensity in small probe volume of ~ 1.5 mm^3.
- Using particle size image processing tools, a drop size distribution is obtained for HFO spray in burning environment. Figure 5.9 shows the schematic of this proposed new LIF technique.

Figure 5.10 shows a single shot image of droplet fluorescence captured using this technique. The raw image indicates a good signal to background intensity ratio. The boundary of droplets is also well distinguished. These images are further analyzed for determining droplet sizes using the Lavision post-processing tool. Figure 5.11 shows a post-processed LIF image with droplets identified and estimated droplet diameters. Table 5.1 shows different experimental cases for measurement of HFO droplet size distribution under different GLR and co-flow temperatures. For every case mentioned in Table 5.1, 500 LIF images are recorded to arrive at droplet size distribution of HFO spray in combusting environment.

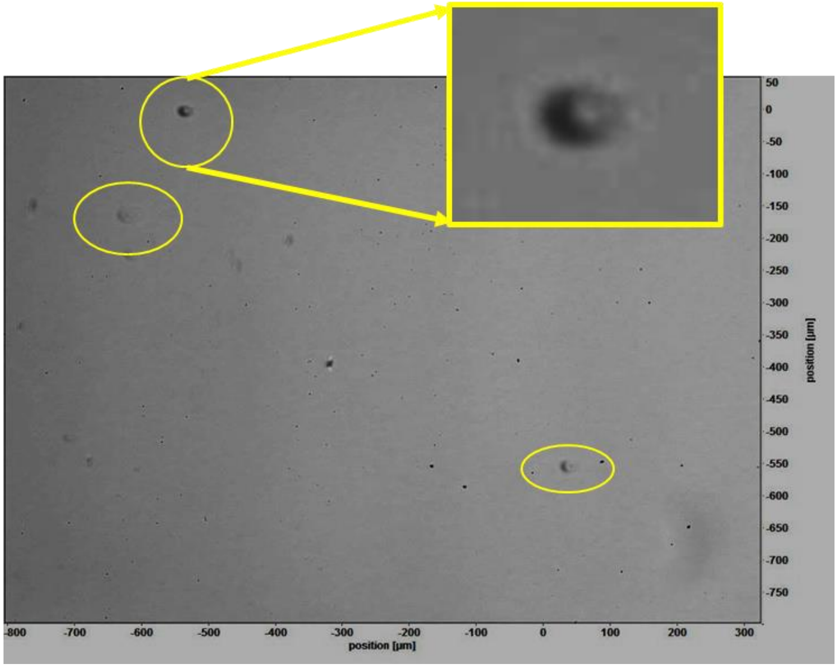

Figure 5.7 PDIA image of FO droplets in burning spray (raw image).

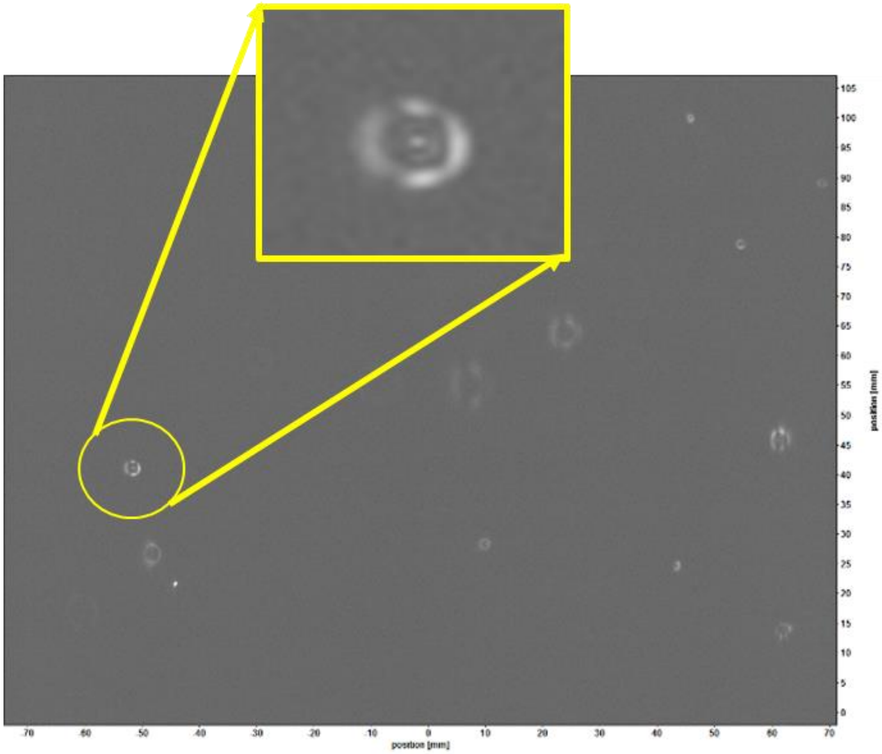

Figure 5.8 IMI image of FO droplets in burning spray (raw image).

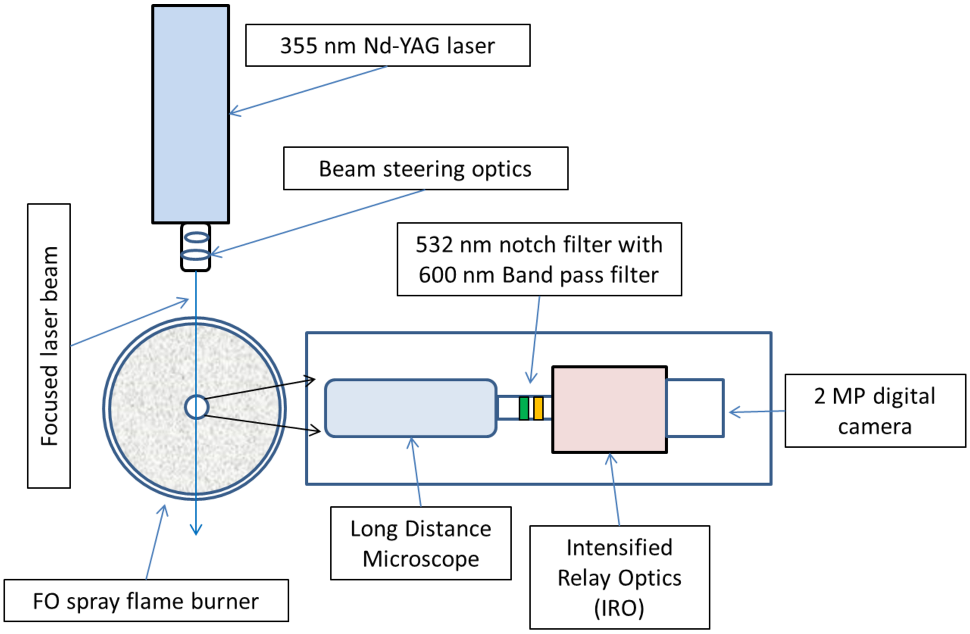

Figure 5.9 Newly proposed LIF optical diagnostic setup to capture HFO droplets in combusting spray environment.

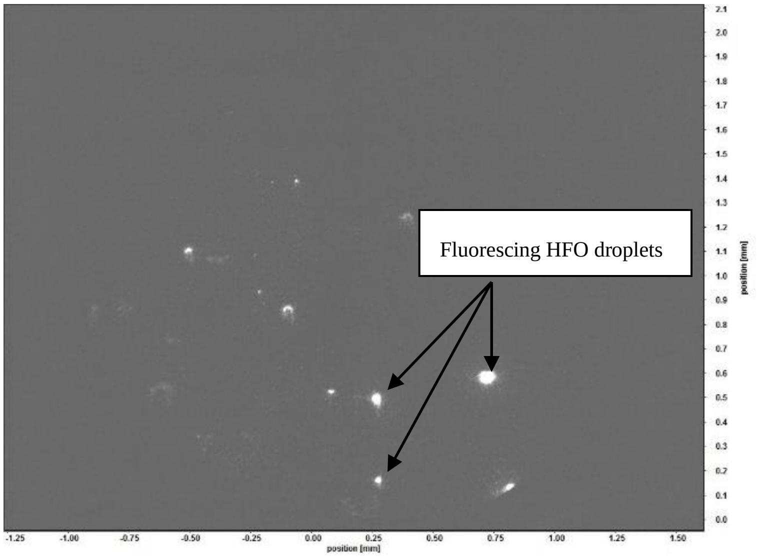

Figure 5.10 LIF image of HFO droplets in burning spray (raw image).

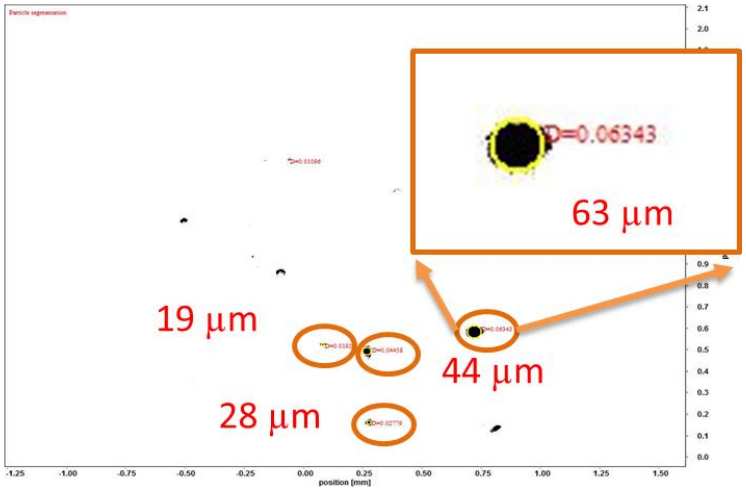

Figure 5.11 Post-processed image of FO LIF image.

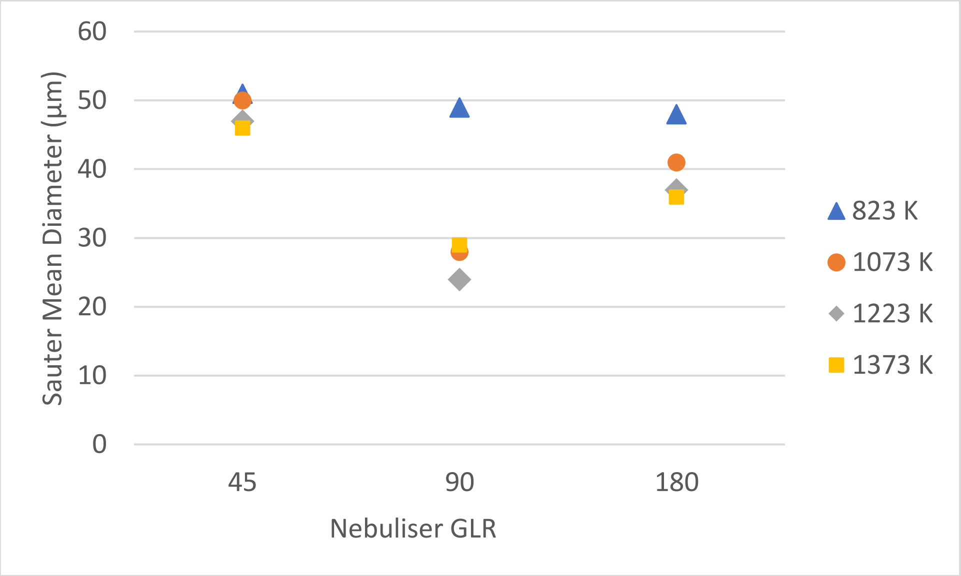

Figure 5.12 Effect of GLR on HFO spray SMD.

Case No.	FO flow (mlpm)	Atomising Gas N_2		Co-flow Air (lpm)	Co-flow O_2 (lpm)	Co-flow H_2 (lpm)	Co-flow Temperature °C	Co-flow O_2 content (% Volume)
		(lpm)	GLR					
1	0.02	0.5	45	40	2.5	5	550	20.4
2	0.02	0.5	45	40	7	10	800	21.5
3	0.02	0.5	45	40	10	15	950	20.34
4	0.02	0.5	45	45	12	18	1100	20.2
5	0.02	1	90	40	2.5	5	550	20.4
6	0.02	1	90	40	7	10	800	21.5
7	0.02	1	90	40	10	15	950	20.34
8	0.02	1	90	45	12	18	1100	20.2
9	0.02	2	180	40	2.5	5	550	20.4
10	0.02	2	180	40	7	10	800	21.5
11	0.02	2	180	40	10	15	950	20.34
12	0.02	2	180	45	12	18	1100	20.2

Table 5.1 Experimental matrix for different HFO spray GLRs and co-flow temperatures.

5.1.1 Effect of GLR on Drop size distribution

Figure 5.12 presents the droplet measurement results in a consolidated form. It is expected that SMD should decrease with increasing GLR and generate a higher number of finer droplets. However, the reverse trend is observed where the Sauter Mean Diameter (SMD) is found to increase as GLR increases from 45 to 180. This trend is same for higher co-flow temperature cases (1073 K to 1373 K) except for 823 K. It should be noted that higher GLRs are employed for this nebulizer and the atomization regime is expected to be in the catastrophic liquid jet breakup regime. Hence, the observed reverse trend may be attributed to higher coalescence probability due to larger droplet numbers and higher droplet exit velocities.

5.1.2 Effect of co-flow temperature on Drop size distribution

Higher co-flow temperatures are expected to aid secondary atomization as droplets viscosity will further reduce due to convective heating in the spray environment. Hence, with higher co-flow temperatures, the drop sizes and hence SMD should decrease. Figure 5.13 indicates similar trends for all 4 GLR cases. At lower temperatures of 823 K and 1073 K, a drastic reduction in SMD is observed. While the further increase in co-flow temperatures from 1073 K till 1373 K, this effect is lessened. Furthermore, the difference in SMD between GLRs of 90 to 180 reduces with higher co-flow temperatures.

Thus, a new methodology for drop sizing using PLIF is established to image fuel droplets in a combusting environment overcoming problems normally encountered in such environments. The drop sizing for HFO spray in burning environment is successfully carried out experimental operating conditions are identified for further investigation. The co-flow temperature has a more pronounced effect on the SMD of the HFO spray than the operating GLR of the nebulizer.

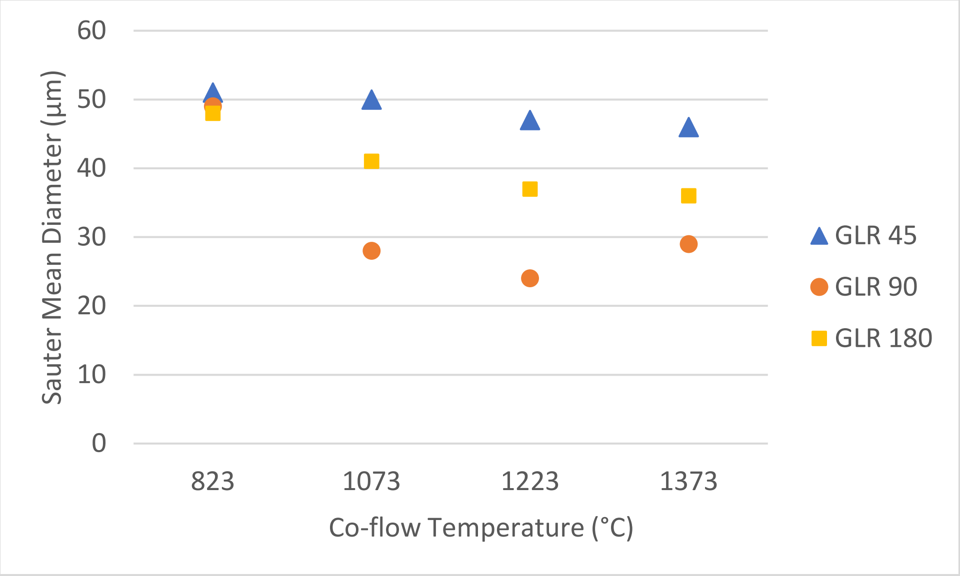

Figure 5.13 Effect of Co-flow temperature on HFO spray SMD.

6 Soot formation in HFO combustion

A wide range of carbon particulates (sizes ranging from 10-nm up to 100-µm) is generated during HFO combustion. These particulates are classified based on size range as ‘soot' for size ranging from 10-nm to 1-µm and ‘cenospheres’ for size ranging from 1-µm to 100-µm. The formation mechanisms for these two classes of carbon particulates are quite different. Soot is a result of condensation of polyaromatic hydrocarbons (PAH) on to carbon-rich nuclei formed during gas-phase combustion, while cenospheres are generated due to pyrolysis of HFO droplets during combustion. Hence, the particulate formation studies in HFO spray flames are divided into two parts, soot formation studies (Chapter 6), and cenosphere formation studies (Chapter 7).

During the HFO spray combustion, a major fraction of HFO evaporates rapidly and mixes with the oxidizing co-flow. This fuel-oxidizer mixture then burns as a diffusion flame. Due to the presence of a substantial fraction of aromatics in HFO, soot is formed during this phase of combustion. To investigate the effect of spray atomization and drop size distribution on soot formation, a planar LII technique, as explained in Chapter 3, is used. Using the measured HFO spray characteristics, standard cases are identified for further investigation and are listed in Table 6.1. The established experimental procedure for LII as described in Chapter 4 is then utilised to measure soot produced in HFO flames. **Error! Reference source not found.** shows a typical averaged soot volume fraction image of HFO spray flame, and a corresponding axial profile of soot volume fraction axial along the centerline is shown in Fig. 6.2.

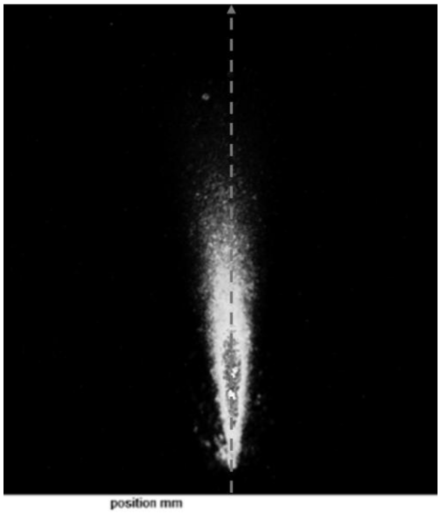

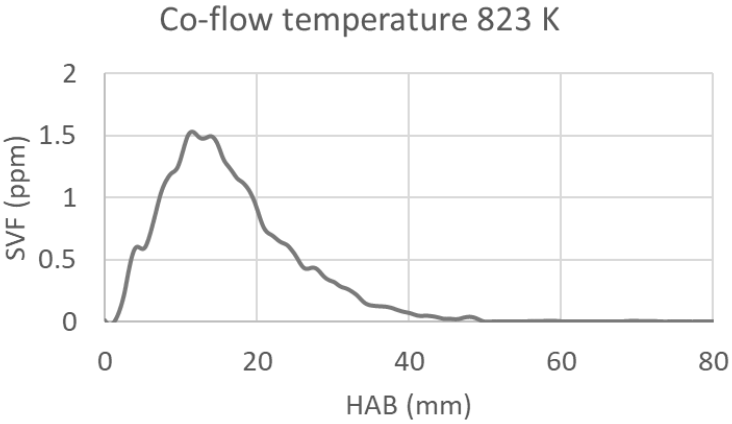

Figure 6.1 Soot volume fraction (fv) variation along centreline.

Figure 6.2 Average soot volume fraction (fv) image.

Case No.	SMD of HFO Spray (µm)	Co-flow temperature (K)
1	50	873
2	50	1073
3	50	1223
4	50	1373
5	32	873
6	32	1073
7	32	1223
8	32	1373
9	28	873
10	28	1073
11	28	1223
12	28	1373

Table 6.1 Nomenclature of experimental cases.

The soot volume fraction field shown in Fig. 6.1 indicates that for HFO spray flames, soot exists in regions where combustion is still prevalent. An axial profile of soot volume fraction indicates that soot is formed rapidly during between 0 to 15-mm HAB and peaks at 15-mm as shown in Figure 6.2. This soot is subsequently oxidized between 15-mm to 50-mm resulting in negligible net soot emission. This shows that the soot formed at lower heights is reactive and can be reduced under favorable conditions. Typically, soot formation and soot oxidation mechanisms are simultaneously active in the flame region due to high temperature and presence of oxygen. Hence, one cannot estimate soot formation and soot oxidation time scales based on the gradients of the soot volume fraction.

Figure 6.3 shows the soot volume fraction fields for the HFO spray with SMD 50-µm and different co-flow temperatures (cases 1 to 4 as defined in Table 6.1). It can be observed that for co-flow temperatures of 1223 K (case 3) and 1373 K (case 4), there is substantial reduction in peak soot volume fraction as well as the height of soot volume fraction field as compared to the cases with lower temperatures of 823 K (case 1) and 1073 K (case 2).

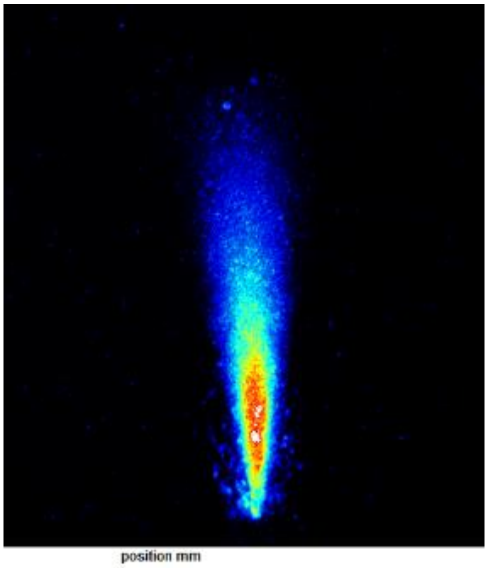

(Case 1) SMD 50 µm, Co-flow temperature 823 K

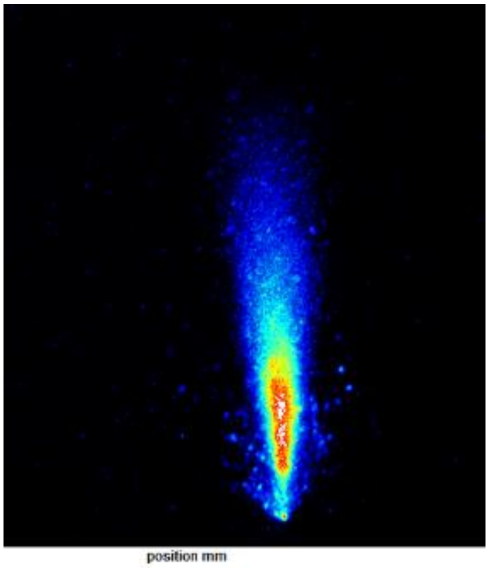

(Case 2) SMD 50 µm, Co-flow temperature 1073 K

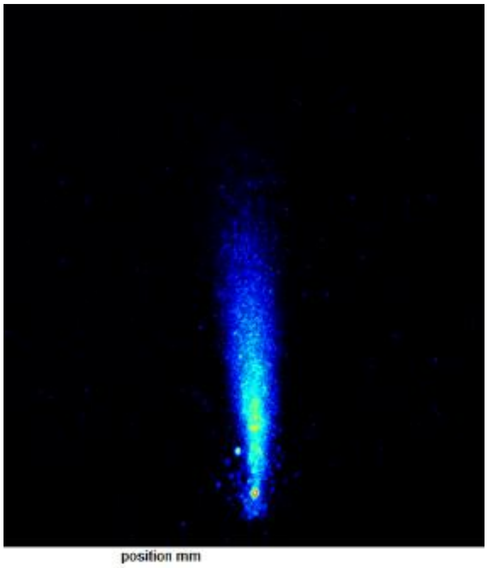

(Case 3) SMD 50 µm, Co-flow temperature 1223 K

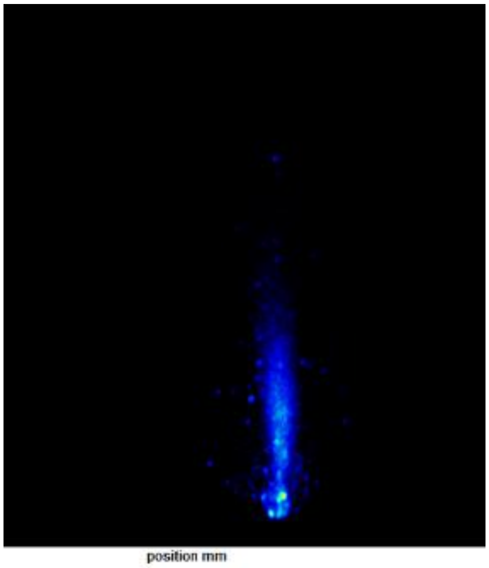

(Case 4) SMD 50 µm, Co-flow temperature 1373 K

Figure 6.3 Soot volume fraction fields for HFO spray with SMD 50-µm at different co-flow temperatures (Cases 1 to 4).

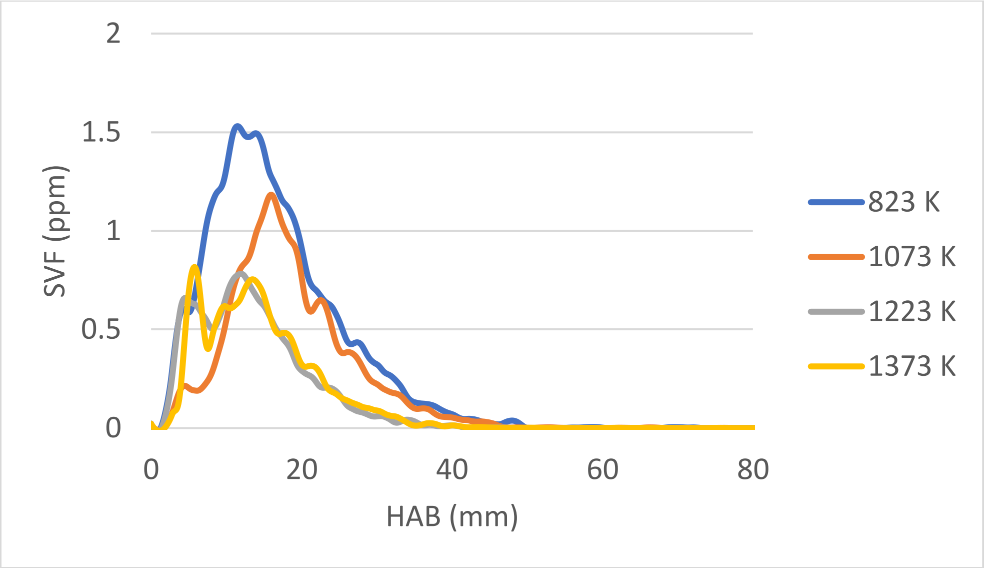

Figure 6.4 Effect of co-flow temperature on soot volume fraction for HFO spray combustion (HFO spray cases 1 to 4).

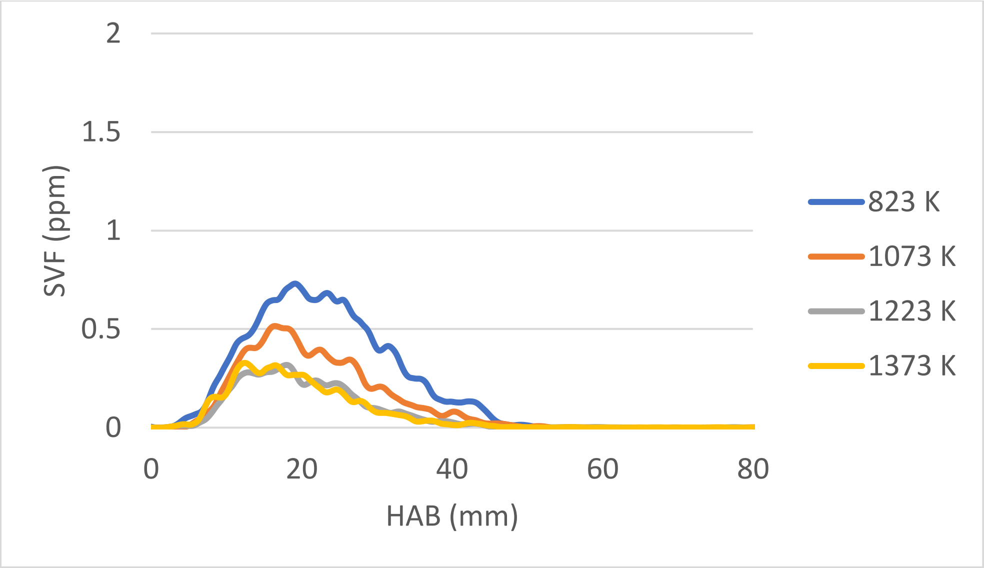

Figure 6.5 Effect of Co-flow temperature on Soot volume fraction for HFO spray combustion (HFO spray cases 9 to 12).

Ikegami et al. [21] has reported similar observations for HFO droplet combustion and concluded that temperatures above 1100 K are favorable for soot burnout. Hence, we can state that reduced soot peak and lower soot heights for higher temperatures cases (3 & 4) of 1223 K and 1373 K are due to higher rate of soot oxidation. This effect of co-flow temperature on soot formation is evident from a comparison of axial profiles of soot volume fraction as shown in Figure 6.4.

Similarly, the soot volume fraction fields for HFO spray with SMD 28-µm and different temperature cases (cases 9 to 12) are shown in Figure 6.6. Similar trends of reduced peak soot volume fraction and reduced height of soot region with an increase in co-flow temperatures are observed in HFO spray combustion cases 9 to 12. The axial profiles of soot volume fraction for these cases are shown in Figure 6.5. By comparing the cases 1 to 4 with SMD of 50-µm with cases 9 to 12 with SMD of 28-µm, it is evident that for the lower SMD case, the soot region has larger spread as well as height. It should be noted that smaller spray SMDs are achieved by increasing GLR of the nebulizer. This results in higher initial droplet velocities as well as higher air entrainment at lower heights of spray. This is also evident from comparison of axial profiles as shown in Figure 6.4 and Figure 6.5, where the soot is present till the height of about 35-mm HAB for the case 4, whereas it is present up to a height of 45 mm for case 12. The increased heights of soot regions can be attributed to higher initial droplet velocities. The wider spread of soot regions at lower heights can be a result of vigorous air-fuel vapor mixing at these heights.

Figure 6.11 shows the consolidated results of LII experiments, comparing different spray characteristics at same co-flow temperatures. It is observed that HFO sprays with smaller SMDs consistently result in lower soot volume fraction peaks. Figure 6.15 shows the effect of co-flow temperatures comparing all cases.

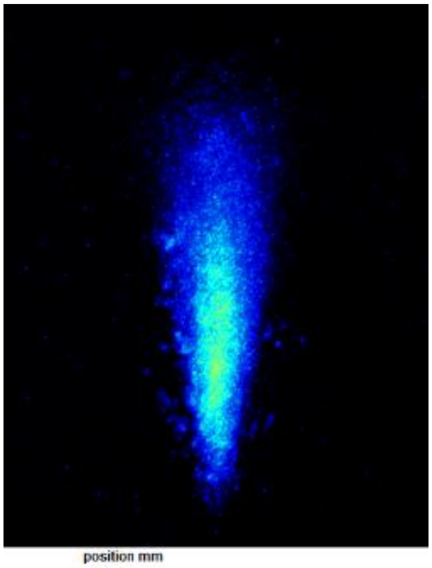

(a) Co-flow temperature 823 K.

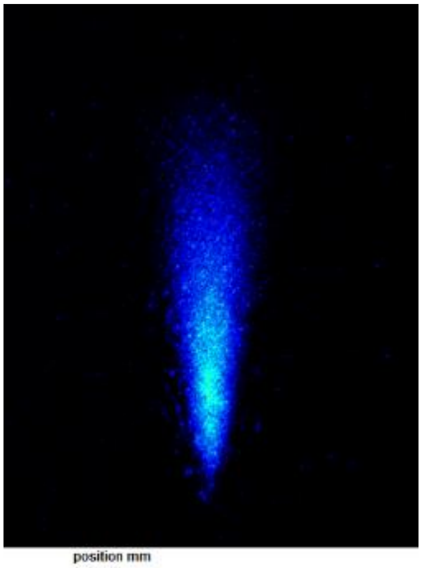

(b) Co-flow temperature 1073 K.

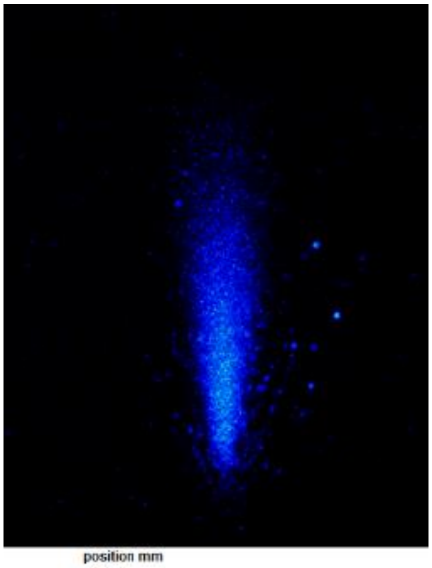

(c) Co-flow temperature 1223 K.

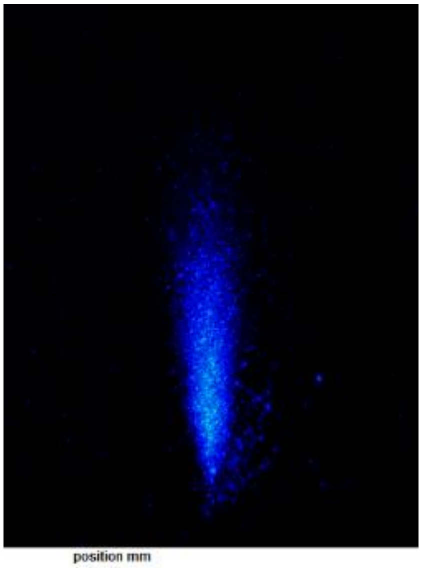

(d) Co-flow temperature 1373 K.

Figure 6.6 Soot volume fraction fields for HFO spray (cases 9 to 12) at different co-flow temperatures.

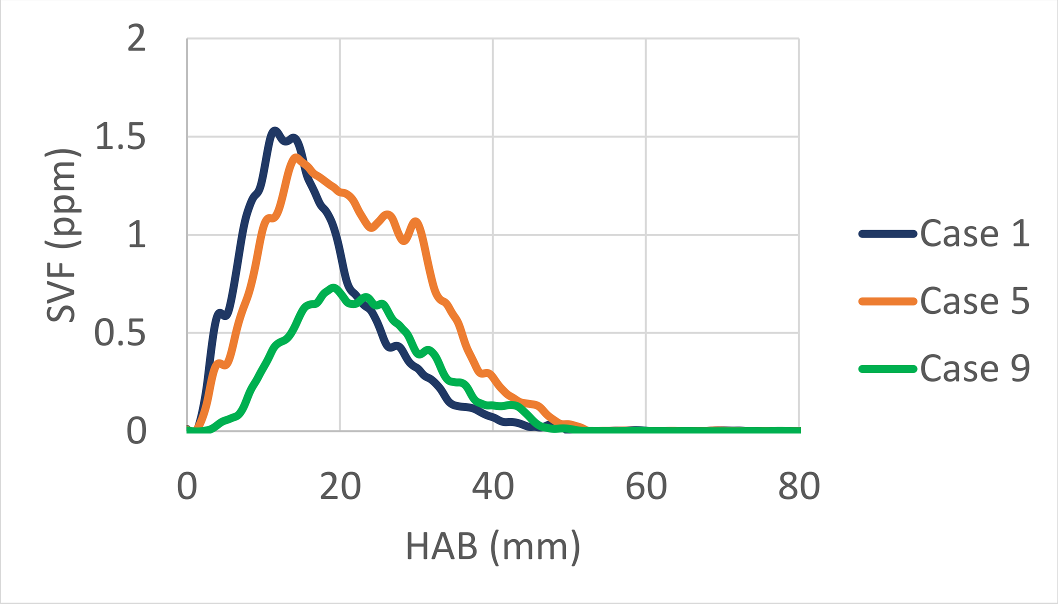

Figure 6.7 (a) Co-flow temperature 823 K (cases 1,5,9).

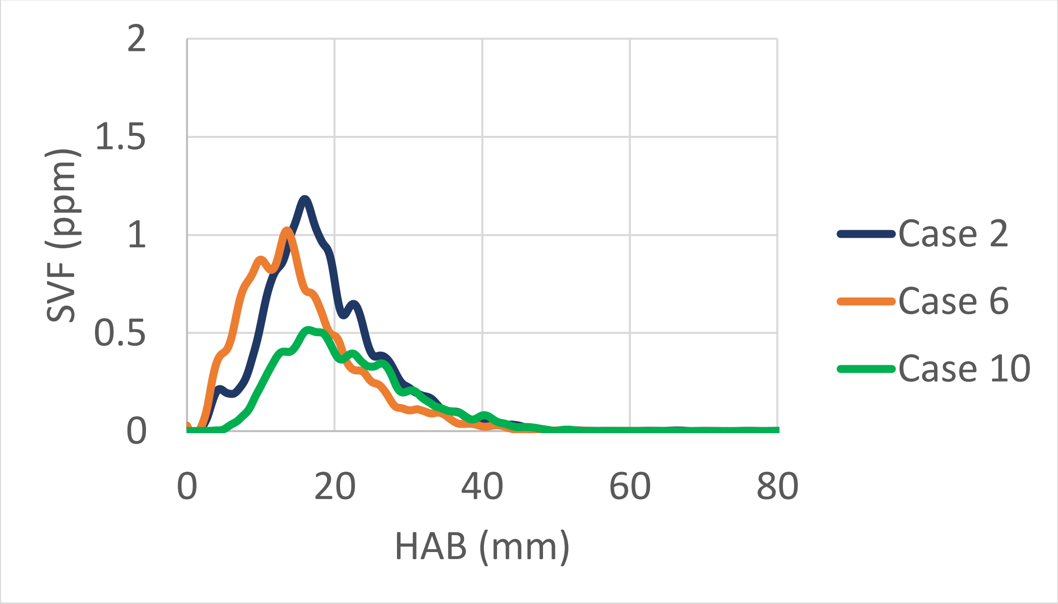

Figure 6.8 (b) Co-flow temperature 1073 K (cases 2,6,10).

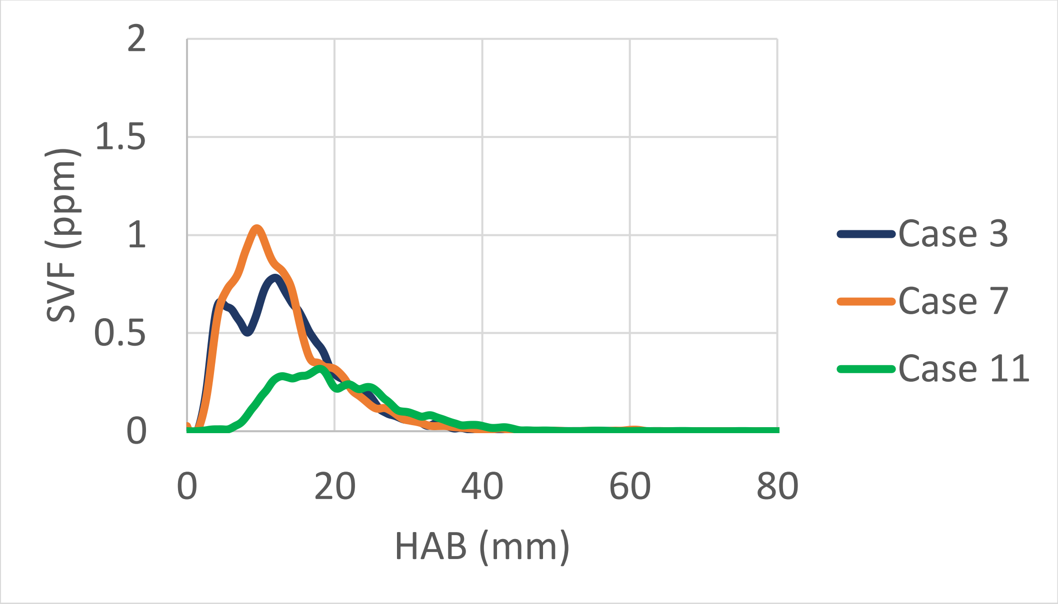

Figure 6.9 (c) Co-flow temperature 1223 K (cases 3,7,11).

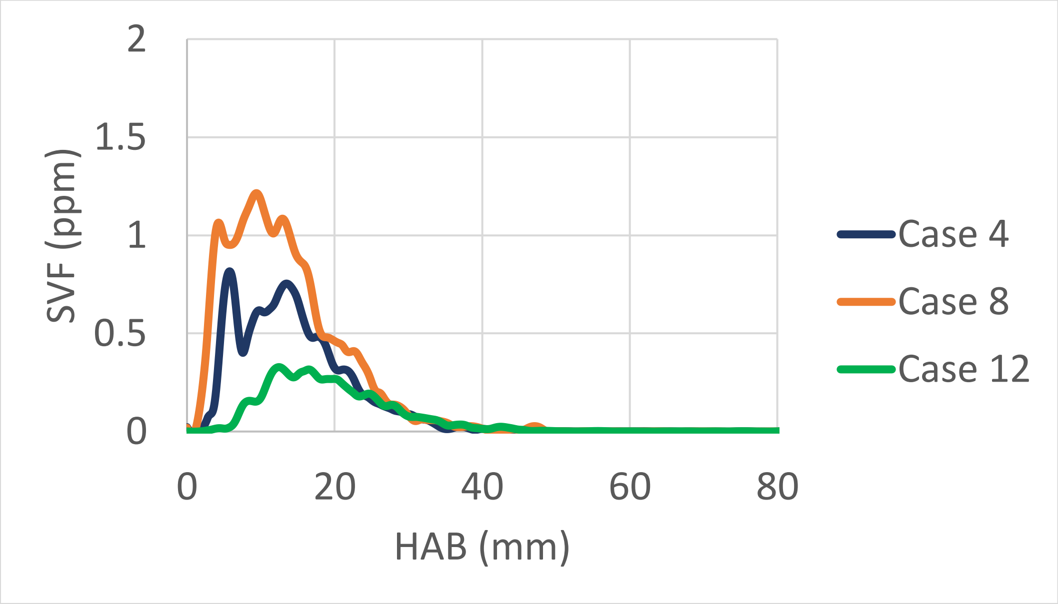

Figure 6.10 (d) Co-flow temperature 1373 K (cases 4,8,12).

Figure 6.11 Effect of HFO spray SMD on Soot volume fraction for HFO spray combustion.

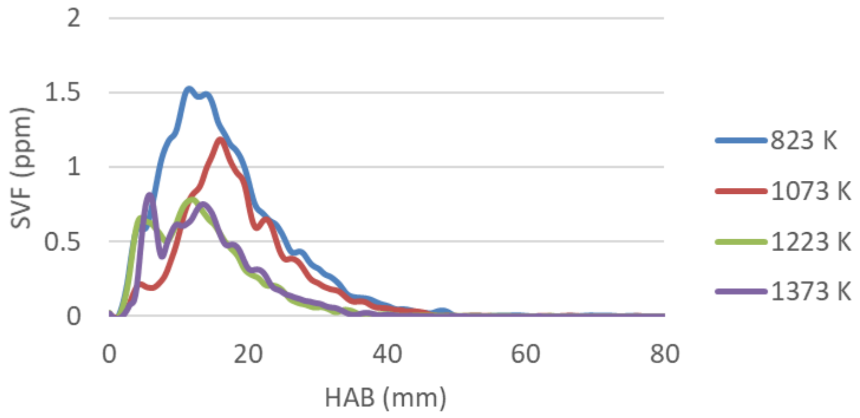

Figure 6.12 (a) HFO spray SMD 50-µm (cases 1 to 4).

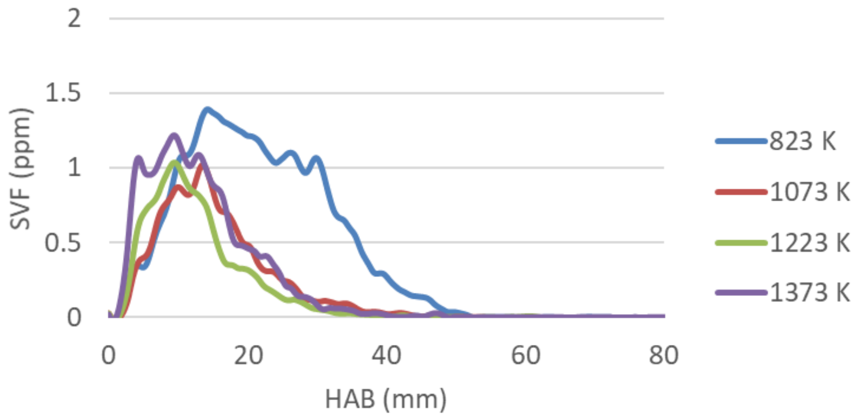

Figure 6.13 (b) HFO spray SMD 32-µm (cases 5 to 8).

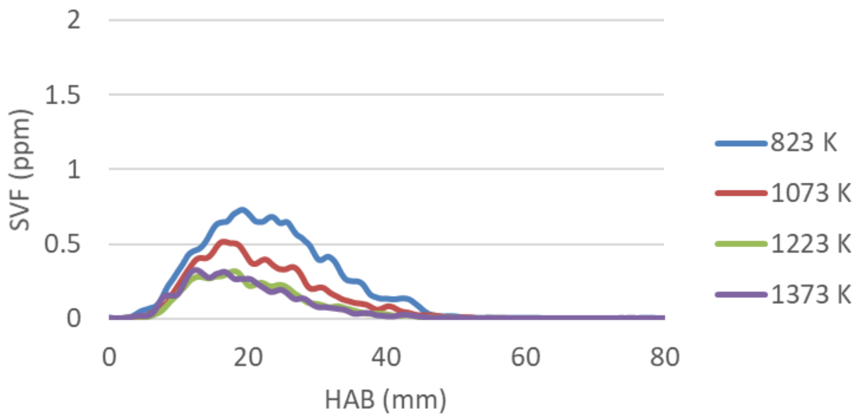

Figure 6.14 (c) HFO spray SMD-28 µm (cases 9 to 12).

Figure 6.15 Effect of Co-flow temperatures on Soot volume fraction at different GLR conditions.

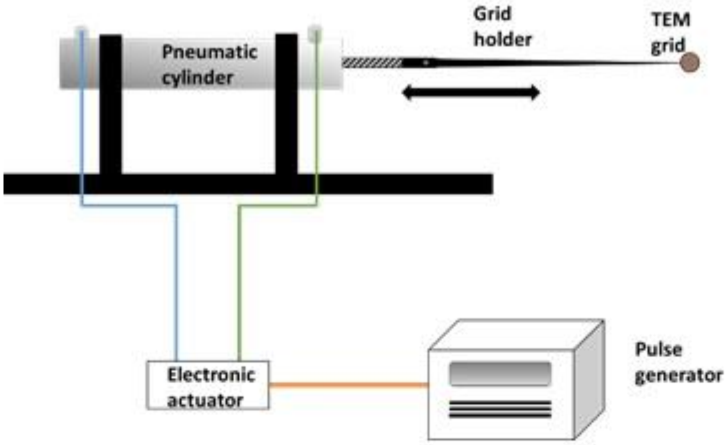

Figure 6.16 Thermophoretic sampling probe setup.

Comparing the soot volume fractions for higher co-flow temperature cases of 1223 K and 1373 K (cases 3 & 4, 7 & 8, 11 & 12), the soot volume fraction profiles are almost coincident for all different spray characteristics. Hence, it can be concluded that, for soot reduction, temperatures upwards of 1223 K are optimal.

The primary particle size is an important morphological aspect of soot. To investigate the effect of HFO spray characteristics and co-flow temperatures on a primary particle size, it is necessary to physically sample soot and perform a microscopic investigation. A thermophoretic sampling technique is used to physically collect samples of soot being emitted from HFO spray flames. A TEM copper grid, coated with 10-nm carbon film (*Cu-200 make: TED PELLA 01810)* is used to deposit soot using thermophoretic sampling technique. A Transmission Electron Microscopy (TEM) technique is used to investigate primary soot particles.

A retractable probe arrangement is designed to control the exposure time of TEM grid to hot gases produced by HFO combustion. A schematic of this setup is shown in Figure 6.16. The retracting action is achieved using a pneumatic cylinder with a stroke guide. The TEM grid is mounted on a grid holder at the tip of pneumatic cylinder rod as shown in Figure 6.16. The pneumatic cylinder stroke is controlled using an electro-pneumatic valve and the duration of exposure of the TEM grid is controlled by the pulse-width of the trigger signal. The probe is maintained at a height of 150-mm above burner to avoid direct exposure of TEM grids to flame. The exposure time of the grids in the flame was limited to 100-150 ms to maintain the integrity of the carbon coating on the grid and to avoid surface growth of soot particulates. Multiple insertions are necessary to collect a sufficient number of soot deposits on the grid, as the soot volume fractions measured are less. A gap of about 10-15 seconds was provided in between consecutive insertions so as to cool down the grid to ambient temperatures. The samples collected stored in a desiccator for 12 hours before TEM investigation. A U-Twin transmission electron microscope (make FEI Tecnai, model: D2060) is used for TEM imaging. For all HFO combustion cases, negligible or no soot deposition is observed on TEM grids. This supports earlier observations of negligible soot volume fraction measured at higher flame heights.

Thus, from above soot formation studies, the following conclusions can be derived:

- Soot formed during HFO spray combustion is reactive and can be completely oxidized under optimal environmental conditions,
- It is observed that a temperature above 1223 K and oxygen availability are favorable for soot oxidation.

7 Cenosphere formation in HFO combustion

Heavy fuel oil contains heavier hydrocarbons called asphaltenes, which exhibit higher distillation temperatures (> 1000 K) and hence, do not evaporate completely during combustion. The incomplete droplet evaporation results in droplet pyrolysis thereby generating a coke particle or cenosphere [2]. Typically, an HFO droplet undergoes combustion in two stages, i.e., droplet phase combustion and solid (coke) phase combustion [22]. In literature [3][20][21][22], it is stated that ‘One HFO droplet generates one cenosphere', however, there is no experimental evidence for this hypothesis. As described earlier in Chapter 6, cenospheres have a size ranging from 1-µm to 100-µm. To study cenospheres generated in the research burner, the emitted particulates are deposited on a ceramic filter with a porosity of 3-µm. These particulates are collected after the visible flame is extinguished. The particulates accumulated on a filter are dried using a hot air gun to remove moisture and are stored in a desiccator. A digital microscope (make: Leica) is used to record digital images of the cenospheres and estimate their sizes. Figure 7.1 shows cenospheres as imaged by the digital microscope. It is observed that the surfaces of the cenospheres are continuous and largely non-porous. However, the cenospheres reported in the literature are largely porous. It is believed that these cenospheres are early stage coke particles generated at the end of droplet combustion phase and have not yet experienced a solid phase combustion phase. Similar early phase coke particles generated by HFO droplet combustion are reported elsewhere [56]. In the HFO spray, a visible flame surrounds the injected droplets where they burn in droplet combustion phase and as the volatile content in droplets is burnt, the flame surrounding the droplets extinguishes.

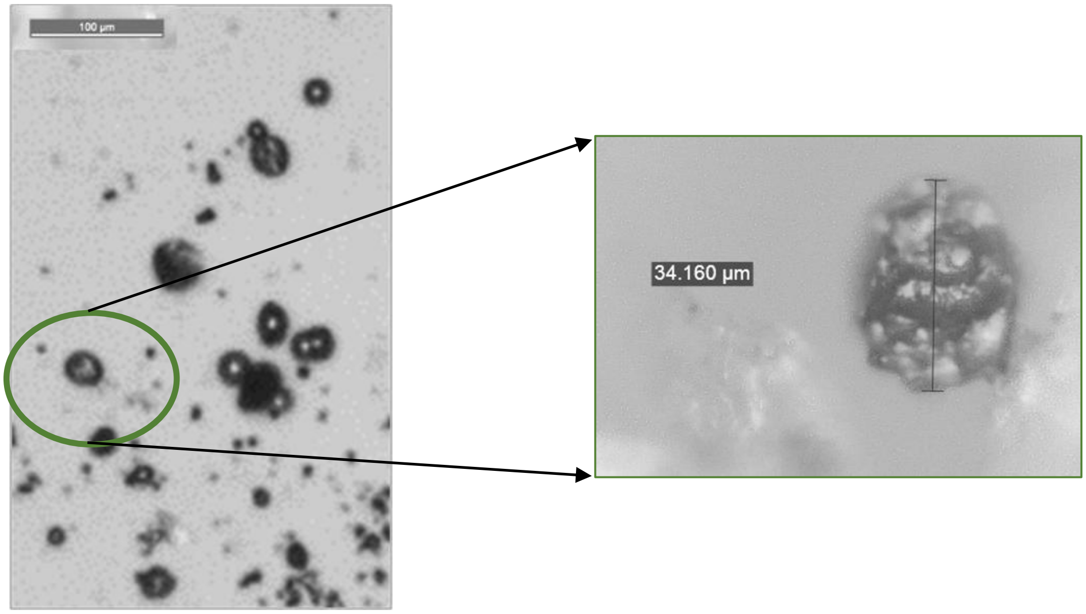

Figure 7.1 Cenospheres as observed under a digital microscope.

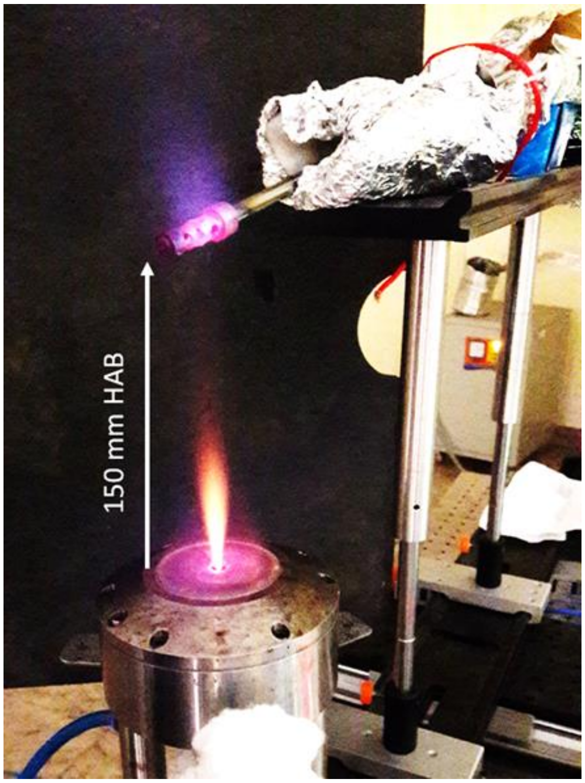

Figure 7.2 Flue gas sampling setup for Aerodynamic particle sizer.

The particulates are collected at a height where there is no visible flame, thus, the particulates do not undergo solid phase combustion. This explains the appearance of the early stage cenospheres observed under the microscope. To investigate the effect of HFO spray characteristics on cenosphere emissions, quantitative data on cenosphere emissions is required. An aerodynamic particle size spectrometer, introduced in section 3.4, is used to quantitatively measure cenosphere emission density and particle size distribution in exhaust gases. To avoid particulate separation in the probe, it is necessary that the suction probe is properly sized and has minimum bends. An L-shaped tube with 18-mm inner diameter and 100-mm radius of curvature is used as a probe for sampling of flue gases. The flue gas with particulates is sucked using this probe at a height of 150-mm above the fuel injection point as shown in Figure 7.2. It should be noted that this instrument can handle particle-laden flows only at room temperature. Hence, water cooling is provided to cool the exhaust gas before it reaches the instrument inlet. The cenosphere/particulate measurements are performed over a period of 60 seconds for all cases.

Figure 7.3 shows the cenosphere/particle size distribution recorded for an HFO spray with 28-µm SMD and a co-flow temperature of 1073 K (case 6). It can be observed that the cenosphere size distribution exhibits double peaks centered at 1.2-µm and 1.7-µm and the size range is between (~ 0.7-µm to 6.7-µm). It is also observed that the resolution and range of the instrument sufficient for the required measurements. Figure 7.4, Figure **7.5** and Figure **7.6** show the effect of co-flow temperatures on particle size distribution for the same HFO spray characteristics, i.e., maintaining the spray SMD constant.

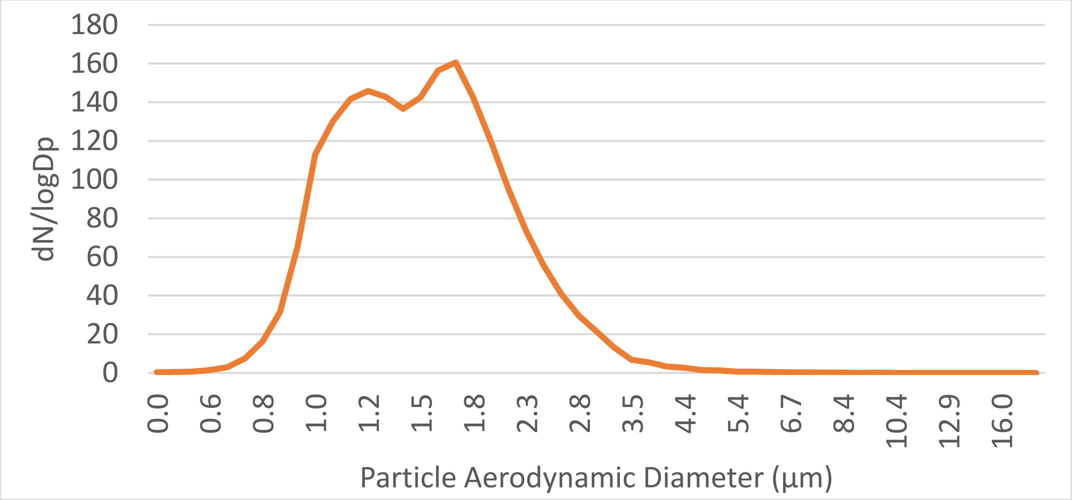

Figure 7.3 Cenosphere size distribution for HFO spray with SMD 28-µm and co-flow temperature of 1073 K (case 6).

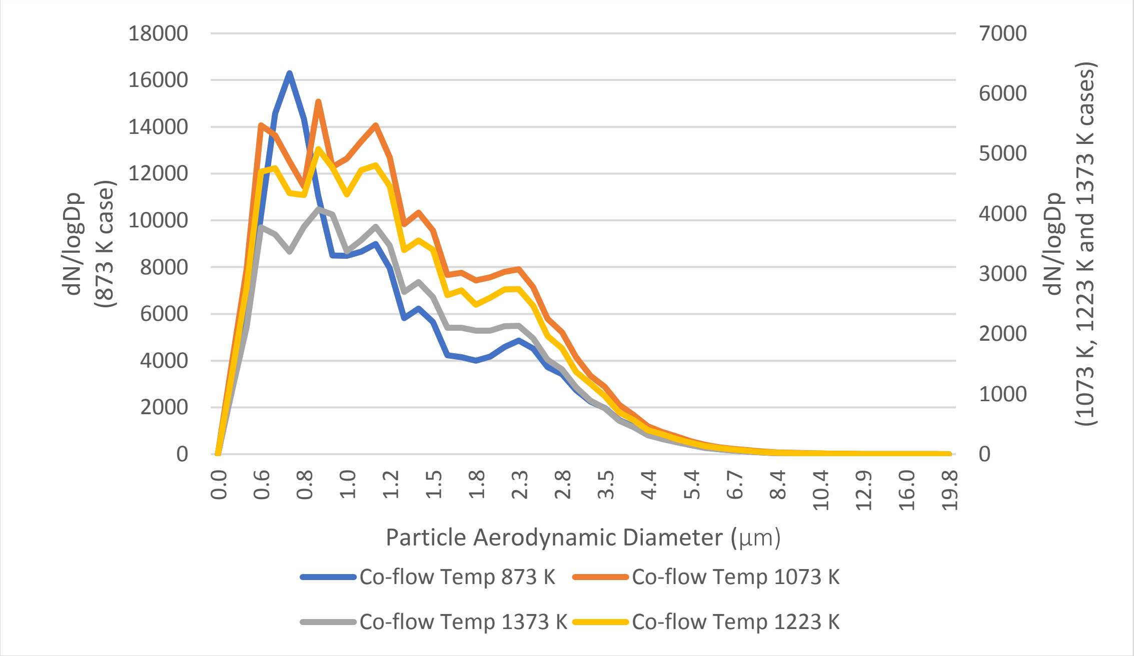

Figure 7.4 Comparison of Cenosphere size distribution for a constant HFO spray SMD of 50-µm (cases 1 to 4).

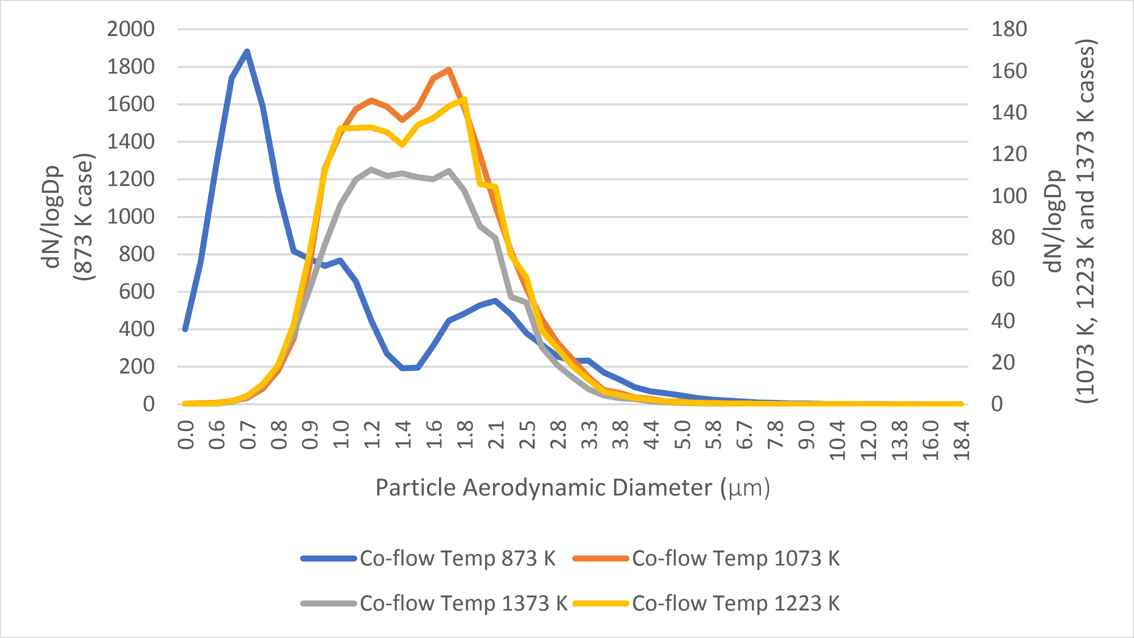

Figure 7.5 Comparison of Cenosphere size distribution for a constant HFO spray SMD of 32-μm (cases 5 to 8).

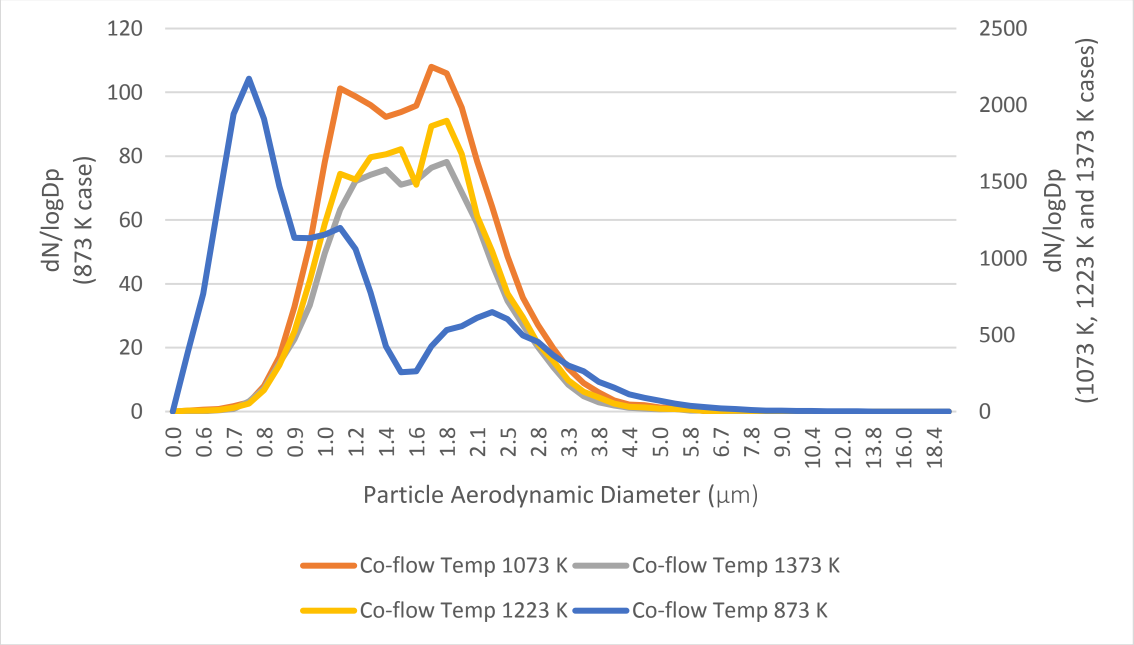

Figure 7.6 Comparison of Cenosphere size distribution for a constant HFO spray SMD of 28-μm (cases 9 to 12).

For the HFO spray corresponding to SMD 50-µm, as the co-flow temperature increases from 873 K to 1373 K (case 1 to 4), the emitted cenosphere size range is between 0.5-µm to 6-µm. The particle count in respective bins decreases with increase in temperature. With a lower co-flow temperature of 823 K, a considerably large number of particles peaking at 0.7 µm are emitted as compared to higher co-flow temperatures of 1073 K, 1223 K, and 1373 K. For the HFO spray corresponding to SMD=32-µm, for lower co-flow temperature of 873 K (case 5), the cenosphere size distribution shows two peaks at 0.6 µm and 2.1 µm. With the increase in co-flow temperature from 873 K to 1073 K (cases 6 to 8), these peaks disappear and the size distribution resembles a normal distribution centered at 1.4-µm particle size. The cenosphere sizes below 0.7-µm and above 5.3-µm completely disappear at higher co-flow temperatures (> 1073 K). The size distributions for co-flow temperatures of 1073 K, 1223 K, and 1373 K (cases 6 to 8) are similar with a slight decrease in a number of particles in the respective bins near to the mean value of 1.4-µm. For the HFO spray with SMD=28-µm (cases 9 to 12), similar trends are observed. It should be noted that the number of particles in bins near to the mean particle value of 1.4-µm is further lowered with lower SMD. Thus, comparing Figure 7.4, Figure **7.5** and Figure **7.6**, it is observed that, for co-flow temperatures less than 1073 K, irrespective of the SMD, the HFO combustion gives rise to higher cenosphere emissions (particle number emissions) at all size ranges below 6.7-µm. However, with co-flow temperatures in excess of 1073 K, the cenosphere emissions are reduced considerably and the trends are consistent for all cases. The aerodynamic particle sizer also measures particle number density in the exhaust gases. Figure 7.7 shows the impact of the spray SMD and the co-flow temperature on cenosphere particle number density (number/cm^3). It is generally observed that the cenosphere number density in exhaust decreases with increase in co-flow temperatures from 823 K to 1373 K.

Furthermore, for lower SMDs (<= 32 µm), the cenosphere number density emitted is orders of magnitude lower than that for SMDs in the range 50-µm.

Thus, it can be conclusively stated that HFO spray SMD below 40-µm and co-flow temperatures in excess of 1073 K are favorable for a reduction in cenosphere emissions. It should be noted that at a constant HFO flow rate of 0.02 mlpm, the lower SMD spray should generate a higher number of HFO droplets. Hence, considering the assumption of ‘One HFO droplet generated at least one cenosphere', the cenosphere emission density (particle number/cm^3) should increase as well as the size pf cenospheres should shift towards lower size ranges. This however is not observed in the experiments. It seems that the smaller droplets undergo complete combustion without coke formation and fewer droplets undergo droplet pyrolysis leading to reduced cenosphere emissions. This also indicates the existence of a critical HFO droplet size below which droplets undergo complete evaporation and combustion without experiencing solid phase combustion.

7.1.1 Particle/cenosphere emission statistics:

The results of particle size spectroscopy indicate the existence of critical droplet diameter below which no cenosphere/coke particle is formed during combustion. The HFO injector generates a wide range of droplet sizes, hence it is not possible to experimentally estimate the critical droplet size by altering the spray drop size characteristics. A different methodology is thus adopted towards correlating the number of HFO droplets injected and the number of cenospheres generated. The droplets/particulates in a combusting spray are studied using Laser Mie-scattering imaging.

A Mie-scattering setup is shown in Figure 7.8. As the size of droplets and particulates are greater than 0.5-µm, the frequency-doubled out of a Nd:YAG laser (532-nm) is used for the Mie-scattering experiments. A typical instantaneous Mie scattering image of droplets/particles in an HFO combusting spray is shown in Fig. 9. Mie-scattering images are captured at each of the five heights marked by a 5-mm high and 20-mm wide box as shown in Figure 7.9. The image resolution is maintained at 0.5-µm/pixel such that all particles above 0.5-µm are captured. Using the LaVision post-processing software, the particles are identified and a total number of particles at each height is estimated. The particles identified at 20-mm height above burner (HAB) are treated as a total number of HFO droplets injected while the particles captured at 90-mm HAB are treated as coke/cenosphere particles, as there is no visible flame at this height. To validate this technique for particle number statistics, this technique is first applied on a cold spray where the number of particles injected is conserved. It was observed that the number of the particle detected at different heights was within +/- 5% as compared to the number of particles measured at 20-mm HAB. After validation, this technique is then applied to all the 12 cases under consideration.

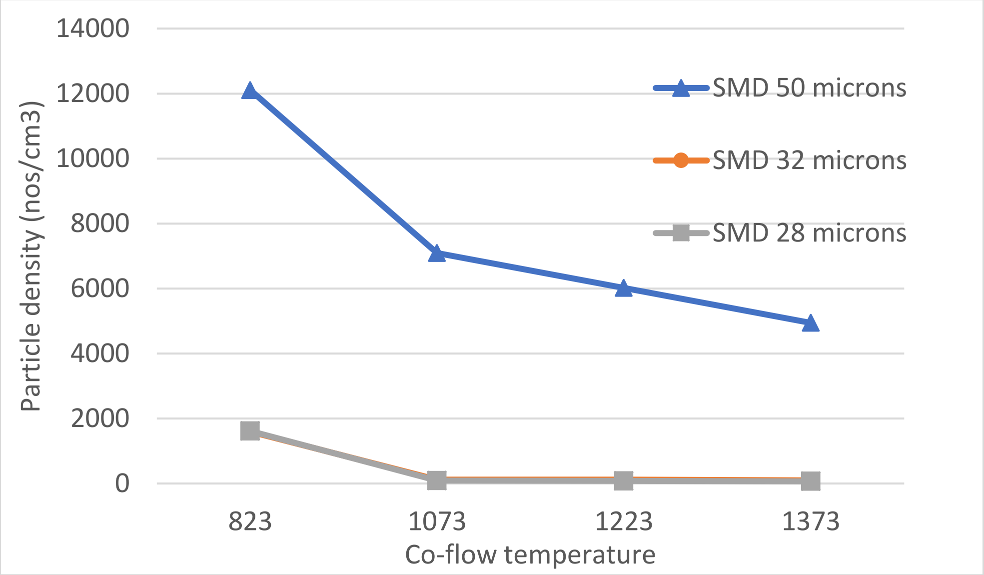

Figure 7.7 Effect of co-flow temperature on cenosphere emission particle density (Nos/cm3) for different HFO spray SMDs.

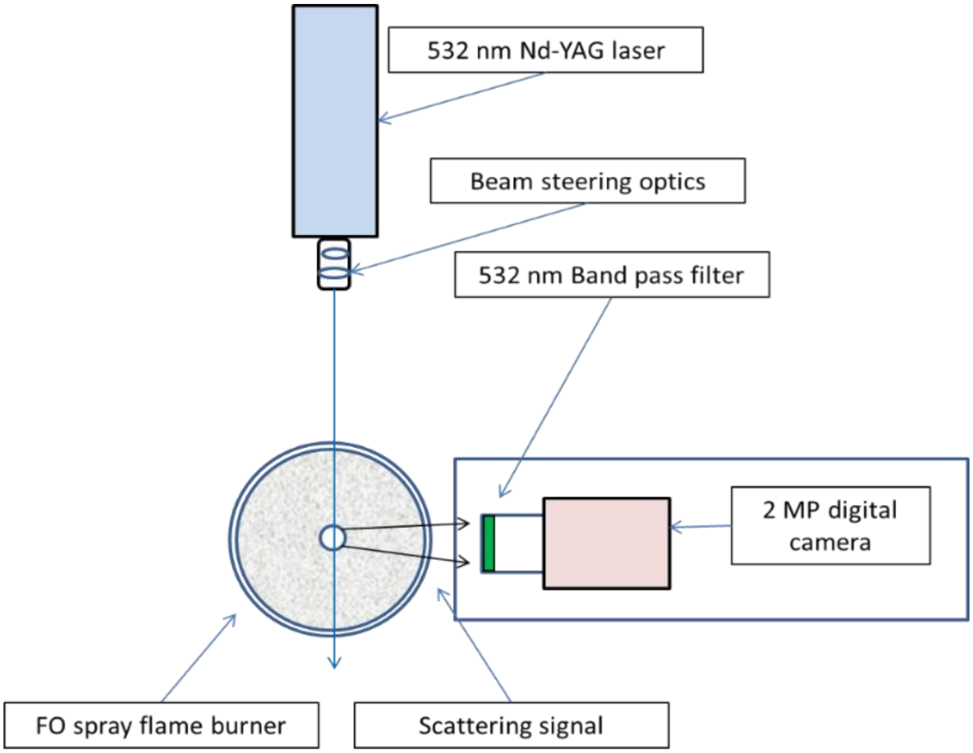

Figure 7.8 Mie scattering imaging setup.

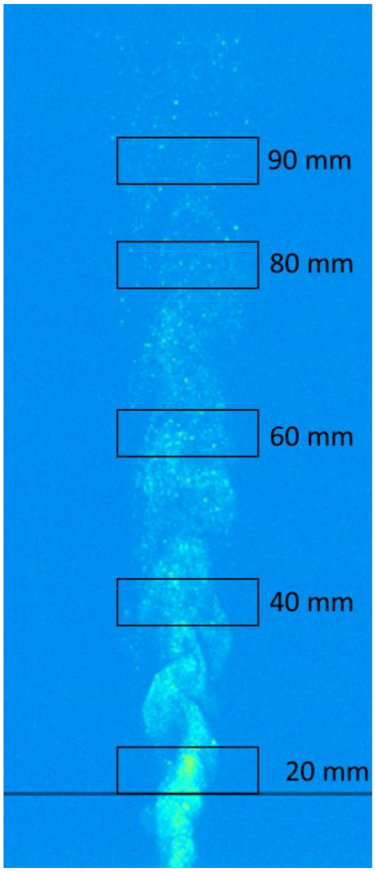

Figure 7.9 Instantaneous Mie scattering image of combusting HFO spray.

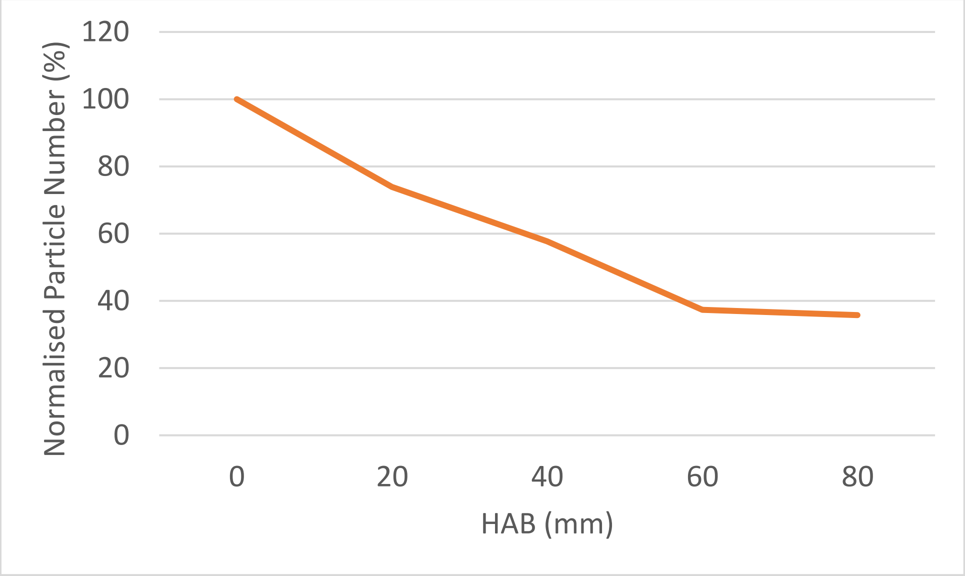

Figure 7.10 Normalised particle number along with the axis for HFO spray with 28 µm SMD and co-flow temperature of 1073 K (case 10).

Figure 7.10 shows the normalized number of particles estimated at different heights for an HFO spray with a 28-µm SMD and co-flow temperature of 1073 K (case 10). The total number of particles estimated at 20-mm HAB is used as a reference for normalization. It clearly shows that the total number of particles is gradually decreases along the flame length. Also, it shows that 64% of the HFO droplets are completely burnt and around 36% of the HFO droplets get converted into coke particles or cenospheres. This observation confirms the results of particle size spectroscopy that a certain fraction of HFO droplets undergo complete combustion without leaving any solid residue. This methodology is used to estimate the number of HFO droplets resulting in cenosphere emissions. This is then corelated with the HFO spray characteristics to determine the critical HFO droplet diameter.

Figure 7.11 shows the effect of co-flow temperature on the normalised particle number along flame height for a constant SMD of 50-µm. It can be observed that as the co-flow temperature rises from 823 K to 1223 K (cases 1 to 3), the normalized particle number decreases (from 74% to 48% for HAB-90 mm), i.e., a number of HFO droplets undergo complete combustion. However, on further increase in co-flow temperature to 1373 K (case 4), the normalized particle number is higher as compared to that of case 3 with co-flow temperature of 1223 K, at all heights. This may be attributed to early droplet pyrolysis promoted by higher surrounding temperatures.

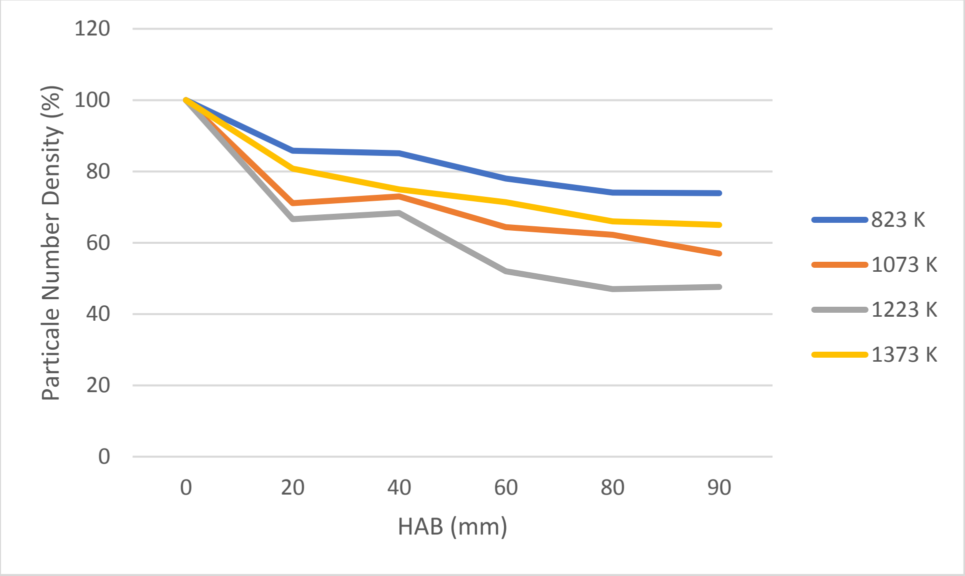

Figure 7.11 Effect of co-flow temperature on normalized particle number for HFO spray SMD of 50-µm (cases 1 to 4).

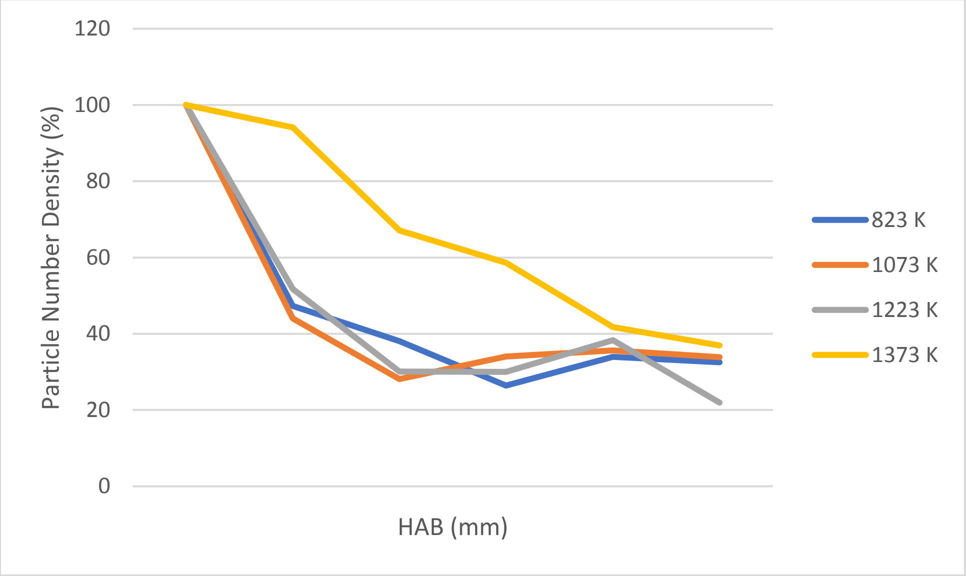

Figure 7.12 Effect of co-flow temperature on normalized particle number for HFO spray SMD of 32-µm (cases 5 to 8).

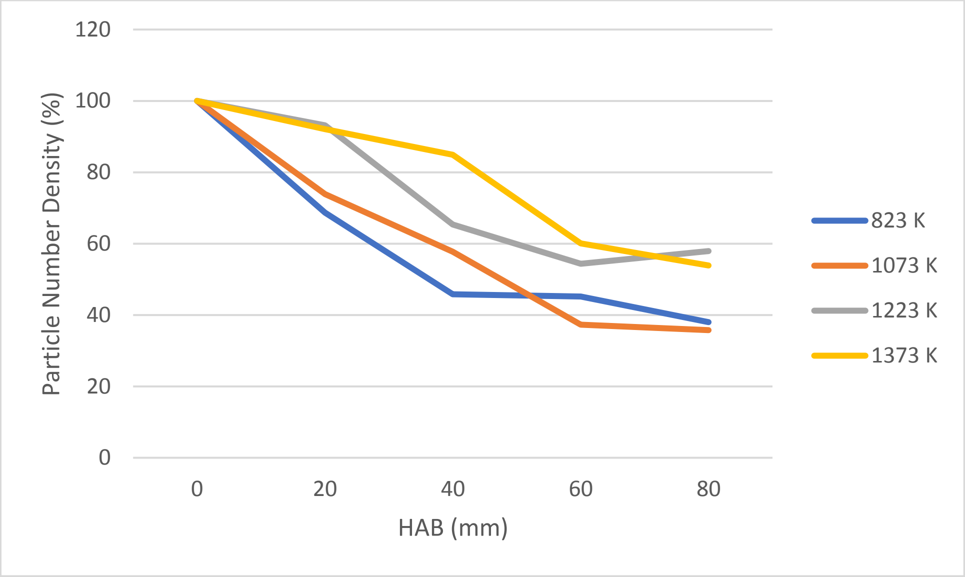

Figure 7.13 Effect of co-flow temperature on normalized particle number for HFO spray with SMD of 28-µm (cases 9 to 12).

Figure 7.12 and Figure 7.13 show a similar comparison for cases 5-8 corresponding to SMD of 32-µm and cases 9-12 with SMD of 28-µm respectively. For cases 5 to 8, with increase in co-flow temperature from 823 K to 1373 K, no pronounced effect on droplet combustion rate is observed. However, early droplet pyrolysis is observed at lower flame heights for 1373 K case (case 8). For the cases 9 to 12, similar trends of reduction in normalized particle number with increase in surrounding temperatures is observed till 1073 K and then increase as the co-flow temperature increases up to 1373 K. Thus, it is found that the temperature around 1223 K is optimal for cenosphere reduction.

Using the above-mentioned particle number statistics, a critical droplet diameter is estimated using the following procedure.

i. Estimate number of particles at height 20-mm and these particles are assumed to represent the total number of HFO droplets injected at any given time.
ii. Estimate number of particles at height 90-mm and these particles are assumed to be early stage cenospheres generated during combustion.
iii. The total number of droplets injected are estimated by summation over 300 images while a total number of cenospheres emitted are also estimated by summation over 300 images.
iv. The fraction of undergoing complete combustion is then estimated.
v. From the measured drop size distribution, a cumulative droplet PDF versus droplet size curve is determined. (Refer Figure 7.14)
vi. It is assumed that the droplets generating cenospheres belong to the larger size in the drop size distribution, while all smaller droplets undergo complete combustion

vii. Comparing the fraction of completely burnt droplets to the cumulative droplet PDF, a droplet diameter is estimated. This estimated droplet diameter corresponds to the largest size of a completely burnt droplet, i.e., the critical droplet diameter.

Figure 7.14 to Figure 7.17 show the PDF of droplet size and the estimated critical droplet diameters for cases 9 to 12, respectively. Thus, an average critical droplet diameter for the medium grade of HFO used in this study is found to be around 18-µm.

Thus, from the above-mentioned statistical investigation of cenosphere formation in HFO spray flames, the following conclusions can be derived,

- The critical droplet diameter for the medium grade of HFO used in the present study is in range of 16-µm to 22-µm.
- Below this critical diameter, droplet pyrolysis does not take place and droplet undergoes complete combustion.
- Higher co-flow temperatures typically greater than 1373 K promote droplet pyrolysis.
- A co-flow surrounding temperature in the range of 1073 K to 1223 K is found to be optimal for reduction in cenosphere formation.

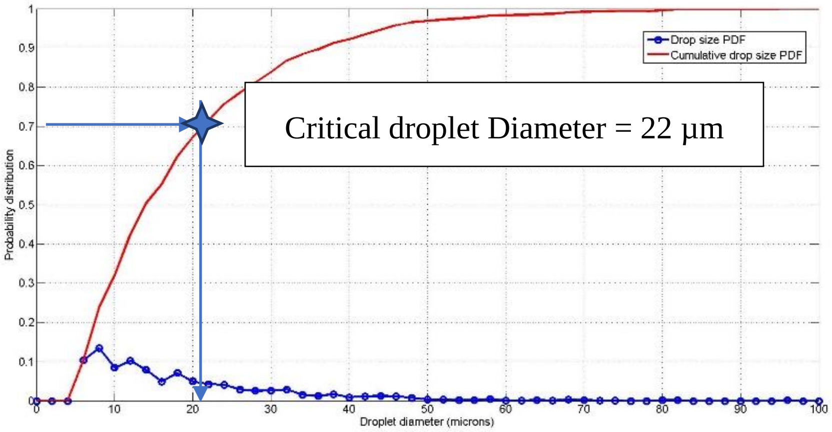

Figure 7.14 Cumulative drop size PDF and Critical droplet diameter for SMD of 28-µm and surrounding temperature of 823 K (case 9).

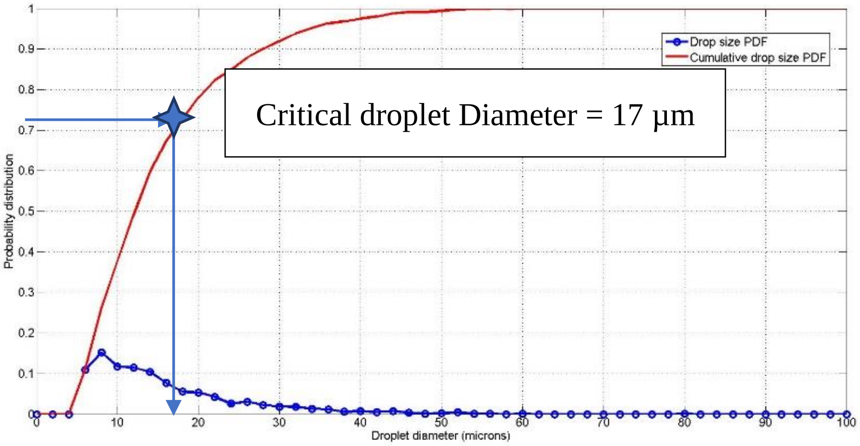

Figure 7.15 Cumulative drop size PDF and Critical droplet diameter for SMD of 28-µm and surrounding temperature of 1073 K (case 10).

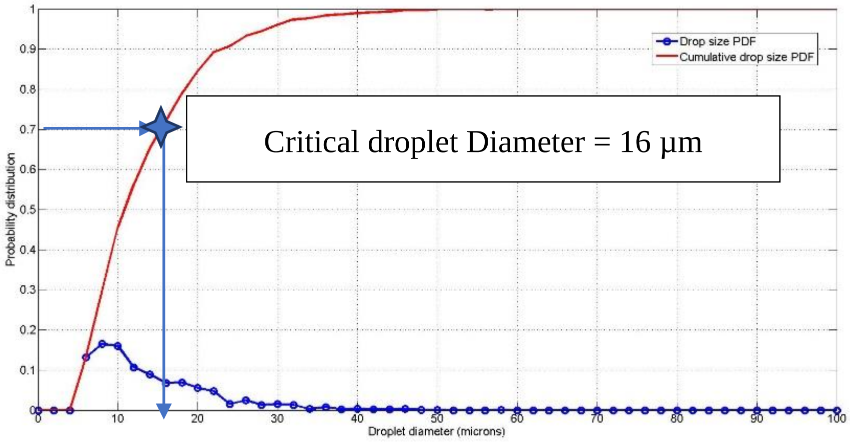

Critical droplet Diameter = 16 µm

Figure 7.16 Cumulative drop size PDF and Critical droplet diameter for SMD of 28-µm and surrounding temperature of 1223 K (case 11).

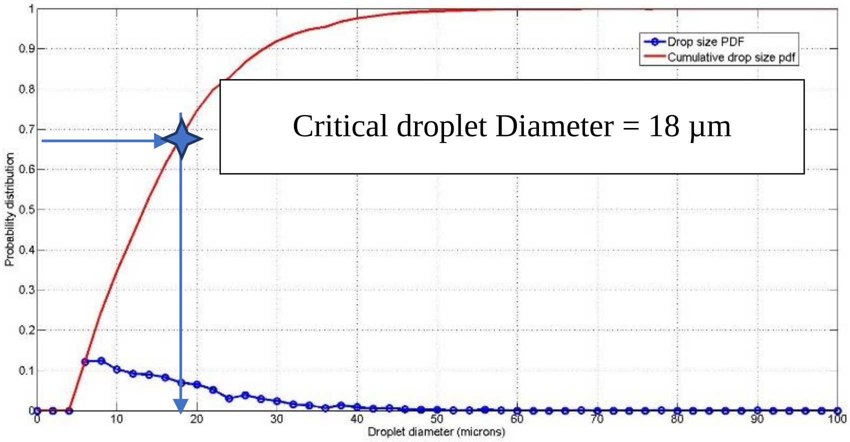

Critical droplet Diameter = 18 µm

Figure 7.17 Cumulative drop size PDF and Critical droplet diameter for SMD of 28-µm and surrounding temperature of 1373 K (case 12).

8 Conclusions

In the present study, an experimental investigation of HFO droplet combustion and the effect of HFO spray characteristics on carbon particulate emission in a spray combustion environment has been successfully carried out. A new research burner is designed to study fundamental combustion characteristics of HFO droplets in a controlled high-temperature environment (800 – 1300 K). The research burner is initially used to study droplet evaporation in convective spray environments for single component liquids (n-decane and n-dodecane) and a mathematical methodology is established to extract evaporation rate constant from spray droplet size distribution and droplet velocities. This methodology is further extended to estimate droplet evaporation rate constant for multi-component fuels such as Jet-A1. The research burner is then utilized to study HFO spray combustion and particulate formation. A novel Laser-induced fluorescence (LIF) based optical technique is developed to optically image HFO droplets in the high-temperature spray flame environment. Based on this data, the injection parameters are optimized to achieve spray characteristics with Sauter Mean Diameters (SMD) ranging from 24-µm to 53-µm. The soot measurements are carried out in the HFO spray flames using the Laser-induced incandescence (LII) technique to identify soot formation and oxidation zones. Soot is observed to be produced at lower flame heights and subsequently oxidized along the spray flame height. It is observed that a reduction in SMD from 53-µm to 24-µm leads to a 58% reduction in soot formation. To investigate the impact of the HFO spray characteristics and the co-flow temperature on droplet pyrolysis, the cenosphere sizes are measured using an aerodynamic particle sizer. With a change in SMD from 53-µm to 24-µm, a drastic reduction (~90%) in cenosphere emission density (particles/cm^3) is observed. It is also observed that higher temperatures in the range of 1073 K to 1223 K are favorable for cenosphere reduction. The morphological study of cenospheres indicates that these are nascent coke particles generated at the end of the droplet combustion phase. These results seem to contradict the generally accepted theory that ‘one droplet generates one cenosphere’. The data is further analyzed to establish the existence of a critical diameter of HFO, which undergoes complete combustion in the droplet combustion phase without generating a solid coke particle. In other words, if the HFO spray consists of droplets whose diameter is below this critical value, the particulate emissions can be drastically minimized. From the experimental data, the critical droplet diameter is found to be in the range of 18 µm to 23 µm for the medium grade of HFO used.

Thus, the current work adds the following new observations to the literature:

i. ‘One HFO droplet generate one cenosphere' theory is not valid for very small HFO droplets typically below 18-µm. It can be theorized that competition between evaporation, cracking mechanisms, and carbonization reduce the hydrocarbon chains available to form the solid coke nucleus.

ii. A critical droplet diameter exists for HFO fuels, below which HFO droplets undergo complete combustion without formation of coke particles. This critical droplet size range of 16-µm to 22-µm for the medium grade HFO used in the present study.

iii. The gas temperatures surrounding the HFO droplet need to be above 1073 K for oxidation of nascent soot as well as inhibition of cenosphere formation. This is specific to the grade of HFO used.

iv. The co-flow temperature range between 1073 K to 1223 K appears suitable for lower cenosphere production. The temperatures in excess of 1373 K promote droplet pyrolysis.

v. A novel optical diagnostic technique based on LIF is developed to measure fuel droplet size distribution in a combusting environment.

8.1 Scope for future work

1. Depending upon the grade of HFO, there exists a critical droplet diameter to achieve minimum particulate emissions. The critical droplet diameter for a medium grade of HFO is of the order of 18-µm. To achieve droplets in this size range at practical fuel flow rates is a challenge. Hence, as a next step, it is imperative to develop a suitable HFO atomizer which can achieve smaller droplets (~ 20 µm) at higher fuel flow rates.

2. Based on the present work, it is clear that maintaining the temperature in the range of 1000 K to 1200 K in the inner recirculation zone (IRZ) of a swirl burner is beneficial for HFO atomization and soot oxidation. Hence, there is a need to develop an HFO combustor which provides sufficiently higher temperatures in the vicinity of the fuel spray.

3. Another strategy to achieve higher temperatures in the IRZ region is to use a dual fuel strategy, i.e., use of natural gas and HFO together to increase the heating rate of droplets in the spray cone. This option also needs to be evaluated.

4. Finally, understanding and modeling of carbonization mechanisms and nuclei formation inside HFO droplets during combustion is required to be investigated. This aspect can help in assessing the critical droplet diameter of various grades of HFO used in burners.

9 Bibliography

[1] R. Kalpokaite-Dichkuvene and G. Stravinskas, “Behavior of a fuel oil droplet on a hot surface,” *J. Eng. Phys. Thermophys.*, vol. 79, no. 1, pp. 10–17, 2006.

[2] C. Allouis, F. Beretta, and A. D’Alessio, “Structure of inorganic and carbonaceous particles emitted from heavy oil combustion,” *Chemosphere*, vol. 51, no. 10, pp. 1091–1096, 2003.

[3] K. D. Bartle *et al.*, “The combustion of droplets of high-asphaltene heavy oils,” *Fuel*, vol. 103, pp. 835–842, 2013.

[4] A. Breña de la Rosa, A. Sobiesiak, and T. A. Brzustowski, “The influence of fuel properties on drop-size distribution and combustion in an oil spray,” *Symp. Combust.*, vol. 21, no. 1, pp. 557–566, 1988.

[5] R. Weber, “Scaling characteristics of aerodynamics, heat transfer, and pollutant emissions in industrial flames,” *Symp. Combust.*, vol. 26, no. 2, pp. 3343–3354, 1996.

[6] C. A. Miller, W. P. Linak, C. King, and J. O. L. Wendt, “Combustion Science and Technology Fine Particle Emissions from Heavy Fuel Oil Combustion in a Firetube Package Boiler Fine Particle Emissions from Heavy Fuel Oil Combustion in a Firetube Package Boiler,” *Combust. Sci. Technol.*, vol. 134, no. July 2012, pp. 477–502, 2010.

[7] H. Y. Park and Y. J. Kim, “Combustion characteristics of vacuum residue in a test furnace and its utilization for utility boiler,” *Korean J. Chem. Eng.*, vol. 24, no. 1, pp. 83–92,

2007.

[8] A. Chávez, M. Ramírez, E. Medina, R. Bolado, and J. Mora, “Advances in the generation of a new emulsified fuel,” *Heat Mass Transf. und Stoffuebertragung*, vol. 47, no. 8, pp. 1051–1063, 2011.

[9] Byrnes M A *et al.*, “Measurement and Predictions of Nitric Oxide and Particulates Emissions from Heavy Fuel Oil,” *Combust. Inst.*, vol. Twenty-Six, pp. 2241–2250, 1996.

[10] J. Yuan, V. Semião, and M. G. Carvalho, “Modelling and validation of the formation and oxidation of cenospheres in a confined spray flame,” *Int. J. Energy Res.*, vol. 21, no. 14, pp. 1331–1344, 1997.

[11] A. Barreiros, M. G. Carvalho, M. Costa, and F. C. Lockwood, “Prediction of the near burner region and measurements of NOxand particulate emissions in heavy fuel oil spray flames,” *Combust. Flame*, vol. 92, no. 3, pp. 231–240, 1993.

[12] R. Villasenor and R. Escalera, “A highly radiative combustion chamber for heavy fuel oil combustion,” *Int. J. Heat Mass Transf.*, vol. 41, no. 20, pp. 3087–3097, 1998.

[13] A. Rebola and M. Costa, “Simultaneous reduction of NOx and particulate emissionsfrom heavy fuel oil-fired furnaces,” *Proc. Combust. Inst.*, vol. 29, no. 2, pp. 2243–2250, 2002.

[14] A. L. Shihadeh *et al.*, “Low NOx Emissions from Aerodynamically Staged Oil-Air Turbulent Diffusion Flames,” *Chem. Phys. Process. Combust.*, 1994.

[15] C. Allouis, A. D’Alessio, C. Noviello, and F. Beretta, “Time resolved laser induced incandescence for soot and cenospheres measurements in oil flames,” *Combust. Sci. Technol.*, vol. 153, no. 1, pp. 51–63, 2000.

[16] W. P. Linak, C. A. Miller, and J. O. L. Wendt, “A Fine Particle Emissions from Residual

Fuel Oil Combustion : Characterization and Mechanisms of Formation," vol. 28, pp. 2651–2658, 2000.

[17] R. Weber and F. Breussin, "Scaling properties of swirling pulverized coal flames: From 180 kW to 50 MW thermal input," *Symp. Combust.*, vol. 27, no. 2, pp. 2957–2964, 1998.

[18] D. L. Urban *et. al.* "Twenty-Fourth Symposium (International) on Combustion/The Combustion Institute," pp. 1357–1364, 1992.

[19] D. L. Urban and F. L. Dryer, "Twenty-Third Symposium (International) on Combustion/The Combustion Institute, 1990/pp. 1437-1443," pp. 1437–1443, 1990.

[20] R. Villasenor and F. Garcia, "An experimental study of the effects of asphaltenes on heavy fuel oil droplet combustion," *Fuel*, vol. 78, no. 8, pp. 933–944, 1999.

[21] G. Xu, M. Ikegami, S. Honma, K. Ikeda, X. Mao, and H. Nagaishi, "Burning droplets of heavy oil residual blended with diesel light oil: Analysis of coke behaviors," *Energy and Fuels*, vol. 17, no. 3, pp. 779–790, 2003.

[22] G. Xu, M. Ikegami, and S. Honma, "Combustion Science and Technology Burning droplets of heavy oil residual blended with diesel light oil : Characterization of burning steps," *Sci. Technol.*, no. October 2011, pp. 115–145, 2010.

[23] M. Ikegami *et al.*, " Distinctive combustion stages of single heavy fuel oil droplet under Microgravity," *Fuel*, vol. 82, pp. 293–304, 2003.

[24] V. Garaniya, "Modelling of heavy fuel oil spray combustion using continuous thermodynamics," *Phd thesis, University of Tasmania*, 2009.

[25] L. Witzel, P. Moszkowicz, and G. Claus, "Mechanism of particulate reduction in heavy fuel oil combustion," *Fuel*, vol. 74, no. 12, pp. 1881–1886, 1995.

[26] P. Murugan, N. Mahinpey, and T. Mani, “Thermal cracking and combustion kinetics of asphaltenes derived from Fosterton oil,” *Fuel Process. Technol.*, vol. 90, no. 10, pp. 1286–1291, 2009.

[27] A. C. Eckbreth, “Effects of laser-modulated particulate incandescence on Raman scattering diagnostics,” *J. Appl. Phys.*, vol. 48, no. 11, pp. 4473–4479, 1977.

[28] L. A. Melton, “Soot diagnostics based on laser heating,” *Appl. Opt.*, vol. 23, no. 13, p. 2201, 1984.

[29] H. Bladh, J. Johnsson, and P. E. Bengtsson, “On the dependence of the laser-induced incandescence (LII) signal on soot volume fraction for variations in particle size,” *Appl. Phys. B Lasers Opt.*, vol. 90, no. 1, pp. 109–125, 2008.

[30] W. Ketren, P. Vallikul, a Garo, and G. Grehan, “Numerical Simulation on Effects of Laser Fluence on Temporal and Time Integrated LII-Process of Soot Particle,” *Environment*, vol. 1, pp. 173–179, 2010.

[31] S. Will, S. Schraml, K. Bader, and A. Leipertz, “Performance characteristics of soot primary particle size measurements by time-resolved laser-induced incandescence,” *Appl. Opt.*, vol. 37, no. 24, p. 5647, 1998.

[32] “Laser Incuced Incandescence - LaVision manual.”

[33] T. Ni, J. A. Pinson, S. Gupta, and R. J. Santoro, “Two-dimensional imaging of soot volume fraction by the use of laser-induced incandescence,” *Appl. Opt.*, vol. 34, no. 30, p. 7083, 1995.

[34] N. H. Qamar, Z. T. Alwahabi, Q. N. Chan, G. J. Nathan, D. Roekaerts, and K. D. King, “Soot volume fraction in a piloted turbulent jet non-premixed flame of natural gas,”

Combust. Flame, vol. 156, no. 7, pp. 1339–1347, 2009.

[35] G. Smallwood and K. P. Geigle, "LII Workshop Session: Experimental Issues and Experiments performed," 2nd International discussion meeting and workshop on 'Laser Induced Incandescence: Quantative interpretation, modeling, application, 2006.

[36] M Kohler *et.al.* , "Sooting turbulent jet flame : characterization and quantitative soot measurements," Applied Physics:B Lasers and Optics, p. 409-425 2011.

[37] S. De Iuliis, F. Cignoli, and G. Zizak, "Peak soot temperature in laser-induced incandescence measurements," *CEUR Workshop Proc.*, vol. 195, p. 31, 2005.

[38] R. Wainner and J. Seitzman, "Soot diagnostics using laser-induced incandescence in flames and exhaust flows," *37th Aerosp. Sci. Meet. Exhib.*, 1999.

[39] H. A. Michelsen, "Understanding and predicting the temporal response of laser-induced incandescence from carbonaceous particles," *J. Chem. Phys.*, vol. 118, no. 15, pp. 7012–7045, 2003.

[40] F. Goulay, P. E. Schrader, L. Nemes, M. A. Dansson, and H. A. Michelsen, "Photochemical interferences for laser-induced incandescence of flame-generated soot," *Proc. Combust. Inst.*, vol. 32 I, pp. 963–970, 2009.

[41] R. L. Vander Wal, "Laser-induced incandescence: detection issues," *Appl. Opt.*, vol. 35, no. 33, pp. 6548–6559, 1996.

[42] R. L. Vander Wal and K. J. Weiland, "Laser-induced incandescence: Development and characterization towards a measurement of soot-volume fraction," *Appl. Phys. B Laser Opt.*, vol. 59, no. 4, pp. 445–452, 1994.

[43] C. R. Nelson *et al.*, "Soot diagnostics using laser-induced incandescence in flames and

exhaust flows," *Appl. Phys. B Lasers Opt.*, vol. 23, no. 3, pp. 1457–1467, 2010.

[44] F. Cignoli, S. De Iuliis, V. Manta, and G. Zizak, "Two-dimensional two-wavelength emission technique for soot diagnostics," *Appl. Opt.*, vol. 40, no. 30, p. 5370, 2001.

[45] J. Zerbs *et al.*, "The influence of wavelength in extinction measurements and beam steering in laser-induced incandescence measurements in sooting flames," *Appl. Phys. B Lasers Opt.*, vol. 96, no. 4, pp. 683–694, 2009.

[46] Snelling *et.al.* , "Soot volume fraction measurements by two-dimensional imaging of laminar diffusion flames," NRC Publications Archive Archives des publications du CNRC

[47] A. M. Mohan, T. N. C. Anand, and R. V Ravikrishna, "Experimental spray characterisation of air-assisted impinging jets Dept . of Mechanical Engineering , Indian Institute of Science , India Dept . of Mechanical Engineering , Indian Institute of Technology Madras , India," pp. 1–8, 2012.

[48] R. Lemaire, M. Maugendre, T. Schuller, E. Therssen, and J. Yon, "Original use of a direct injection high efficiency nebulizer for the standardization of liquid fuels spray flames," *Rev. Sci. Instrum.*, vol. 80, no. 10, 2009.

[49] R. Lemaire, A. Faccinetto, E. Therssen, M. Ziskind, C. Focsa, and P. Desgroux, "Experimental comparison of soot formation in turbulent flames of Diesel and surrogate Diesel fuels," *Proc. Combust. Inst.*, vol. 32 I, no. 1, pp. 737–744, 2009.

[50] R. Lemaire, E. Therssen, and P. Desgroux, "Effect of ethanol addition in gasoline and gasoline-surrogate on soot formation in turbulent spray flames," *Fuel*, vol. 89, no. 12, pp. 3952–3959, 2010.

[51] B. Cushman-roisin and J. Wiley, "ENVIRONMENTAL FLUID MECHANICS" Book

published on March, 2014.

[52] S. S. Sazhin *et al.*, “A simplified model for bi-component droplet heating and evaporation,” *Int. J. Heat Mass Transf.*, vol. 53, no. 21–22, pp. 4495–4505, 2010.